Princeton University

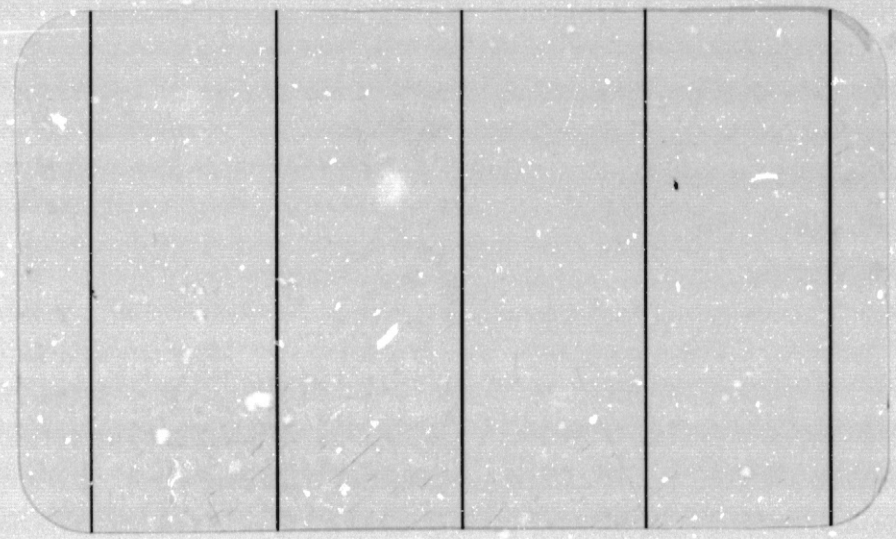

Department of Aerospace and Mechanical Sciences

NASA CR-134 999

IMPACT OF COMPOSITE PLATES: ANALYSIS OF STRESSES AND FORCES

F.C. Moon
B.S. Kim
S.R. Fang-Landau
January 1976

1. Report No.	2. Government Accession No.	3. Recipient's Catalog No.
NASA CR 134999		

4. Title and Subtitle	5. Report Date
Impact of Composite Plates: Analysis of Stresses and Forces	January 1976
	6. Performing Organization Code

7. Author(s)	8. Performing Organization Report No.
F. C. Moon B. S. Kim S. R. Fang-Landau	AMS Report No. 1298
	10. Work Unit No.

9. Performing Organization Name and Address	11. Contract or Grant No.
Department of Aerospace and Mechanical Sciences Princeton University Princeton, NJ 08540	NGR-31-001-267
	13. Type of Report and Period Covered
12. Sponsoring Agency Name and Address	Final Report 5/74-8/75
National Aeronautics and Space Administration Washington, DC 20546	14. Sponsoring Agency Code

15. Supplementary Notes

Project Manager: C. C. Chamis
Materials & Structures Division
NASA Lewis Research Center
Cleveland, OH 44135

16. Abstract

This final report presents the results of analyses dealing with three problems related to the foreign object damage resistance of composite fan blades. In the first part, edge impact stresses in an anisotropic plate are calculated incorporating a constrained layer damping model. This protection scheme would use a high damping elastomer layer between an elastic impact protection strip and the edge of the anisotropic plate. It is shown that a very thin damping layer can dramatically decrease the maximum normal impact stresses. In part II a multilayer model of a composite plate is presented which allows computation of the interlaminar normal and shear stresses. Results are presented for the stresses due to a line impact load normal to the plane of a composite plate. It is shown that significant interlaminar tensile stresses can develop during impact. A computer code has been developed for this problem using the fast Fourier transform. In part III a marker and cell computer code has been used to investigate the hydrodynamic impact of a fluid slug against a wall or turbine blade. Application of fluid modeling of bird impact is reviewed. Velocity and pressure fields as well as force histories are presented for normal and oblique impact of incompressible fluid spheres and cylinders for various viscosities and boundary conditions.

17. Key Words (Suggested by Author(s))	18. Distribution Statement
Fiber Composites, Impact Stresses, Impact Forces, Stress Waves, Constrained Layer Stresses, Interlaminar Stresses, Hydrodynamic Impact Model, Bird Impact, Composite Blades	Unclassified, Unlimited

19. Security Classif. (of this report)	20. Security Classif. (of this page)	21. No. of Pages	22. Price*
Unclassified	Unclassified	110	$5.25

* For sale by the National Technical Information Service, Springfield, Virginia 22151

Table of Contents

Summary

This is the final report on the theoretical studies of impact of composite plates completed by the principal investigator at Princeton University. Previous reports under this grant have presented analyses and computer codes for the calculation of stresses in composite plates due to central and edge impact of hard objects. These studies were directed toward the problem of foreign object damage in jet engine fan blades. The present report is directed toward three separate problems related to foreign object damage in composite plate like structures. These are; the effectiveness of constrained layer damping for leading edge impact protection; the development of multilayer mathematical models to calculate interlaminar stresses due to impact of composite plates; and a review of fluid modelling techniques for predicting impact stresses and forces due to bird impact.

Part I - Constrained Layer Damping of Impact Stresses.

In a previous report an analytical-computational code was developed to predict the stresses due to the in plane edge impact of an anisotropic plate. This code included provision for an elastic protection strip to be placed between the impact force and the half plane of the plate. In the present report this code is modified to include a viscoelastic layer between the elastic protection strip and the composite plate. Similar techniques for damping plate vibrations have proved very successful. Numerical results show that a very thin elastomer damping layer may significantly reduce the normal impact stresses in the plate. The results are based on a modification of the plate-protection strip boundary condition. Since the code uses the fast Fourier transform, experimentally determined,

frequency dependant material constants for the elastomer can be included.

Part II - Multilayer Model for Impact of Composite Plates.

In earlier studies by the principal investigator, the central impact of composite plate was modelled using a plate theory that included linear bending and shear displacements and a single transverse displacement variable which effectively neglected wave propagation through the thickness of the plate. In the present report higher order inertia variables are included. In addition the plate is broken down into a set of identical orthotropic layers. Each layer may represent many plys or in specialized cases a single ply of the composite plate. Incorporation of these two features results in a model that can predict interlaminar shear and normal stresses as well as wave propagation through the thickness direction. Results for the line impact of a two layer plate show an interlaminar tension developing under the load after impact. The computer code which solves finite difference equations for a periodic set of oscillators can handle any number of layers.

Part III - Dynamics of Bird Impact.

Prediction of impact stresses in composite fan blades not only depends on the structural modelling but on an accurate knowledge of the force between the foreign object and the structure. In the final section of this report methods for predicting the forces generated during a bird impact with a solid wall are investigated. The physical properties of birds as related to impact are reviewed. Simple Hertz impact calculations for bone and composite materials show that the skeletal bones of birds will disintegrate under impact suggesting that a fluid model for impact might be useful for high speed impact greater than 50 m/s. A brief survey of the literature of rain drop impact and computational fluid mechanics is

presented. A marker and cell hydrodynamic code is used to calculate pressurec and force history between a flat plate and viscous incompressible fluid of cylindrical and spherical shape. Both normal and oblique impact are studied. The pressure and force histories show a fluctuation behavior suggesting either real or computational instabilities in the code. Velocity distributions show the development of an eddy effect near the wall and a subsequent stationary zone of liquid near the plate. This leads to a fairly uniform pressure distribution across the contact area between the fluid and the wall.

PART I

Edge Impact of a Plate With Constrained Layer Damping

by

F.C. Moon

Part I - Edge Impact of a Plate With Constrained Layer Damping.

To prevent failure of composite fan blades under impact forces, leading edge protection strips have been employed. In practice strips of stainless steel are wrapped around the leading edge of the blade. The effect of the strip is to thwart the force of impact, thereby spreading the normal impact stresses over a large area of the composite material underneath the strip.

In a previous report we developed an analytical model for edge impact of a composite plate with edge protection [3]. In this model the composite plate was treated as a homogeneous anisotropic elastic material and the edge protection modelled as a beam which is connected to the edge. The results of that study showed that the edge strip could decrease both the normal and edge wise impact stresses at the surface but that significant shear stress could develop at the bond between the edge strip and the plate. The calculations were carried out for in-plane impact loads.

The edge protection strip is only effective to the extent that it spreads the transient impact loading over a surface along the plate edge larger than the impact contact area. Also it disperses the pulse so that the impact energy to the plate is spread out in time, hence decreasing the peak stresses.

In contrast to the energy dispersion method of decreasing impact stresses the dissipation method uses damping material to convert the impact energy into heat instead of into kinetic and stored elastic energy in the plate. There are two approaches to the absorbtion of structural vibration in beams and plates. In one method a highly viscoelastic material

is simply connected to one face of the beam or plate. Energy is converted to heat in the viscoelastic layer through normal stresses. This method has been used to quiet the vibration of submarines. This method contrasts with the constrained layer method in which the energy is dissipated through shear stresses. This is accomplished by cementing a soft viscoelastic material to the plate and covering the damping layer with a stiff elastic material (see Figure 1). Thus the viscous layer is constrained between two elastic plates, hence the name. In practice the viscoelastic sublayer is a thin high damping elastomer while the constraining plate can be a thin plate of aluminum or steel. This method has been studied both experimentally and analytically for vibratory motion by Yan [4] and Yan and Dowell [5].

It is proposed to use such a method for the absorbtion of transient impact vibrations of composite fan blades by placing a thin elastomer material between the leading edge protection strip and the composite blade material

In this section a model is proposed to examine the energy absorbing potential of such a concept for the edge impact of an anisotropic half space. The model is shown in Figure 2 . Between the anisotropic half space and the edge protection strip we assume a thin layer of viscoelastic material which has a uniform normal strain in the x_3 direction ϵ_{33} and an average shearing strain γ_{13}. The inertia of the layer is neglected as well as bending moments. Thus the stresses t_{33}, and t_{13} are transmitted from the beam to the half space unperturbed. However the compalibility conditions between the beam displacements U, W and the plate edge displacements u_1, u_3 are changed.

If ϵ_{33} is the uniform strain in the sublayer at position x_1 and d

the thickness of this layer, then the relation between u_3 and W is given by

$$u_3 - W = \epsilon_{33} d \tag{I-1}$$

Further if α is the change in angle of a line element normal to the damping layer (see Figure 2), then the relation between u_1 and U is given by

$$U - u_1 = \frac{b}{2} \frac{\partial W}{\partial x_1} - \alpha d \tag{I-2}$$

However, the angle α is not the total shearing strain. At the center of the damping layer we take the average shearing strain to be

$$\gamma_{13} = + \alpha + \frac{\partial}{\partial x_1}(u_3 - \epsilon_{33} d/2) \tag{I-3}$$

Finally to find ϵ_{33}, γ_{13} we use the viscoelastic constitutive relations between the strains and t_{33}, t_{13} for the sublayer. We also neglect the strain ϵ_{11} in the sublayer. Thus for the Laplace transformed variables where $s = i\omega$ we have

$$\epsilon_{33} = t_{33}/Y(\omega) \quad , \quad \gamma_{13} = t_{13}/G(\omega) \tag{I-4}$$

where $Y(\omega)$, $G(\omega)$ are complex functions of the frequency ω, and t_{11} and t_{22} are neglected in (I-4).

The stresses t_{33} and t_{13} are related to the surface displacements of the half space u_1, u_3 through constitutive equations for the plate and the displacements must satisfy the wave equations in the plate. To find the displacements and stresses in the composite plate, we follow the same procedure as the no-strip case except for the boundary conditions on the edge. In place of the zero stress conditions on the edge we

relate the edge stresses t_{33}, t_{13} to the motion of the beam strip. If one considers a small element of the beam-strip along the x_1 direction, the momentum balance equations in the x_1, x_3 directions become, (for a plate of unit thickness)

$$\rho b \frac{\partial^2 U}{\partial t^2} = Eb \frac{\partial^2 U}{\partial x_1^2} + t_{13} \tag{I-5}$$

$$\rho b \frac{\partial^2 W}{\partial t^2} = - EI \frac{\partial^4 W}{\partial x_1^4} + I_\rho b \frac{\partial^4 W}{\partial x_1^2 \partial t^2} + \frac{b}{2} \frac{\partial t_{13}}{\partial x_1} + t_{33} + p_o f g$$

In these equations U, W are the x_1, x_3 displacements of the beam element at the half thickness, and t_{33}, t_{13} are the interface stresses.

The compatibility condition between the beam and plate displacements W and u_3 are given by (I-1) and the condition between U, and u_1 is given by (I-2).

In the above equations b is the depth of the strip, E, I, I_ρ are respectively the Young's modulus, moment of inertia and rotary inertia. Also $p_o f(t) g(x_1)$ is the edge loading applied to the outer protective strip surface.

The equations for the plate remain as in the free edge case [3] and a solution is obtained by taking a Laplace transform on time and a Fourier transform on the space variable x_1. With nondimensionalization the solution in the plate has the form

$$\begin{bmatrix} \bar{u}_1 \\ \bar{u}_3 \end{bmatrix} = C_1 \begin{bmatrix} 1 \\ \psi_{31} \end{bmatrix} e^{-p_1 x_3} + C_2 \begin{bmatrix} 1 \\ \psi_{32} \end{bmatrix} e^{-p_2 x_3} \tag{I-6}$$

where p_1, p_2 and Ψ_{31}, Ψ_{32} are given by the following equations ($\bar{u}$ indicates a Fourier and Laplace transformed variable).

$$\det = C_{33}C_{55}p^4 + [C_{33}(-s^2-C_{11}k_1^2)+C_{55}(-s^2-C_{55}k_1^2)+k_1^2(C_{13}+C_{55})^2]p^2 + (s^2+C_{11}k_1^2)(s^2+C_{55}k_1^2) = 0 \tag{I-7}$$

where the C_{ij} are the equivalent elastic constants for the anisotropic plate. We will choose the p's with positive real parts to insure the decay in x_3 direction of the surface wave. Let the solutions be $p = p_1, p_2$, therefore, we have

$$p = p_1 : \phi_1^{(1)} \equiv C_1(k_1,s) \quad , \quad \phi_2^{(1)} = -\frac{i[-s^2-C_{11}k_1^2+C_{55}p_1^2]}{k_1 p_1 (C_{13}+C_{55})}\phi_1^{(1)} \equiv \Psi_{31}C_1 \tag{I-8}$$

$$p = p_2 : \phi_1^{(2)} \equiv C_2(k_1,s) \quad , \quad \phi_2^{(2)} = \Psi_{32}C_2 \equiv -\frac{i[-s^2-C_{11}k_1^2+C_{55}p_2^2]}{k_1 p_2 (C_{13}+C_{55})}\phi_1^{(2)}$$

The equations of motion for the beam (I-5a,b), are next transformed using a Laplace transform on time and a Fourier Transform on the space variable x_1. When the solutions for $\bar{u}_1$, $\bar{u}_3$, along with the constraint conditions for $\bar{W}$, $\bar{U}$ are substituted into the bending and extensional equations of motion for the beam, and the constitutive equations (I-4), used to eleminate the stresses t_{33}, t_{13} we obtain two equations for the unknown constants C_1, C_2 in (I-6). These equations can be put into the form.

$$\begin{bmatrix} \gamma_1 & H_1 \\ G_2 & H_2 \end{bmatrix}\begin{bmatrix} C_1 \\ C_2 \end{bmatrix} = p_o\overline{fg}\begin{bmatrix} 1 \\ 0 \end{bmatrix} \tag{I-9}$$

To define the terms G_1, G_2, H_1, H_2 we use the symbol s for the Laplace transform variable and k for the Fourier transform variable where

$$\bar{F}(k,s) = \int_{-\infty}^{\infty}\int_{o}^{\infty} F(x,t)e^{-st}dt\ e^{-ikx}dx$$

Then using the following symbols

$$b\Delta_1 = \{EIk^4+I_\rho bk^2s^2+\rho bs^2\}$$

$$b\Delta_2 = \{Ebk^2+\rho bs^2\} \ ,$$

the matrix elements in (I-9) are given by

$$G_1(p_1,\psi_{31}) = b\Delta_1\psi_{31} - \frac{ikb}{2}C_{55}(ik\psi_{31}-p_1) - (ikC_{13}-C_{33}p_1\psi_{31})(1+\frac{bd\Delta_1}{Y(s)})$$

$$G_2(p_1,\psi_{31}) = b\Delta_2(1+\frac{ikb}{2}\psi_{31}) - C_{55}(ik\psi_{31}-p_1) \qquad \text{(I-10)}$$

$$+ b\Delta_2 d\left[\frac{ikb}{2Y(s)}(C_{33}p_1\psi_{31}-ikC_{13})+ik(\psi_{31}-\frac{d}{2Y(s)}[C_{13}ik-C_{33}p_1\psi_1])\right.$$

$$\left. - \frac{d}{G(s)}C_{55}(ik\psi_{31}-p_1)\right]$$

and where

$$H_1 = G_1(p_2, \psi_{32})$$

$$H_2 = G_2(p_2, \psi_{32})$$

When the thickness of the viscous layer is set equal to zero, i.e. $d = 0$, then one obtains the solution for an anisotropic plate with

with a beam glued to the edge. When the beam thickness is set to zero, i.e. b = 0, then the free edge plate is obtained. These two cases were studied in Reference [3].

To obtain solutions in the time domain for a pulsed imput fg the expressions for $\bar{u}_1$, $\bar{u}_3$ must be inverted. This was accomplished using a double fast Fourier transform as described in a previous report [2]. In the example choosen a specific elastomer was chosen whose viscoelastic properties were known. The material choosen was an elastomer made by the Dupont Corp., LR3-604. This material was used by Yan in his dissertation [4] and the numerical values of $Y(s)$ and $G(s)$ were obtained from data in Yan's thesis. This data is shown in Figures 3,4. The shear modulus can be represented in the form

$$G(s) = G(i\omega) = G'(\omega) + i\, G''(\omega)$$

$$= G'(1+i\, G''/G') \quad .$$

The expression for $G'(\omega)$ can be represented by a cubic function of $\log(\omega/2\pi)$. The ratio G''/G' is known as the loss tangent and for the particular temperature chosen can be approximated as a bilinear function of $\log(\omega/2\pi)$. Thus for each frequency component in the Fourier inversion of the solution the corresponding value of $G(s)$ was used.

Results of calculations for a specific case are shown in Figures 5,6 The plate material is a $\pm$ 15 degree layup angle graphite/epoxy composite. The parabolic loading length is a = 2 cm and the steel beam strip thickness is b = 0.5 cm. The contact time in this example is 35 μsec. Plotted in Figure 5 is the maximum normal stress at the plate interface t_{33}/p versus the normalized thickness of the shear sublayer d/a. One can see

that while the stress rises for very small values of d/a, the normal impact stress decreased dramatically for elastomer thicknesses less then 20% of the impact half length.

Figure 6 shows results for the edgewise stress t_{11}. The maximum edgewise stress without the beam is about $4.8\ p_o$ from the study of Ref. 3 and with the beam glued to the edge is $1.1\ p_o$. Adding a damping sublayer appears to increase the stress for $d/a < 0.15$ and the limit as $d/a \to 0$ does not appear to result in the zero sublayer case. This is believed due to the fact that the shear modulus for the sublayer is many orders of magnitude below that of the composite or the beam. Thus the sublayer acts as a zero shear stress boundary condition. To check this we ran a case for $d/a = 0$ but the shear condition for the beam set to $t_{13} = 0$ while maintaining continuity of normal stress and displacement. This can be accomplished in the computer model by setting $\Delta_2 = 0$ in equation (I-10). The result of this calculation leads to a maximum $t_{11} = 3.73\ p_o$ for the same loading conditions and plate material as the cases above. This value appears to be the limiting value for $d/a \to 0$ and explains the apparent paradox.

Page intentionally left blank

PART II

Multi-Layer Model For Wave Propagation in Composite Plates Due to Impact

by

F.C. Moon and B.S. Kim

Part II - Multi-Layer Model For Wave Propagation in Composite Plates

Section 1. Introduction

In our previous reports on wave propagation in composite plates [1], [2] the multiply plate was modeled by inclusion of linear bending and shear displacement across the thickness and a single transverse displacement variable for the midplane. This model is a modified Timoshenko plate using a procedure for obtaining approximate plate theories from the equations of elasticity developed by Mindlin [6]. This simplified model assumes that the wavelengths of the impact forcing function are equal to or greater than the thickness of the plate. It is further limited in that it cannot treat wave propagation through the thickness of the plate and predict damage phenomena such as spalling.

A number of researchers have presented models for a multi-layer composite plate. Many, however, have stopped short of the transient impact problem and have examined only the frequency-wavelength dispersion relation for wave propagation in the plate [7]-[12]. In this report we present another attempt to mathematically model the multilayer plate but will develop a method wherein propagation through the plate thickness can be handled and transient impact stresses can be calculated using an inexpensive fast Fourier algorithm on the digital computer.

The composite plate is represented by N layers; each layer may contain a number of plys (Fig.7). Each layer is treated as orthotropic with the symmetry axes of all the layers alligned. For alternating ply composites each layer should bontain two or more plys. The model can be extended to include the case of the layer symmetry axes at angles to each other but will not be reported here. A key assumption is that all the layers are identical. While restricting the application, this assumption allows us to formulate the problem

using difference-differential equations. The technique of periodic structures has been used in the study of electrical transmission lines [13] and in the vibration of multistory buildings [14]. A set of equations of motion is developed for a typical layer. The relative motion of one layer to another is related by a phase shift. In this way the number of layers can be increased without increasing the size of the matrices to be inverted to satisfy the boundary conditions.

The model incorporates the interlayer stresses as explicit variables. Through these stresses we hope to extend the analysis to the study of impact of composite plates with viscoelastic damping layers and with cracks. Such studies are now underway. In the results presented in this report only the line impact has been treated. This has simplified the calculations and saved computer time in testing out the model. The technique however can be extended to the two dimensional or central impact problem. The next sections will describe the model in detail and discuss the numerical results.

Section 2. Formulation

Basic Theory of Linear Anisotropic Elasticity. Cauchy's equations of motion in cartesian tensor form are

$$t_{ij,i} = \rho \ddot{u}_j$$

$$t_{ij} = t_{ji} \qquad \text{(II-1)}$$

where body forces are neglected and the stress tensor is related to the infinitesimal strain tensor ϵ_{ij} by

$$t_{ij} = C_{ijk\ell}\epsilon_{k\ell} \ , \qquad \text{(II-2)}$$

or in a condensed form this is often written as

$$t_i = C_{ij} e_j \tag{II-3}$$

The elastic moduli C_{ijkl} or C_{ij} has the following form for orthotropic materials

$$C_{ij} = \begin{bmatrix} C_{11} & C_{12} & C_{13} & 0 & 0 & 0 \\ C_{12} & C_{22} & C_{23} & 0 & 0 & 0 \\ C_{13} & C_{23} & C_{33} & 0 & 0 & 0 \\ 0 & 0 & 0 & C_{44} & 0 & 0 \\ 0 & 0 & 0 & 0 & C_{55} & 0 \\ 0 & 0 & 0 & 0 & 0 & C_{66} \end{bmatrix} \tag{II-4}$$

Analysis of a Layer. For a layer shown in Fig. 7 we employ the approximate plate theory of Mindlin [6] and the displacement field $\underset{\sim}{u}$ is expanded in terms of the Legendre polynomials as

$$\underset{\sim}{u}(x_1, x_2, x_3, t) = \sum_{n=0}^{\infty} \underset{\sim}{u}^{(n)}(x_1, x_3, t) P_n(\eta) \tag{II-5}$$

where η is the local coordinate along thickness and normalized by b (b; a half of layer thickness).

Instead of solving Eq.II-1 directly we obtain new approximate equations of motion by a variational process and integration over the thickness η. The result is

$$b t^{(n)}_{\alpha j, \alpha} + [P_n(\eta) t_{2j}]^1_{-1} - t^{(n)}_{2j} = \rho b \frac{2}{2n+1} u^{(n)}_j \quad (\alpha = 1, 3) \tag{II-6}$$

where

$$t_{\alpha j}^{(n)} = \int_{-1}^{1} P_n(\eta) t_{\alpha j} d\eta$$

$$t_{2j}^{(n)} = \int_{-1}^{1} \frac{dP_n(\eta)}{d\eta} t_{2j} d\eta$$

By substituting the constitutive relation (II-2) with the displacement expansion (II-5) into the above approximate equations of motion, we can find governing equations of motion in terms of $u_1^{(0)}$, $u_2^{(0)}$, $u_3^{(0)}$, $u_1^{(1)}$... . The accuracy of the theory depends on how many terms of the displacement field we retain. Since the complexity in formulation increases rapidly with the number of terms included we keep terms only up to second order. Furthermore we will only examine harmonic waves propagating along the x_1 direction so that we can drop $u_3^{(n)}$ terms and have $\frac{\partial}{\partial x_3}\{\ \} = 0$. Next to get rid of the undesired coupling with higher modes we set $u_1^{(2)} = u_2^{(2)} = 0$. Then the resulting equations are

$$2b(C_{11}u_{1,11}^{(0)} + \frac{1}{b}C_{12}u_{2,1}^{(1)}) + (t_{21}^{+} - t_{21}^{-}) = 2b\rho\ddot{u}_1^{(0)}$$

$$2b\ C_{66}(\frac{1}{b}u_{1,1}^{(1)} + u_{2,11}^{(0)}) + (t_{22}^{+} - t_{22}^{-}) = 2b\rho\ddot{u}_2^{(0)}$$

$$\frac{2b}{3}(C_{11}u_{1,11}^{(1)} + \frac{3}{b}C_{12}u_{2,1}^{(2)}) - 2C_{66}(\frac{u_1^{(1)}}{b} + u_{2,1}^{(0)}) + (t_{21}^{+} + t_{21}^{-}) = \frac{2}{3}b\rho\ddot{u}_1^{(1)} \qquad \text{(II-8)}$$

$$\frac{2b}{3}(C_{66}u_{2,11}^{(1)} + \frac{3}{b}C_{66}u_{1,1}^{(2)}) - 2(C_{12}u_{1,1}^{(0)} + \frac{1}{b}C_{22}u_2^{(1)}) + (t_{22}^{+} + t_{22}^{-}) = \frac{2}{3}b\rho\ddot{u}_2^{(1)}$$

$$(t_{22}^{+} - t_{22}^{-}) - 2(C_{12}u_{1,1}^{(1)} + \frac{3}{b}C_{22}u_2^{(2)}) = 0$$

$$(t_{21}^{+} - t_{21}^{-}) - 2(C_{66}u_{2,1}^{(1)} + \frac{3}{b}C_{66}u_1^{(2)}) = 0$$

Here we notice that the first, fourth and last equations are written in terms of $u^{(n)}_i$ where $(n+i)$ is an odd integer and represent the thickness stretching motion (or symmetric motion). In the rest of the equations in which $(n+i)$ is an even integer, the u's represent flexual motion (or antisymmetric motion). Hence this process has decoupled the stretching motion from bending motion.

To get rid of the 2nd order modes from Eq. (II-8) we solve the last two equations for $u_2^{(2)}$ and $u_1^{(2)}$, and insert them into the remaining four equations and drop the propagation of $u_2^{(1)}$ along x_1 direction which is equivalent to dropping $\frac{\partial}{\partial x_1}(t_{21}^+ - t_{21}^-)$ in the last equation. Then eq. (II-8) can be reduced as follows:

$$2b(C_{11}u^{(0)}_{1,11} + \frac{1}{b}C_{12}u^{(1)}_{2,1}) + (t_{21}^+ - t_{21}^-) = 2b\rho\ddot{u}_1^{(0)}$$

$$2b\, C_{66}(\frac{1}{b}u^{(1)}_{1,1} + u^{(0)}_{2,11}) + (t_{22}^+ - t_{22}^-) = 2b\rho\ddot{u}_2^{(0)}$$

$$\frac{2b}{3}\hat{C}_{11}u^{(1)}_{1,1} - 2C_{66}(\frac{u_1^{(1)}}{b} + u^{(0)}_{2,1}) + \frac{C_{12}b}{3C_{22}}(t_{22}^+ - t_{22}^-)_{,1} + (t_{21}^+ + t_{21}^-) = \frac{2}{3}b\rho\ddot{u}_1^{(1)} \qquad \text{(II-9)}$$

$$-2(C_{12}u^{(0)}_{1,1} + \frac{1}{b}C_{22}u_2^{(1)}) + (t_{22}^+ + t_{22}^-) = \frac{2}{3}\rho b\ddot{u}_2^{(1)}$$

where

$$\hat{C}_{11} = C_{11} - \frac{C_{12}^2}{C_{22}}$$

Section 3. Wave Propagation

Harmonic Waves. Let's consider now a harmonic wave propagating in the x_1 direction. Namely the solutions for $\underset{\sim}{u}$ and $\underset{\sim}{t}$ are written as

$$\underset{\sim}{u}^{(n)} = \underset{\sim}{U}^{(n)} e^{i(kx_1 - \omega t)} \quad ; \quad \underset{\sim}{t} = \underset{\sim}{T}\, e^{i(kx_1 - \omega t)} \qquad \text{(II-10)}$$

In view of the Legendre polynomical expansion the displacements on the both sides of a layer can be written as

$$w^{\pm} = u_1^{(0)} \pm u_1^{(1)} \quad ; \quad \eta = \pm 1$$

$$v^{\pm} = u_2^{(0)} \pm u_2^{(1)} \quad ; \quad \eta = \pm 1 \tag{II-11}$$

and the displacement w and v can also be given as

$$w = W e^{i(kx_1 - \omega t)}$$

$$v = V e^{i(kx_1 - \omega t)} \tag{II-12}$$

If we substitute Equs. (II-10, 11,12) into Eq. (II-9) we find

$$(-C_{11}\kappa^2+\bar{\omega}^2)(W^+ + W^-) + C_{12} i\kappa (V^+ - V^-) + b(T_{12}^+ - T_{12}^-) = 0$$

$$-C_{12} i\kappa (W^+ + W^-) + \frac{1}{3}(-3C_{22}+\bar{\omega}^2)(V^+ - V^-) + b(T_{22}^+ + T_{22}^-) = 0$$

$$C_{66} i\kappa (W^+ - W^-) + (-C_{66}\kappa^2+\bar{\omega}^2)(V^+ + V^-) + b(T_{22}^+ - T_{22}^-) = 0 \tag{II-13}$$

$$\frac{1}{3}(-\hat{C}_{11}\kappa^2 - 3C_{66}+\bar{\omega}^2)(W^+ - W^-) - C_{66} i\kappa (V^+ + V^-) + \frac{C_{12}}{3C_{22}} i\kappa b(T_{22}^+ - T_{22}^-) + b(T_{21}^+ + T_{21}^-) = 0.$$

where $\bar{\omega}^2$ and κ are defined by

$$\bar{\omega}^2 = \rho b^2 \omega^2$$

$$\kappa = bk$$

The above equation is the final form of governing equation written in terms of wave number, frequency and amplitudes of displacements on both sides of a layer.

Plate Analysis. Remembering that above analysis is for any arbitrary layer in a plate, say the nth layer, equation (II-13) can be immediately written as a set of difference equations, [15],

$$
\begin{aligned}
&(-C_{11}\kappa^2+\bar{\omega}^2)(W_n+W_{n-1}) + C_{12}i\kappa(V_n-V_{n-1}) + (\tau_n-\tau_{n-1}) = 0\\
&-C_{12}i\kappa(W_n+W_{n-1}) + \frac{1}{3}(-3C_{22}+\bar{\omega}^2)(V_n-V_{n-1}) + (\sigma_n+\sigma_{n-1}) = 0\\
&C_{66}i\kappa(W_n-W_{n-1}) + (-C_{66}\kappa^2+\bar{\omega}^2)(V_n+V_{n-1}) + (\sigma_n-\sigma_{n-1}) = 0\\
&\frac{1}{3}(-\hat{C}_{11}\kappa^2-3C_{66}+\bar{\omega}^2)(W_n-W_{n-1}) - C_{66}i\kappa(V_n+V_{n-1}) + \frac{C_{12}}{3C_{22}}i\kappa(\sigma_n-\sigma_{n-1}) + (\tau_n+\tau_{n-1}) = 0
\end{aligned}
\qquad \text{(II-15)}
$$

where we replaced $bT_{21} = \tau$ and $bT_{22} = \sigma$. Here we notice that the continuity conditions in displacements and stresses across the boundary between layers are identically satisfied by these difference equations.

Dispersion Relationship. For a plate made of N layers, in general, Eq. (II-15) gives 4N equations written in terms of 4(N+1) variables $(W_o, V_o, \tau_o, \sigma_o, W_1, V_1, \cdots, \tau_N, \sigma_N)$. Boundary conditions drop 4 variables among them so that 4N unknowns can be determined by 4N homogeneous equations when the determinant of coefficient matrix vanishes, which provides the desired dispersion relationship between frequency ω, and wave length $2\pi/k$.

One layer Plate The dispersion relationship for a plate made of one layer (as shown in Fig. 8) can be found by setting $N = 1$ in Eq. (15) with corresponding boundary conditions, i.e. $\sigma_o = \tau_o = \sigma_1 = \tau_1 = 0$ and the resulting equations are now written in matrix form as follows:

$$\begin{bmatrix} (-C_{11}\kappa^2+\bar{\omega}^2), & C_{12}i\kappa & 0 & 0 \\ -C_{12}i\kappa & \frac{1}{3}(-3C_{22}+\bar{\omega}^2) & 0 & 0 \\ 0 & 0 & C_{66}i\kappa & (-C_{66}\kappa^2+\bar{\omega}^2) \\ 0 & 0 & \frac{1}{3}(-\hat{C}_{11}\kappa^2-3C_{66}+\bar{\omega}^2), & -C_{66}i\kappa \end{bmatrix} \begin{Bmatrix} W_1+W_o \\ V_1-V_o \\ W_1-W_o \\ V_1+V_o \end{Bmatrix} = \begin{Bmatrix} 0 \\ 0 \\ 0 \\ 0 \end{Bmatrix} \tag{II-16}$$

Then by setting the coefficient matrix zero we obtain the dispersion relations as

$$\begin{aligned} C_{12}^2\kappa^2 - \tfrac{1}{3}(-3C_{22}+\bar{\omega}^2)(-C_{11}\kappa^2+\bar{\omega}^2) &= 0 \\ C_{66}^2\kappa^2 - \tfrac{1}{3}(-\hat{C}_{11}\kappa^2-3C_{66}+\bar{\omega}^2)(-C_{66}\kappa^2+\bar{\omega}^2) &= 0 \end{aligned} \tag{II-17}$$

Here we notice that the first relationship corresponds to the state of deformation of $W_1 = W_o$ and $V_1 = -V_o$, which correspond to thickness extension of the plate or the symmetric mode, and the second describes the flexual deformation or antisymmetric mode. The exact theory of plate gives an infinite number of dispersion relations but since we only kept inertia effects up to 1st order for both components of displacement, we have only the first four dispersion relationships.

Dispersion relationships and corresponding phase velocities for an isotropic material with Poisson's ratio 1/4 (namely $\lambda = u$) are given in

Fig. 9a and b. Relationships for a 55% graphite fiber-epoxy matrix composite with layup angle 0° and 45° are shown in Fig. 10a, b and 11a, b. Note here that modified frequency $\bar{\omega}$ and phase velocity c are normalized again by C_{66}. From these figures we clearly see that $\bar{\omega}_1/\kappa$ (or c_1) approachs the limit $\sqrt{C_{11}/C_{66}}$ which is the dilatation wave speed in case of an isotropic plate and quasi-dilatation for anisotropic plate when the wave number κ becomes large (or the wave length becomes small compared with the layer thickness b). Also notice that $\bar{\omega}_4/\kappa$ (or c_4), which for $kb \ll 1$ is a bending wave approaches a shear wave for $kb \gg 1$. Fig. 11a and b show the effect of anisotropy on the dispersion relationships and the wave speeds of the dilatation (and quasidilatation) waves when the layup angle changes from 0° to 90° (see Table II).

Two-Layer Plate. In this case we obtain 8 equations by putting n = 0 and 1 in (II-15). The boundary conditions require $\tau_o = \sigma_o = \tau_2 = \sigma_2 = 0$ (see Figure 8). The 8 equations are written for 8 unknowns $(W_o, V_o, W_1, V_1, \tau_1, \sigma_1, W_2, V_2)$ and again by following the same procedure as in one-layer case we find the dispersion relations as

$$\frac{1}{3}\{(-\hat{C}_{11}\kappa^2 - 3C_{66} + \bar{\omega}^2) + \frac{C_{12}C_{66}}{C_{22}}\kappa^2\}\ [-C_{12}^2\kappa^2 + (\bar{\omega}^2 - C_{11}\kappa^2)\{\frac{1}{3}(-3C_{22} + \bar{\omega}^2) + (\bar{\omega}^2 - C_{66}\kappa^2)\}]$$

$$-(\bar{\omega}^2 - C_{11}\kappa^2)\{C_{66}^2\kappa^2 + \frac{C_{12}C_{66}}{3C_{22}}\kappa^2(\bar{\omega}^2 - C_{66}\kappa^2)\} = 0$$

$$C_{66}^2\kappa^2(-3C_{22} + \bar{\omega}^2) - (\bar{\omega}^2 - C_{66}\kappa^2)(-3C_{22} + \bar{\omega}^2)\{(\omega^2 - C_{11}\kappa^2) + \frac{1}{3}(-\hat{C}_{11}\kappa^2 - 3C_{66} + \bar{\omega}^2)\}$$

$$+ 3(\bar{\omega}^2 - C_{66}\kappa^2)C_{12}^2\kappa^2 = 0$$

Dispersion relationships for the isotropic plate and anisotropic plate

with layup angle $0°$ and $45°$ are plotted in Fig.13a,b,14a,b, and 15a,b.

N-Layer Plate. In general, we can obtain a $2(N+1)$ order polynomial of $\bar{\omega}^2$ by expanding a $(4N) \times (4N)$ determinant and find $2(N+1)$ dispersion relations. But unfortunately this process involves considerably complicated algebra and it may be necessary to develop a computer technique to find roots of an equation in determinant form (not in polynomial form).

A difference equation approach can be used to solve the N set of four simultaneous first order difference equation given by Eq. (II-15). This proceedure is neat and can be generalized for any number of layers but the last step of this approach, where a long polynomial is to be solved again, is not simpler than previous direct method.

Section 4.- Difference Equation Approach for Impact Problem

Solutions of Difference Equations. Since the simultanious difference equations given by Eq. (II-15) are linear and all the coefficients are constants, we can try the following form for their solution [15]

$$\begin{aligned} \tau_n &= A\, e^{2i\beta n} \\ \sigma_n &= B\, e^{2i\beta n} \\ W_n &= C\, e^{2i\beta n} \\ V_n &= D\, e^{2i\beta n} \end{aligned} \qquad \text{(II-19)}$$

where β is complex, in general. By substitution of these solutions into Eq. (II-15) we have

$$\begin{bmatrix} (-C_{11}\kappa^2+\bar{\omega}^2)\cos\beta, & -C_{12}\kappa\sin\beta, & 0 & i\sin\beta \\ -C_{66}\kappa\sin\beta, & (-C_{66}\kappa^2+\bar{\omega}^2)\cos\beta, & i\sin\beta & 0 \\ \frac{i}{3}(-C_{11}\kappa^2-3C_{66}+\bar{\omega}^2)\sin\beta, & -C_{66}i\kappa\cos\beta, & -\frac{C_{12}}{3C_{22}}\kappa\sin\beta, & \cos\beta \\ -C_{12}i\kappa\cos\beta, & \frac{i}{3}(-3C_{22}+\bar{\omega}^2)\sin\beta, & \cos\beta, & 0 \end{bmatrix} \begin{Bmatrix} C \\ D \\ A \\ B \end{Bmatrix} = \begin{Bmatrix} 0 \\ 0 \\ 0 \\ 0 \end{Bmatrix} \qquad \text{(II-20)}$$

Again if we set the value of the determinant zero we find the following equations for β, $\bar{\omega}$ and κ .

$$a_1\cos^4\beta + a_2\sin^2\beta\cos^2\beta + a_3\sin^4\beta = 0 \qquad \text{(II-21)}$$

$$a_1 = (-C_{11}\kappa^2+\bar{\omega}^2)(-C_{66}\kappa^2+\bar{\omega}^2)$$

$$a_2 = \alpha_1 + \alpha_2 - \alpha_4 C_{12}\kappa - C_{12}C_{66}\kappa^2$$

$$a_3 = \frac{\alpha_3}{3}(-3C_{22}+\bar{\omega}^2)$$

$$\alpha_1 = \{-C_{12}^2\kappa^2 + \frac{1}{3}(-C_{11}\kappa^2+\bar{\omega}^2)(-3C_{22}+\bar{\omega}^2)\}$$

$$\alpha_2 = \{-C_{66}^2\kappa^2 + \frac{1}{3}(-\hat{C}_{11}\kappa^2-3C_{66}+\bar{\omega}^2)(-C_{66}\kappa^2+\bar{\omega}^2)\}$$

$$\alpha_3 = \{\frac{1}{3}(-\hat{C}_{11}\kappa^2-3C_{66}+\bar{\omega}^2) + \frac{C_{12}C_{66}}{3C_{22}}\kappa^2\}$$

$$\alpha_4 = \{C_{66}+(-C_{66}\kappa^2+\bar{\omega}^2)\frac{C_{12}}{3C_{22}}\kappa\}$$

Then we can find 4 values of β (say $\pm\beta_1(\pm\beta)$ and $\pm\beta_2(\pm\alpha)$) with given values of $\bar{\omega}$ and κ. Accordingly solutions given by (II-19) can be written as

$$\begin{aligned}
\tau_n &= A_1e^{2i\beta n} + A_2e^{-2i\beta n} + A_3e^{2i\alpha n} + A_4e^{-2i\alpha n} \\
\sigma_n &= B_1e^{2i\beta n} + B_2e^{-2i\beta n} + B_3e^{2i\alpha n} + B_4e^{-2i\alpha n} \\
W_n &= C_1e^{2i\beta n}C_2e^{-2i\beta n} + C_3e^{2i\alpha n} + C_4e^{-2i\alpha n} \\
V_n &= D_1e^{2i\beta n} + D_2e^{-2i\beta n} + D_3e^{2i\alpha n} + D_4e^{-2i\alpha n}
\end{aligned} \qquad \text{(II-22)}$$

Next when we substitute these solutions to our original difference equations we can find the relationships between A_i, B_i, C_i and D_i. The boundary conditions on the top and bottom faces of the plate require calculation of τ_n and σ_n, and they are given by

$$\sigma_n = B_1 e^{2i\beta n} + B_2 e^{-2i\beta n} + B_3 e^{2i\alpha n} + B_4 e^{-2i\alpha n}$$

$$\tau_n = X(\beta)(B_1 e^{2i\beta n} - B_2 e^{-2i\beta n}) + X(\alpha)(B_3 e^{2i\alpha n} - B_4 e^{-2i\alpha n}) \qquad \text{(II-23)}$$

with

$$X(\beta) = \frac{\alpha_2(-C_{11}\kappa^2+\bar{\omega}^2)\cos^2\beta + \alpha_1\alpha_3\sin^2\beta}{(\alpha_2 C_{12}\kappa + \alpha_1 C_{66}\kappa)\cos\beta\sin\beta} \qquad \text{(II-24)}$$

where the unknown constants B_i's have to be determined from boundary conditions.

Dispersion Relationship and Impact Problems. The dispersion relation for a composite plate consisting of N layers can be found immediately by setting $\sigma_0 = \tau_0 = \sigma_N = \tau_N = 0$ which leads us to

$$\Delta \equiv \begin{bmatrix} 1 & 0 & 1 & 0 \\ 0 & X(\beta) & 0 & X(\alpha) \\ \cos 2\beta N & i\sin 2\beta N & \cos 2\alpha N & i\sin 2\alpha N \\ -X(\beta)\sin 2\beta N, & X(\beta)\cos 2\beta N, & i\,X(\alpha)\sin 2\alpha N, & X(\alpha)\cos 2\alpha N \end{bmatrix}$$

$$= 2X(\alpha)X(\beta)(1-\cos 2\alpha N \cos 2\beta N) - \{X^2(\alpha)+X^2(\beta)\}\sin 2\beta n \sin 2\alpha N \qquad \text{(II-25)}$$

$$= 0.$$

where β and α are obtained by solving (II-21).

This difference equation method can be applied to the impact problem without any further difficulties by using integral transforms (Fourier transform in x_1 and Laplace transform in time) instead of harmonic wave analysis. The resulting equations are the same as (II-23) and B_i's can be determined from σ_o, τ_o, σ_N, τ_N which are now the integral transforms of impact functions. For the present report we have chosen a line impact along the x_3-axis, i.e.,

$$t_{22} = -P_o\left[1-\left(\frac{x_1}{a}\right)^2\right]\sin\frac{\pi t}{\tau_o} \quad ; \quad \text{on + side of } N^{th} \text{ layer,} \qquad \text{(II-26)}$$

$$\text{for } -a \le x_1 \le a \ , \ 0 \le t \le \tau_o$$

for the only nonvanishing impact function. Therefore the resulting boundary conditions are $\sigma_o = \tau_o = \tau_N = 0$ and $\sigma_N = \hat{\bar{t}}_{22}$ which is the integral transform of t_{22}. Once the B_i's are determined, the displacement fields and stress fields can be computed by inversion of the integral transform. For the present problem the inversion cannot be accomplished analytically because of the complexity of transformed function, but since the impact function given by Eq. (II-26) has finite rise time, duration and extent both in time and space, inversion can be carried out numerically by use of Fast Fourier Transform techniques.

Section 5. Numerical Results

Numerical inversion of the solution for the stresses in a multilayer plate was carried out for a two layer model of a composite plate. Each layer may contain many plys, but for the unidirectional fiber layup case each layer may represent a single ply. The calculations were carried using equivalent anisotropic elastic constants for a 55% graphite fiber/epoxy

matrix composite plate. A two layer model allows direct calculation of midplane interlaminar shear and normal stresses.

The propagation of a wave after impact on a plate consisting of two steel layers is shown in Fig. 16 a ~ f* where we can see two distinct wave speeds; $c_1 (\doteq 5.33$ mm/μsec) for w's and σ_{11} and $c_2 (\doteq 2.67$ mm/μsec) for v's and σ_{12} while the dilatation wave in steel has a speed of $c_d = \sqrt{(\lambda+2\mu)/\rho} =$ 5.61 mm/μsec and the shear wave $c_s \sqrt{\mu/\rho} = 3.25$ mm/μsec. This indicates that the initial signals are propagating via the acoustic branch of the symmetric mode with an almost constant group velocity $c_1 = 1.63\ c_s = 5.31$ mm/μsec and the major signals are carried by the bending mode (the acoustic branch of the antisymmetric mode) whose group velocity is lower than c_s (as shown in Figure 9). Similar phenomena is also observed in case of an anisotropic composite.

Figure 17a, b show the interlaminar shear stress versus time for the 45° fiber layup case (load perpendicular to the fibers) and the change of interlaminar shear stress along the plate at various times after impact. Figures 18a, b present simular numerical data for the interlaminar normal stress. In Figure 18b one can see that directly under the load the normal stress is initially compressive but subsequently becomes tensile. This is due to reflection from the back surface which in the two layer plate model is an oscillation in the thickness direction. Such tensile stresses may account for spalling damage and ply separation.

Finally in figure 19 data are presented for the case of the load in the direction of the fibers. Here for the case of interlaminar shear t_{12}

---

* Propagations of w_o, σ_{11_2}, v_1 and v_o are almost exactly same as those of w_2, σ_{11_o} and v_2 with different signs in case of u and σ_{11} and they are not shown here.

one can see a distinct wave spreading along the plate in time. From the figure we find $c \doteq 1.3$ mm/μsec which is slightly lower than $\sqrt{C_{66}/\rho}$ as in the isotropic case mentioned before. Investigation of wave propagation through the thickness direction requires an increase in the number of layers and is underway at the writing of this report.

PART III

Dynamics of Bird Impact with Aircraft Engines

by

F.C. Moon, S.R. Fang-Landau

Part III - Dynamics of Bird Impact with Aircraft Engines

Section 1. Introduction

It is well known that bird impact on the fan blades of jet aircraft poses a serious threat to airline safety. This problem has been studied extensively using both dummy birds and actual carcasses, both in Great Britain [16] and in this country [17],[18]. It has been clearly demonstrated in these tests that gross damage to composite blades can occur on impact producing broken parts of blades which themselves can initiate sequential fracture of the rest of the blade set. Films of single blade encounter with bird carcasses or simulated bird material suggest that the bird may be modelled as a transient fluid mechanics problem. However, until recently very little analytical or computer modelling of bird impact was available in the technical literature. A large literature on computer modelling of transient fluid mechanics problems exists with application to rain impact and erosion [19-22] but little if any had been applied to the bird impact problem.

The objective of the Princeton program in this area was to search the fluid mechanics literature for solutions and computational techniques that could be used to predict the forces and pressures on the blade structure during bird impact. We had also hoped to use such forces to simultaneously predict both fluid (bird) and blade motion (and hense stresses) during impact. These goals were only partially met as will be discussed below. But the principal problem lies in the reliability of the forces and pressures obtained from the computer simulation programs.

Before a proper model can be chosen, one must examine some of the physical properties of common birds. A complete description would include

the effects of bones and feathers and noncalcified tissue such as muscle, tendon, and fat as well as vital organs. A mechanics description of such an object would include such descriptions as inhomgeneous, viscoelastic and nonlinear. A complete solution of the impact of such a material is not possible at this time. Using contemporary techniques, one can hope to obtain a fluid model which is homogeneous, viscous, and perhaps compressible.

Section 2. Physical Properties of Birds

Before examining potential mathematical models for bird impact studies we review some of the physical properties of common birds. A summary of weight and geometric properties of birds was given by Griffiths [23]. Elastic and inelastic properties of bones and muscles of many animals and birds has been compiled by Yamada [24]. Ultrasonic wave properties of fatty tissue and muscle material are found in a review by Fry and Dunn [25]. For further details the reader is directed to the growing literature in biomechanics, in particular the collection of reviews edited by Fung [26].

A summary of the information found in these references is presented in Table 1. It should be cautioned that the numerical values given are in general rough values and in some cases may not be representative of a class of birds because of the small number of specimens sometimes tested.

In summary the weights of birds range from 9 kgm (20 lb.) for a swan to 1/4 kgm (0.55 lb.) for a sparrow hawk. While the density of mammalian fat and muscle is close to that of water the overall density calculated by Griffiths [23] was found to be less than that of water. He attributed this to air sacs which he has estimated range from 10-20% of the volume of pigeons and ducks. The skeletal structure of flying birds comprises less then 10% of the weight [23]. More extensive data for chickens may be found in [16], since these are readily available in the commercial food industry. However, data based on chickens which are ground birds may be misleading if extrapolated to flying birds, which are often involved in foreign object damage to aircraft.

The ultimate compressive strength of the femur bone of domestic fowls and birds is about 6860 N/cm^2 (9,950 psi) in the longitudinal direction

and about 45% less in the transverse direction (Tables 26, 30 Yamada [24]). The elastic modulus in compression for an ostrich femur is 0.5 MN/cm^2 (0.76 10^6psi) [24], while the value in tension is 1.36 MN/cm^2 (2.0 10^6psi) in the wet condition. Values for other birds were not available.

The strength of bones under impact may be enhanced by the protection of skin. Currey [27] found that 37% more energy was required to break rabbit bones protected with skin under impact than those without protection.

While bone may be treated as an elastic material, muscle and tendon are highly nonlinear materials. The ultimate tensile strength of tendon for domestic ducks is around 6370 N/cm^2 (9200 psi) with 6.7% elongation (Table 73 Yamada [24]).

The ultrasonic wave speed in mammalian fat and muscle is around 1500 m/s which is near that of water [25]. However the decay of ultrasonic waves in fat and muscle is much greater. At 1 MHz the characteristic decay distance is 7 and 20 cm for muscle and fat respectively compared to 4000 cm for water. Thus the water hammer model, employed in rain impact problems, which has a shock wave generated in the water on impact, may not be appropriate for bird impact because the large damping would smooth out or impede the attempt of the waves to form shocks. Further the presence of bone would further disperse any shocks developed by scattering the waves.

The viscous nature of soft tissue is also much greater than water and is estimated to be as high as 150 poise compared to 10^{-2} poise for that of water or 15 poise in the case of glycerine. However a more realistic model would certainly include viscoelastic effects which have been measured for certain biological materials [26] but are not reported here since only fluid models for birds will be discussed.

Section 3. Bone Impact Model

If the bird is to be treated as a liquid it must be shown that the impact of skeletal structure of the bird with the fan blade will generate stresses greater than the strength of the bone material. To model this we consider the bone as an elastic cylinder of radius R_2 under impact with the fan blade material of radius of curvature R_1. Treating the bone as elastic will obtain an upper bound on the stresses that would have to be sustained by the bone in order to remain intact.

The solution for the impact of two cylinders, as shown in Figure 20 may be found in the monograph on impact by Goldsmith [28]. The impact theory presented in [28] is based on that of Hertz which starts with the contact force between two elastic solids

$$F = k_2 \alpha^{3/2}$$

where α is the relative approach of the two bodies and k_2 is a constant depending on the elastic constants of the composite and bone, and the geometry R_1, R_2. One of the results of this theory is the time of contact τ

$$\tau = \frac{2.943}{V}\left[\frac{5}{4}\frac{MV^2}{k_2}\right]^{2/5}$$

where V is the normal velocity and M is the mass of the bone cylinder. The results are shown in Figure 21a,b. One can see that the contact times are less than 10^{-5} sec compared with the time of flight of the bird mass past the blade of around 10^{-3} sec.

The maximum compressive stress can also be calculated with the Hertz theory. The details are contained in [28] and are not shown here. The results are shown in Figure 21b for two cylinders with their axes at 90° to each other. Here we used $R_2 = 0.64$ cm for the radius of the bone, and 20 gm for the mass of impacting cylinder and 0.41 MN/cm^2 (.6 x 10^{6}psi) for compressive elastic moduli of the bone [24]. The blade material was assumed to be graphite/epoxy. As one can see, the induced stress is order of 10^9 Newton/m^2, (10^5 psi) when the impact velocity is somewhere around 100 m/sec. This stress is much higher than the ultimate strength of the bone in a transverse compressive load ($5*10^3$ Newton/cm^2) which implies that the failure of the bone is immediate.

This rough calculation supports the idea that at speeds greater than 50 m/sec the bird may be modelled as a fluid since in any encounter of bone with the blade the strength of the bone will be greatly exceeded.

Section 4. Liquid Impact Models

The impact of a liquid object with a solid target has been the subject of study in problems of rain erosion [29]-[34] and micrometeorite impact in the high speed limit where the impacting object can be treated as a liquid. While water is usually treated as a nonviscous incompressible fluid at low speeds, during the high speed impact of rain drops the compressibility of the fluid becomes important and a shock wave propagates into the fluid upon impact with the solid in a manner similar to waterhammer in a pipe, Figure 22. If the impacting fluid is moving with velocity V_o with respect to a rigid target, a one dimensional analysis of this problem predicts a pressure p given by

$$p = \rho_o V_o V_s$$

where V_s is the velocity of propagation of the shock wave in the fluid, and ρ_o is the density in the uncompressed part of the fluid. If the target is elastic the normal pressure on the solid is [34]

$$p = \frac{\rho_o V_o V_s}{(1 + \frac{\rho_o V_s}{\rho_e V_e})}$$

where

ρ_e is the density of the elastic medium and V_e is the the speed of sound in the elastic solid.

This analysis neglects motion of the fluid lateral to the incoming velocity. In fact if the speed is low enough the fluid will flow tangential to the surface rather than compress normal to the surface. In this hydrodynamic limit the maximum pressure is proportional to

$$p = \frac{\rho_o V_o^2}{2}$$

If enough fluid is present and some quasi steady flow is established near the center of impact a stagnation flow solution found in many books in fluid mechanics can be used [35], [36]. In this solution the tangential velocity along the solid increases linearly with distance from the center of impact.

Taylor [36] has shown that for the steady flow of a two dimensional jet of incompressible invisid fluid, impinging on a flat plate, the maximum pressure is $\rho V_o^2/2$ and occurs at the center of impact (Figure 23). The pressure falls off by about 75% at a distance equal to the width of the jet. Taylor has also presented data for oblique flow of a jet over a plate [36].

A number of computational models have been proposed to solve the equations of fluid mechanics for transient problems. A review of these techniques is given by Roache [37]. Amsden, Harlow and coworkers have developed an extensive computational scheme to solve transient incompressible viscous flow problems [19]-[21],[38] as well as for compressible flow problems. In one published example they have treated the transient splash of a liquid drop into a pool of water as well as the rigid plate impact. In these examples they have neglected viscosity. Their results show a radial velocity increasing linearly with radius similar to steady two and three dimensional stagnation flow.

Recently Huang, Hammit and Yang have presented a numerical scheme for a nonviscous compressible fluid and have published the results for the impact of a liquid drop onto a plate [22]. The solution predicts wave propagation into the liquid but no propagation into the solid target and no shocks or surfaces of velocity jumps are included. The results are quite extensive. However in the published discussion following the paper, Heymann disputes the findings, claiming that shocks should be formed and that waterhammer pressures $\rho V_o V_s$ should be reached. In [22] the calculated pressures in the fluid and on the plate are far below the theoretical waterhammer pressure. Also this program does not include the effects of viscosity which might be important to bird modelling.

Experimental studies of liquid impact pressures have been made including Brunton [31] and Smith and Kinslow [39]. Experimental bird simulation experiments have been preformed by Allcock and Collin [16] in Great Britain in which they measure the force history. They find that the maximum force is proportional to the kinetic energy of the bird or square of the initial velocity. Similar results have been reported by Hopkins in the United States [40].

The dependance of impact force on the initial kinetic energy of the bird can be explained using a rough momentum analysis. Thus if F_o is the average impact force, at the time of impact, and all the momentum under normal impact is turned 90° to the initial velocity vector then,

$$F_o \Delta t = M V_o \cdot$$

If we choose the time of flight D/V_o for the impact time Δt, where D is the diameter of the spherical bird say, then

$$F_o = \frac{M V_o^2}{D} \cdot$$

This model can be refined a little by assuming that the momentum is changed during impact at a rate proportional to the rate at which the bird volume crosses an immaginary plane surface. Thus if the bird is represented by a ellipsoid with a surface given by (see Figure 24)

$$\frac{r^2}{b^2} + \frac{(a-z)^2}{a^2} = 1$$

then if z is the distance along the symmetry axis of the ellipsoid from the impacting tip of the moving liquid the impact force is given by

$$F = V\rho \, \pi r^2(z) \frac{dz}{dt} = \rho \pi \, r^2(z) V^2$$

where r is given by the previous equation.

For a sphere the maximum force is given by

$$F_{max} = \frac{3}{2} \frac{M V_o^2}{D}$$

At V_o = 100 m/sec, D = 8 cm and $\rho = 10^3$ kgm/m^2 (density of water), $F_{max} = 16\pi 10^3$ Newtons ($\simeq 10^4$ lbf.) The average pressure of such a force over an area equal to $\pi D^2/4$ would be $P_o = \rho V_o^2 = 10^7$ N/m^2(1450 psi). The waterhammer pressure, assuming a shock wave formed in the water (V_s = 1500 m/s), would be $p_o = \rho V_o V_s = 1.5\ 10^8$ N/m^2(21,800 psi).

From the experiments of Alcoch and Collin [16] and Hopkins [40], the dependence of impact force on V_o^2 would imply that the average pressures were also so dependent and that the incompressible model would be appropriate for birds. The compressible model with waterhammer pressures would lead to a linear dependence of force on velocity.

However, since the discrepancy between the incompressible and compressible pressures are so great, further study on the effects of compressibility would be worthwhile. If the results of Huang, Hammitt and Yang [22] are proved right - namely that compressibility does not require shocks in the impacting liquid - then the experimental results on bird impact [16], [40] might be compatible with a compressible model.

Section 5. Results of Hydrodynamic Computer Model

The equations of fluid mechanics were solved using a finite difference technique for both plane and axisymmetric motions. The differential equations for incompressible viscous flow are given below (see e.g. [35] and Figure 25)

$$\frac{\partial u}{\partial z} + \frac{1}{r^\alpha}\frac{\partial r^\alpha u^2}{\partial r} + \frac{\partial uv}{\partial z} = -\frac{\partial \phi}{\partial r} + g_r + \nu \frac{\partial}{\partial z}\left(\frac{\partial u}{\partial z} - \frac{\partial V}{\partial r}\right)$$

$$\frac{\partial v}{\partial t} + \frac{1}{r^\alpha}\frac{\partial r^\alpha uv}{\partial r} + \frac{\partial v^2}{\partial z} = -\frac{\partial \phi}{\partial z} + g_z - \frac{\nu}{r^\alpha}\frac{\partial}{\partial r}\left[r^\alpha\left(\frac{\partial u}{\partial z} - \frac{\partial v}{\partial r}\right)\right]$$

u and v are velocities in the r, z directions respectively, g is the body force per unit mass and ϕ the pressure/density ratio. $\alpha = 0$ in plane coordinates; $\alpha = 1$ for axi-symmetric flow or cylindrical coordinates.

Incompressible flow requires

$$D \equiv \frac{1}{r^{\alpha}} \frac{\partial r^{\alpha} u}{\partial r} + \frac{\partial v}{\partial z} = 0$$

The finite difference algorithm used to simulate bird impact was Amsden and Harlow's simplified Marker and Cell program (SMAC) [20] with modification of the plotting routines, and boundary and initial conditions. The program was modified to accomodate the IBM360-91 computer and associated output devices including printer, plotting and microfilm hardware.

Initially 50 x 50 or 50 x 30 cells were set up. Each cell contains nine marker particles. When the number of marker particles per cell is less than 9 the cell is designated a surface cell. The fluid "bird" occupied up to 300 cells.

Both diffusive and convective sources of numerical instabilities in finite difference methods require that the time and distance intervals Δt, Δz satisfy certain inequalities as necessary conditions for stability [21], i.e.,

$$\frac{\nu \Delta t}{(\Delta z)^2} < \frac{1}{2}$$

$$\frac{V_o \Delta t}{\Delta x} < 1$$

where ν is the kinematic viscosity and V_o the initial velocity. A discussion of the stability of the MAC method has been given by Doly and Procht [41] In all calculations the above inequalities were satisfied. However a long time behavior of some of the numerical results did not always exhibit continuity in either position, velocity or pressure from time cycle to cycle raising questions about the reliability of the method. The SMAC method allows the use of either free slip or no slip boundary conditions, both of which were tried. While the bird is highly viscous, the skin and feathers might provide an effective free slip boundary condition.

Viscosity was kept as a parameter in these studies which was ignored in the splashing drop paper of Harlow and Shannon [19] and Huang et al. [22]. If D represents the diameter of the fluid cylinder or sphere, V_o the initial velocity, and ν the kinematic viscosity, then the Reynolds number

$$R = \frac{V_o D}{\nu}$$

used in the computer simulations ranged from $10^2 < R < 10^5$. As a example we used the data, V_o = 100 m/s, ν = 9.5 cm^2/sec viscosity of glycerine, density of water), D = 16 cm, R = 1.7 10^4 and $\Delta t = 5\ 10^{-6}$ s, Δz = 1 cm. For this case $\nu\Delta t/\Delta z^2 = 4.8\ 10^{-5}$ and $V_o\Delta t/\Delta z = 5\ 10^{-2}$ which are well below the stability criteria.

Two geometric configurations of fluid and target were studied. In the first, normal impact was studied for a fluid cylinder or fluid sphere. This geometry requires a solution for only half the fluid slug because of the inherent symmetry in the problem. Fig. 26 shows the time sequence of fluid and surface cells of a half sphere under normal impact with a rigid wall. In the second configuration a rigid rectangular target was set up and an cylindrical

fluid slug could impact the target at either normal or oblique incidence. In each case the fluid has an initial condition of uniform velocity with gravity ignored.

Figures 27, 28 shows a time sequence of marker particles for normal impact of fluid cylinder. The marker particles are shown in Figure 27 and the velocity vectors shown in Figure 28. Figure 29 shows oblique impact of a fluid cylinder on the edge of a rectangular object.

A time sequence of marker particles and velocity vectors is shown in Figures 30,31 for normal impact of a spherical fluid slug with a rigid plate.

For early time after impact the radial velocity at the plate shows a linear increase with radius which is characterisitic of stagnation point flow [35]. However as the impact proceeds there appears to develop an eddy current flow near the plate creating a dead zone of fluid. This can be seen in the velocity plot in Figure 32 , and the radial velocity plot verses radius in Figure 33 . Thus if the eddy flow is physical and not due to numerical instability, the normal impact velocity in the fluid actually reverses. A plot of normal velocity flow versus distance along the y axis for various times is shown in Figure 34. The velocity starts out uniform and then the normal velocity of the fluid near the plate approaches zero for small times and finally reverses flow for later times indicating an eddy flow. This in effect produces a rounded stationary fluid obstacle which deflects the remaining fluid away from the central plate impact point. This stationary central zone then tends to create a pressure that is fairly uniform with radius.

The stress in the fluid is given by

$$t_{ij} = -p\delta_{ij} + 2\mu \left[\frac{\partial U_i}{\partial x_j} + \frac{\partial U_j}{\partial x_i} \right]$$

where $\{U_i\}$ are the cartesian components of the velocity vector, μ is the viscosity coefficient, and p is the hydrostatic pressure. The pressure p in the SMAC finite difference scheme is found from an iterative procedure and is a direct output of the program along with the velocity vectors in each cell. A plot of pressure to density ratio versus radius is shown in Figure 35 for a Reynolds number equvalent to a 18 cm diameter fluid sphere moving at 100 m/s with the viscosity of glycerine at various times during impact up to about 1.0 ms compared to a time of flight of 1.8 ms. The pressure versus radius exhibits fairly smooth behavior for a given time, and somewhat constant pressure versus radius for time between 200 μs and 800 μs which was suggested by the eddy flow phenomena. However the center pressure versus time does not show a smooth behavior, at first increasing then decreasing and finally increasing again implying a high total force at the end of impact than at the beginning.

Since we had intended to used the total force to calculate the rigid body motion of the target (fan blade) we attempted to check the computer calculated pressures and resulting force using a different technique such as integrating Bernoullis equation for the pressure.

This equation involves calculating accelerations $\partial \underset{\sim}{v}/\partial t$ which must be found from two sequential time solutions for $\underset{\sim}{v}$. The accelerations calculated in this manner however were not reliable and did not lead to a check of the pressure distributions.

Another attempt involved adding up the total momentum $\Sigma\Sigma v(I,J)$ overall the cells (Figure 36). The total normal force is then

$$F_n = \rho \frac{\Sigma\Sigma[v^{(2)}(I,J)-v^{(1)}(I,J)]}{t_2-t_1} \quad .$$

This too produced an erratic force behavior and did not provide a satisfactory way to check the calculated pressures.

However if a smooth curve is fitted to the momentum vs. time data, (Figure 36) and the force calculated from this function, a continuous impact force history is obtained. In addition this force history compares reasonably well with the integrated pressure profiles found from the numerical calculation (Figures 37, 38). The force at first peaks and then attains a constant value for times up to about 20% of the transit time of the fluid cylinder. Thus while the pressure-time data from the finite difference code is erratic from cycle to cycle, it appears to be at least consistent with the velocity or momentum data when averaged over a number of cycles.

The effect of slip or no slip boundary conditions on the pressure distribution on the plate is shown in Figure 39, for a fluid cyclinder under normal impact. For early times the pressures are about equal but beyond 200 μsec the free slip impact results in higher pressures.

Another observation for the full cylinder case is the development of unsymmetrical radial flow along the plate for normal impact Figure 40. (Such symmetry is of course guaranteed for the half cylinder or sphere case). While such instabilities may develop in an actual flow, in the numerical solution this unsymmetrical flow probably indicates a numerical instability

in the finite difference code.

In summary velocity plots of viscous incompressible fluid impact with rigid obstacles using finite difference codes would appear to offer a way to calculate the forces due to bird impact on fan blades. However lack of any exact analytical results to check the calculated pressures and forces raises doubts about the efficacy of using this approach to predict deformation of fan blades. The experience of the rain impact problem, in which there is great controversy over the actual pressures produced during impact, suggests that finite difference codes may not provide a definitive answer for the bird impact problem either without further analytical, experimental or other computational check such as a finite element analysis.

Page intentionally left blank

Conclusions and Recommendations

1. The analytic modelling of constrained layer damping as a mechanism for decreasing stresses in composite plates due to impact shows promise of significant reduction of stresses for edge impact forces. It is recommended that constrained layer damping be studied for central impact of composite plates. To test these results, it is suggested that a limited experimental program be initiated on the concept of shear layer damping of impact stresses.

2. The multi-layer generalization of a Mindlin plate appears to be a straight forward method of modelling a multiply composite plate for the study of impact response. The combined use of finite difference techniques in the thickness direction and the fast Fourier transform in the plane of the plate results in a fairly efficient method of studying interlaminar stresses and wave propagation through the plate. This technique might be modified to investigate the effect of interlaminar cracks or flaws on the impact stresses in the plate.

3. Films and calculations of stresses in bird bones due to impact seem to suggest a fluid model for the study of forces due to bird impact of aircraft structures. However analytical solutions for transient impact of a slug of fluid are not known. As shown in this report finite difference computer codes can be used to obtain velocity, pressure and force histories. These "computer experiments" show the development of instabilities and eddy flow. in the fluid during impact. Whether such motions are real or due to computational instability cannot be decided without comparison with either experimental results or other numerical

schemes such as the finite element method.

A search of the computational fluid mechanics literature reveals a number of potentially useful computer codes for the study of bird impact forces. These codes, if they proved accurate, could save considerable sums in experimental testing. However several questions concerning numerical stability and accuracy of the impact pressures and forces must be carefully examined before they are embraced. While a bird is made up of highly viscous materials, the effect of compressiblity and of shock propagation into the fluid bird needs to be examined.

REFERENCES

[1] F.C. Moon: "Wave Surfaces Due to Impact on Anisotropic Plates". J. Comp. Mat. Vol. 6, p. 62 (1972).

[2] F.C. Moon: "Theoretical Analysis of Impact in Composite Plates", Technical Report to NASA Lewis Res. Center, cont. NAS 3-14331, Princeton University (1973).

[3] F.C. Moon and C.K. Kang "Analysis of Edge Impact Stresses in Composite Plates", Technical Report to NASA Lewis Res. Center cont. NGR 31-001-267, Princeton University (1974).

[4] M.-J. Yan : "Constrained-Layer Damping in Sandwich Beams and Plates. Doctoral Dissertation, Princeton University, June 1972, Report No. AMS-1031.

[5] M.-J. Yan , Dowell, E.H.: "High damping measurements and a preliminary evaluation of an equation for constrained larger damping", AIAA Journal Vol. 11, No. 3, p. 388-390, March 1973.

[6] R.D. Mindlin: "High Frequency Vibrations of Crystal Plates", Quart. Appl. Math., Vol. 19, p. 51 (1961).

[7] S.B. Dong and R.B. Nelson: "On Natural Vibrations and Waves in Laminated Orthotropic Plates," J. Appl. Mech., Trans. ASME, p. 739 (1972).

[8] R.D. Mindlin and M.A. Medick: "Extension Vibrations of Elastic Plates", J. Appl. Mech., Trans ASME, p. 561 (1972).

[9] P.C.Y. Lee and Z. Nikodem: "An Approximate Theory for High Frequency Vibrations of Elastic Plates", Int. J. Solids Struc., vol. 8, p. 581 (1972).

[10] J.E. White and F.A. Angona: "Elastic Wave Velocities in Laminated Media", J. Acout. Soc. Am., vol. 27, p. 310 (1955).

[11] C.T. Sun, J.D. Achenbach and G. Herrmann: "Continuum Theory for a Laminated Media", J. Applied Mech., Trans. ASME, p. 467 (1968).

[12] W.M. Ewing, W.S. Jardetzky and F. Press: Elastic Waves in Layered Media, McGraw Hill, 1957.

[13] L.Brillouin: Wave Propatation in Periodic Structures, Dover Publ. N.Y., 1946.

[14] W.T. Thomson: Vibration Theory and Applications, Prentice Hall, Englewood Cliffs, N.J., 1965.

[15] H. Levy and F. Lessman: Finite Difference Equations, MacMillan Co., 1961.

[16] A.W.R. Allcoch, Collin, D.M.: "The Development of a Dummy Bird for Use in Bird Strike Research", National Gas Turbine Establishment (United Kingdom) N.G.T.E. Report No. C.P. No. 1071., 1968.

[17] C.A. Steinhagen, C.T. Salemine: "Impact Resistance of Current Design 'Composite Fan Blades Tested under Short-Haul Operating Conditions' ", Contractor's Report to NASA from General Electric Co., Evendale, Ohio, NASA-CR-134533, July 1973.

[18] C.E. Meyer, M.J. Boulter, "Bird Control at the Airport", Aeronautics and Astronautics, p. 55-57, Dec .1973.

[19] F.H. Harlow, J.P. Shannon, "The Splash of a Liquid Drop", J. Appl. Phy. vol. 38, No. 10, Sept. 67, p. 3855-3860.

[20] A.A. Amsden, F.H. Harlow: "The SMAC Method: A Numerical Technique for Calculating Incompressible Fluid Flows. Los Alamos Sci. Lab. of Univ. Cal., Los Alamos, N.M., LA-4370, May 1970.

[21] F.H. Harlow, A.A. Amsden: Fluid Dynamics, Los Alamos Sci. Lab. of U. of Calif. L.A. 4700, June 1971.

[22] Y.C. Huang, F.G., Hammit, W.-J. Yang: "Hydrodynamic Phenomena During High-Speed Collison Between Liquid Droplet and Rigid Plane" - Trans. ASME J. of Fluids Engr., June 1973, pp. 270-294.

[23] R. Griffiths: "Properties of Bird Carcasses as Related to Bird Ingestion Problems of Aircraft Gas Turbines", (United Aircraft of Canada

Ltd. Report), Foreign Object Damage of Composites Workshop, Wright Patterson AF Base Dayton, Ohio, November 1974.

[24] H. Yamada, Strength of Biological Materials, Ed. by F.C. Evans, Williams and Wilkins Co., Baltimare, 1970.

[25] W.J. Fry, F. Dunn: "Ultrasound: Analysis and Experimental Methods in Biological Research, Chap. 6, Physical Techniques in Biological Research, W.L. Nastuk, Ed., Acad. Press, N.Y., vol. IV, 1962.

[26] Y.C. Fung, N. Perrone, M. Anliker, Editors, Biomechanics, Prentice Hall, Englewood Cliffs, N.J.

[27] J.P. Currey, "The Effect of Protection on the Impact Strength of Rabbit Bones," Acta Anat. 1968.

[28] W. Goldsmith: Impact, Arnold Publ. LTD., 1960.

[29] Engle, O.G.: "Basic Research on Liquid-Drop-Impact Erosion", NASA Contractor Report, CR-1559 form General Electric Co., Cinn., Ohio June 1970.

[30] Engel, O.G.,"Damage Produced by High-Speed Liquid-Drop Impacts", J. Appl. Phy., 44 (2) p. 692-704, February 1973.

[31] Brunton, J.H., "Deformation of Solids by Impact of Liquids at High Speeds," Symposium on Erosion and Cavitation, ASTM Special Tech. Pub. No. 307, 83-89, 1961.

[32] Rochester, M.C., and Brunton, J.H. "Surface Pressure Distribution During Drop Impingement," CUED/C-Mat/Tr.15, 1974. University of Cambridge. Presented at 4th International Conference on Rain Erosion and Related Phenomena, Meersburg, The Federal German Republic, 8-10

[33] F.J. Heymann: "On the Shock Wave Velocity and Impact Pressure in High Speed Liq[illegible] Solid Impact", Trans. ASME, J. of Basic Engr., p. 400-402, September 1968.

[34] N. Johnson, G.W. Vickers: "Transient Stress Distribution Caused by Water-Jet Impact", J. of Mech. Engr. Sci., vol. 15, No. 4, 1973, p. 302-310.

[35] Schlichting, H., Boundary Layer Theory, McGraw Hill Book Co., New York, 1955.

[36] G.I. Taylor: "Oblique [illegible] of a Jet on a Plane Surface", Phil. Trans. Roy. Soc. Lond., Series A., Math. and Phy. Sci., No. 1110, Vol. 260, July 1960, pp.

[37] P.J. Roache: Computational Fluid Dynamics, Hermosa Publ., Albuquerque, N.M. 87108.

[38] F.H. Harlow, A.A. Amsden: "A Numerical Fluid Dynamics Calculation Method for all Speeds," J. Comp. Phy. 8, p. 197-213, 1971.

[39] D.G. Smith, R. Kinslow, "Pressure Due to High Velcoity Impact of a Water Jet", Soc. Exp. Stress Anal. Meeting, Paper No. 2359, 1975.

[40] A. Hopkins, "Foreign Object Damage of Composites Workshop," Workshop, Wright Patterson AF Base, Dayton, Ohio, November 1974.

[41] B.J. Doly and W.E. Pracht, Phys. of Fluids, 1968.

TABLE I

Physical Properties of Birds

Name	Weight (kgm)	Reference
Common Gull	0.45	[23]
Wood Pigeon	0.45	[23]
Mallard Duck	1.1	[23]
Canada Goose	3.8 - 6.4	[23]
Whooper Swan	9	[23]

percent weight for chicken	Body	Wings	Legs	Head + Neck	Ref.
	67.0	6.4	8.6	8.0	[16]

Specific Properties

Name	Density gm/cm^3	Speed of Sound m/s	Rate of Decay (cm^{-1})	Viscosity poise $(10^{-1} NS/m^2)$	Ref.
Mammalian Tissue	1.07	1570	0.13(@ 1 MHZ)	150 p	[25]
Human Skull bone	1.7	3400	1.7(@ 1.2 MHZ) 7.8(@ 3.5 MHZ)		
				chicken blood	
Chicken Body	1.05			$3\text{-}5\ 10^{-2}p$	[16]
Glycerine (20°C)	1.26			15p	
Water (20°C)	1.0	1500	$25\ 10^{-5}$	$10^{-2}p$	[25]
Alum.	2.7	6400	0.2		
Lucite	1.18	2680			

Strength Properties

Name	Density	Tensite Strength (N/cm^2)	Compression (N/cm^2)	Elastic Modulus	Ref.
Chicken Muscle		59-98			[16]
duck tendon		6370			[24]
femur bone			6860		[24]
(domestic fowls)			long direction		
Ostrich femur				1.36 MN/cm^2 (tension)	[24]

TABLE II. - STRESS-STRAIN COEFFICIENTS FOR 55 PERCENT GRAPHITE

FIBER-EPOXY MATRIX COMPOSITE

(All constants to be multiplied by 10^6 psi, see Figure 7)

0° Layup					
27.95	0.3957	0.3957	0	0	0
	1.170	0.4601	0	0	0
		1.170	0	0	0
			0.3552	0	0
				0.7197	0
					0.3552

$\pm 15^\circ$ Layup					
24.56	0.4000	1.986	0	0	0
	1.170	0.4558	0	0	0
		1.374	0	0	0
			0.3552	0	0
				2.310	0
					0.3552

$\pm 30^\circ$ Layup					
16.48	0.4118	5.167	0	0	0
	1.170	0.4400	0	0	0
		3.093	0	0	0
			0.3552	0	0
				5.491	0
					0.3552

$\pm 45^\circ$ Layup					
8.197	0.4279	6.758	0	0	0
	1.170	0.4279	0	0	0
		8.179	0	0	0
			0.3552	0	0
				7.082	0
					0.3552

List of Figures

14a,b. Dispersion relationship and phase velocity for composite plate (two-layer model; layup angle 0°, 55% graphite/epoxy).

15a,b. Dispersion relationship and phase velocity of composite plate (two-layer model; layup angle 45°, 55% graphite/epoxy).

16. a ~ f. wave propagation in isotropic plate (two-layer steel plate); $C_{11} = C_{22} = \lambda + 2\mu = 3 \times 10^7$psi, $C_{12} = C_{66} = \mu = 10^7$psi; Plate thickness 0 = 1 cm; contact time t_c = 10 μsec, contact radius a = 4 cm.

17a,b. Interlaminar shear stress (τ_{12_1}/p_o) (two-layer composite model); plate thickness Δ = 1 cm. contact time τ_o = 20 μsec; contact radius a = 4 cm; 55% graphite/epoxy layup angle = 45°).

18a,b. Interlaminar normal stress (t_{11_1}/P_o) (same as Fig. 17).

19. Propagation of interlaminar shear stress (τ_1/p_1)(same as Fig. 17,18 90° layup).

20. Model for the impact of a bone cylinder with an aircraft wing or a turbine blade.

21a. Estimate of impact contact time versus speed for bird bones and graphite/epoxy composite.

21b. Estimate of impact contact stress versus speed for bird bones and graphite/epoxy composite.

22. Waterhammer model for fluid slug impact.

23. Distribution of pressure in the steady flow of a two dimensional jet against a flat plate (Taylor [36]).

24. Momentum model for impact force due to fluid impact with a flat plate.

25. Finite difference models for hydrodynamic fluid impact code.

26. Time sequence of marker particles for the impact of a fluid sphere against a rigid wall.

27. Time sequence of marker particles for the normal impact of a fluid cylinder against a rigid object.

28. Time sequence of velocity vectors for the normal impact of a fluid cylinder against a rigid object.

29. Time sequence of marker particles for the impact of a fluid cylinder with a rigid airfoil-like object.

30. Time sequence of marker particles for normal impact of a sphere with a rigid wall.

31. Time sequence of velocity vectors for the normal impact of a fluid sphere with a rigid wall.

32. Velocity vector map of the impact of a fluid sphere showing eddy flow near the rigid wall.

33. Radial velocity versus radius at the wall for the normal impact of a fluid sphere under free slip boundary conditions.

34. Normal velocity on the axis of a fluid sphere versus distance from a rigid wall.

35. Pressure distribution along a rigid wall due to impact of a fluid sphere.

36. Normal momentum versus time after the impact of a fluid cylinder with a rigid wall.

37. Pressure versus radius at various times during the impact of a fluid cylinder.

38. Normal impact force versus time for the normal impact of a fluid cylinder with a rigid wall. Comparison of pressure integration and momentum methods.

39. Comparison of fluid impact pressure distribution for slip and no slip boundary conditions.

40. Impact pressure distribution for normal impact of a fluid cylinder showing development of breakdown of symmetry of the numerical solution.

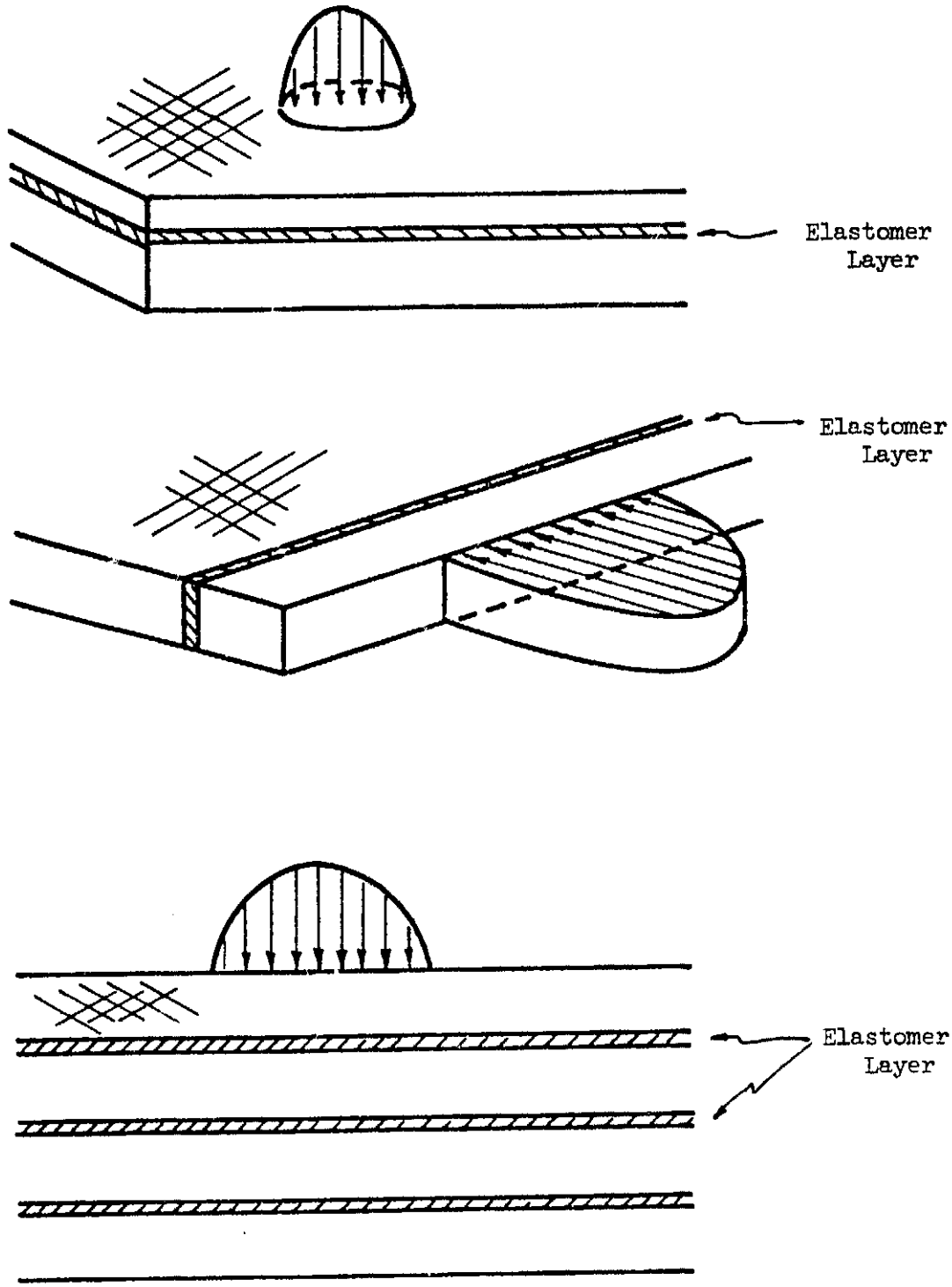

Figure 1. Viscoelastic Impact Energy Absorbing Models

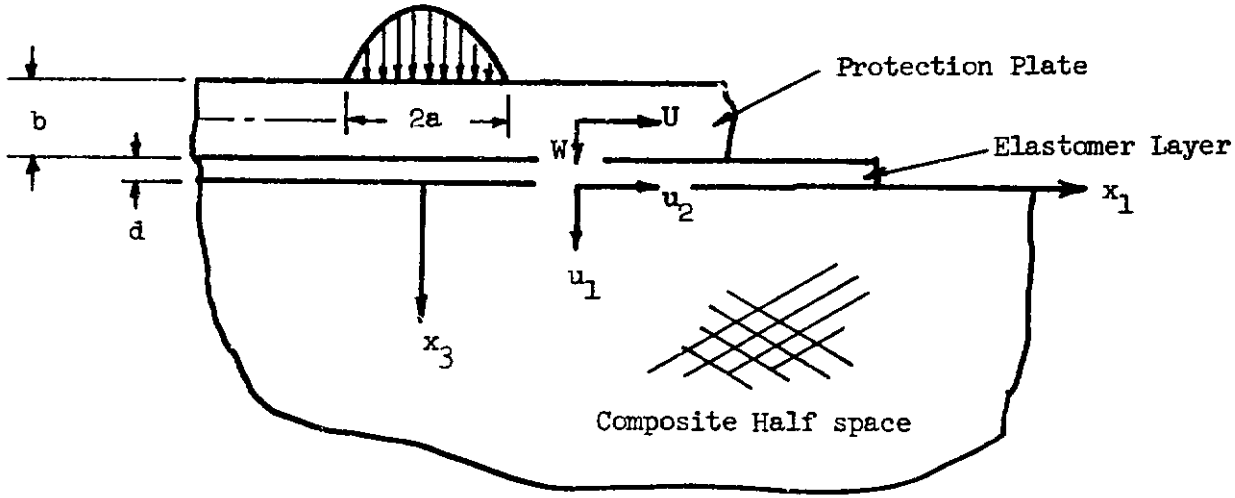

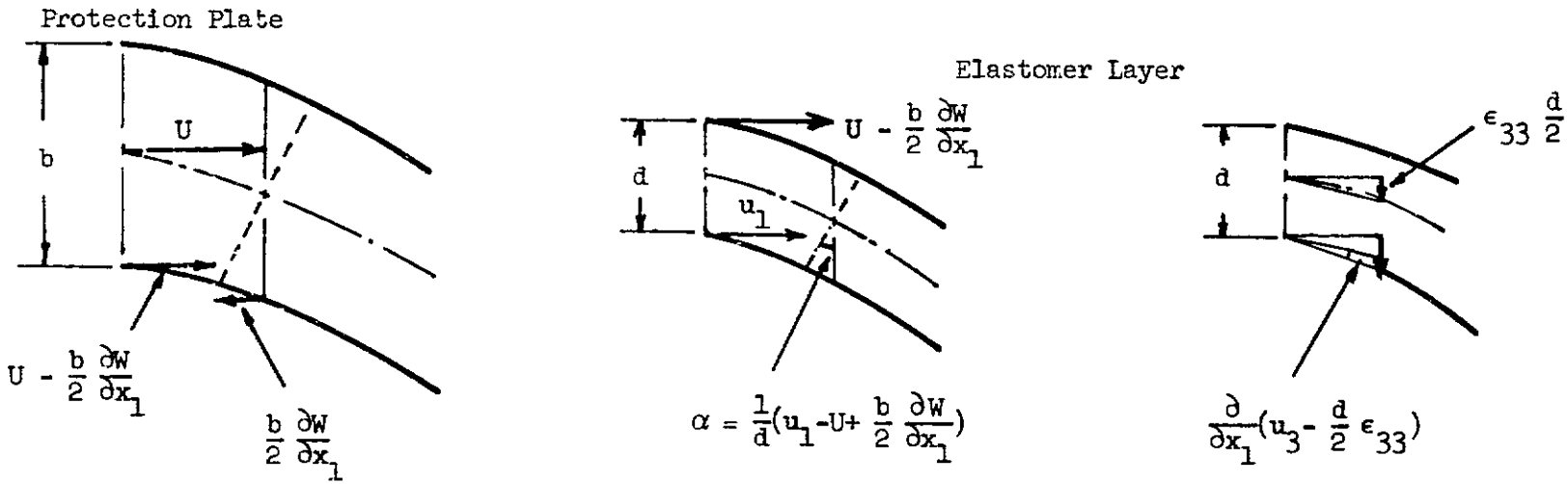

Figure 2. Constrained Layer Damping with Edge Protection

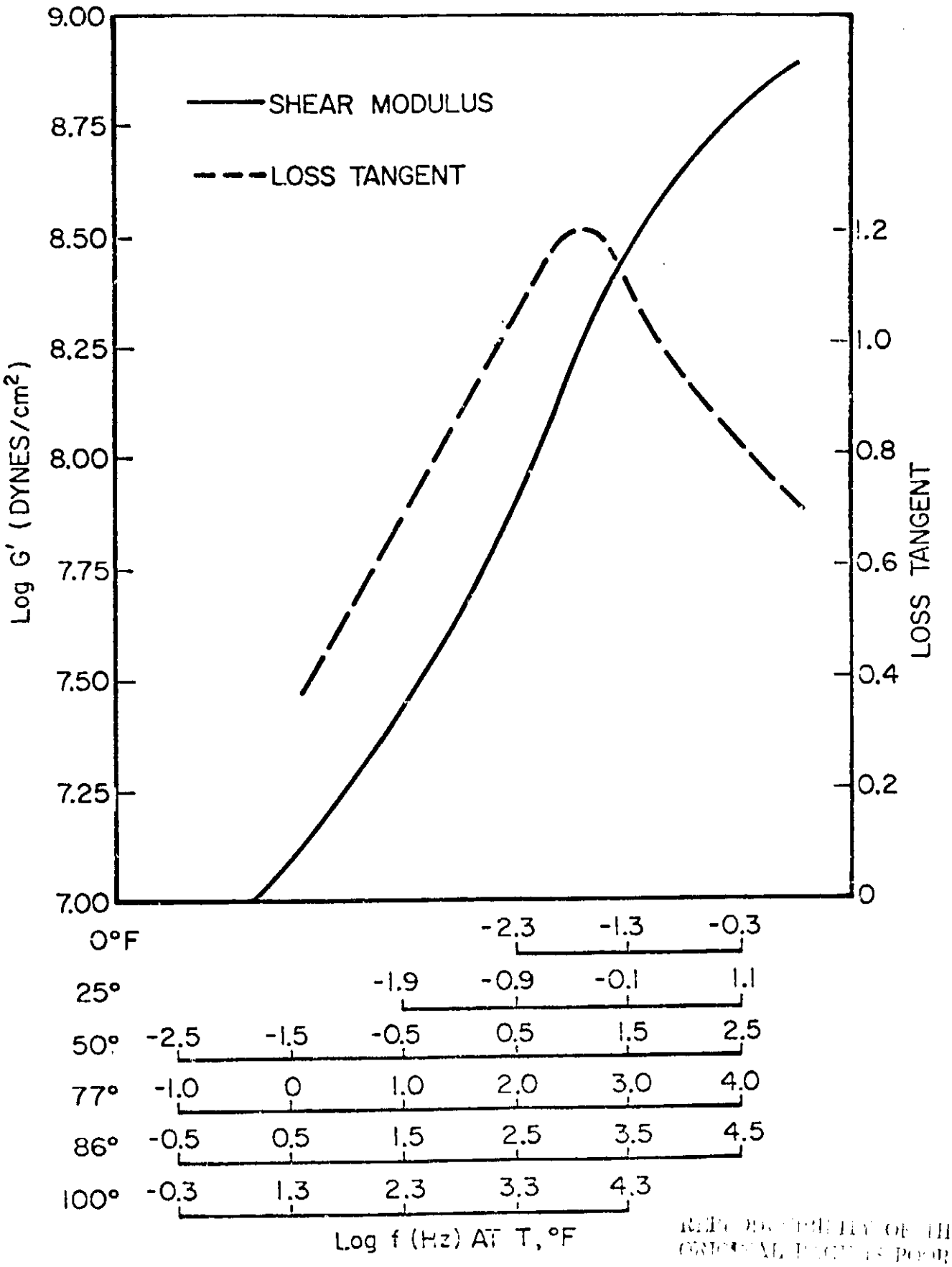

FIGURE 3. SHEAR MODULUS AND LOSS TANGENT AT T °F vs FREQUENCY FOR DUPONT LR3-604

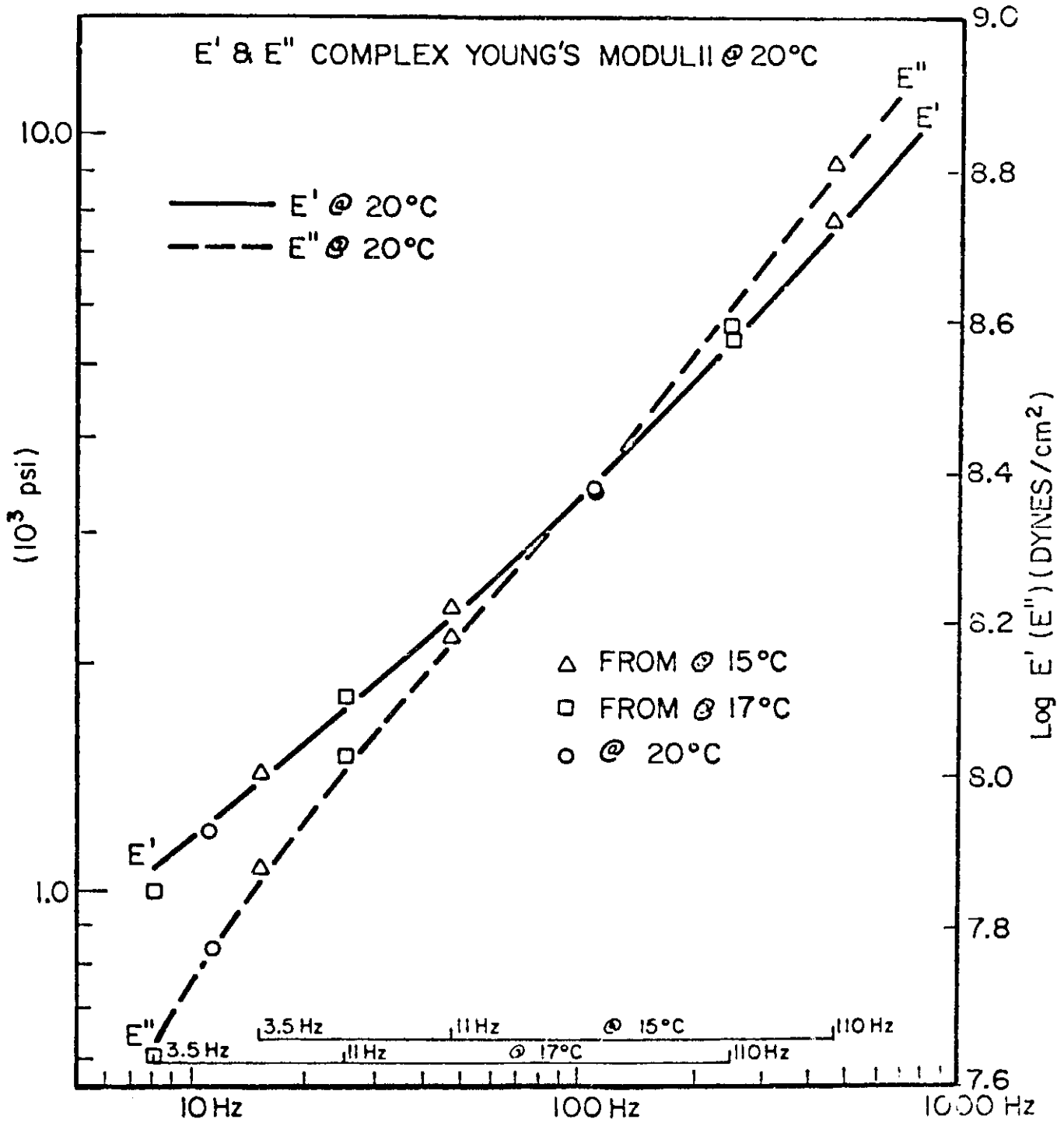

FIGURE 4. THE COMPLEX YOUNG'S MODULUS OF LR3-604 MEASURED

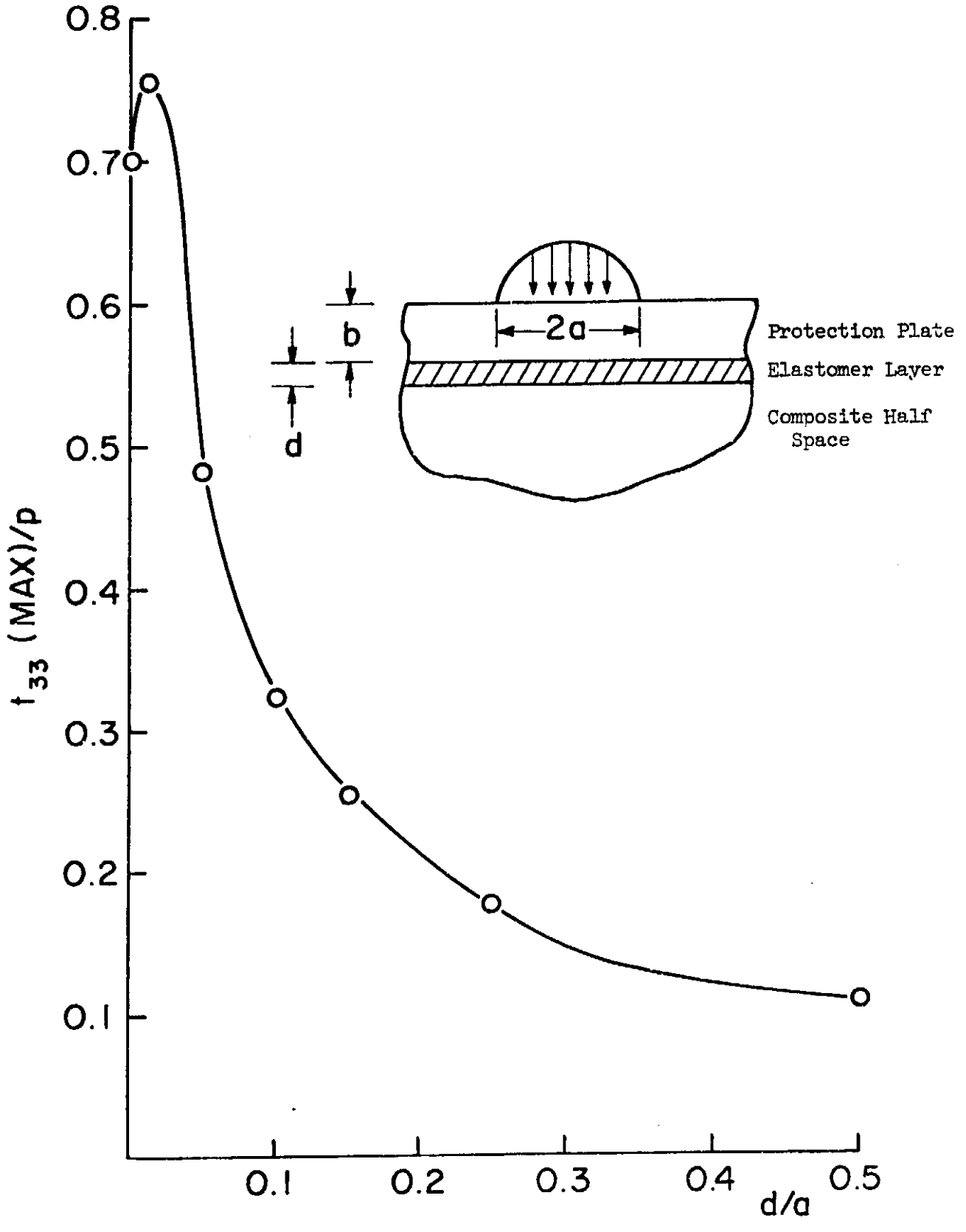

Figure 5. Maximum Normal Stress (t_{33}) in Elastomer Vs Elastomer Thickness

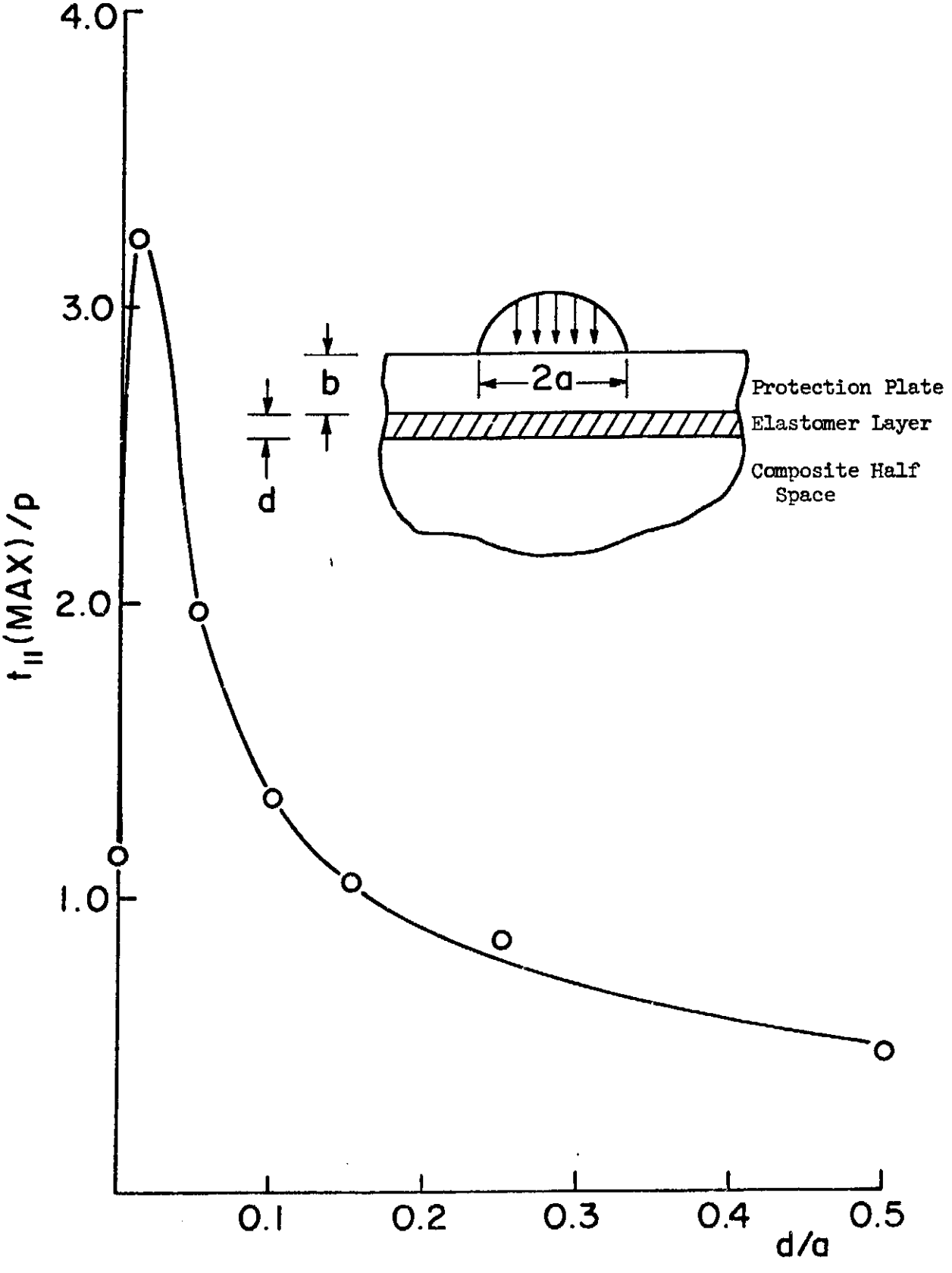

Figure 6. Maximum Normal Stress (t_{11}) in Elastomer Vs Elastomer Thickness

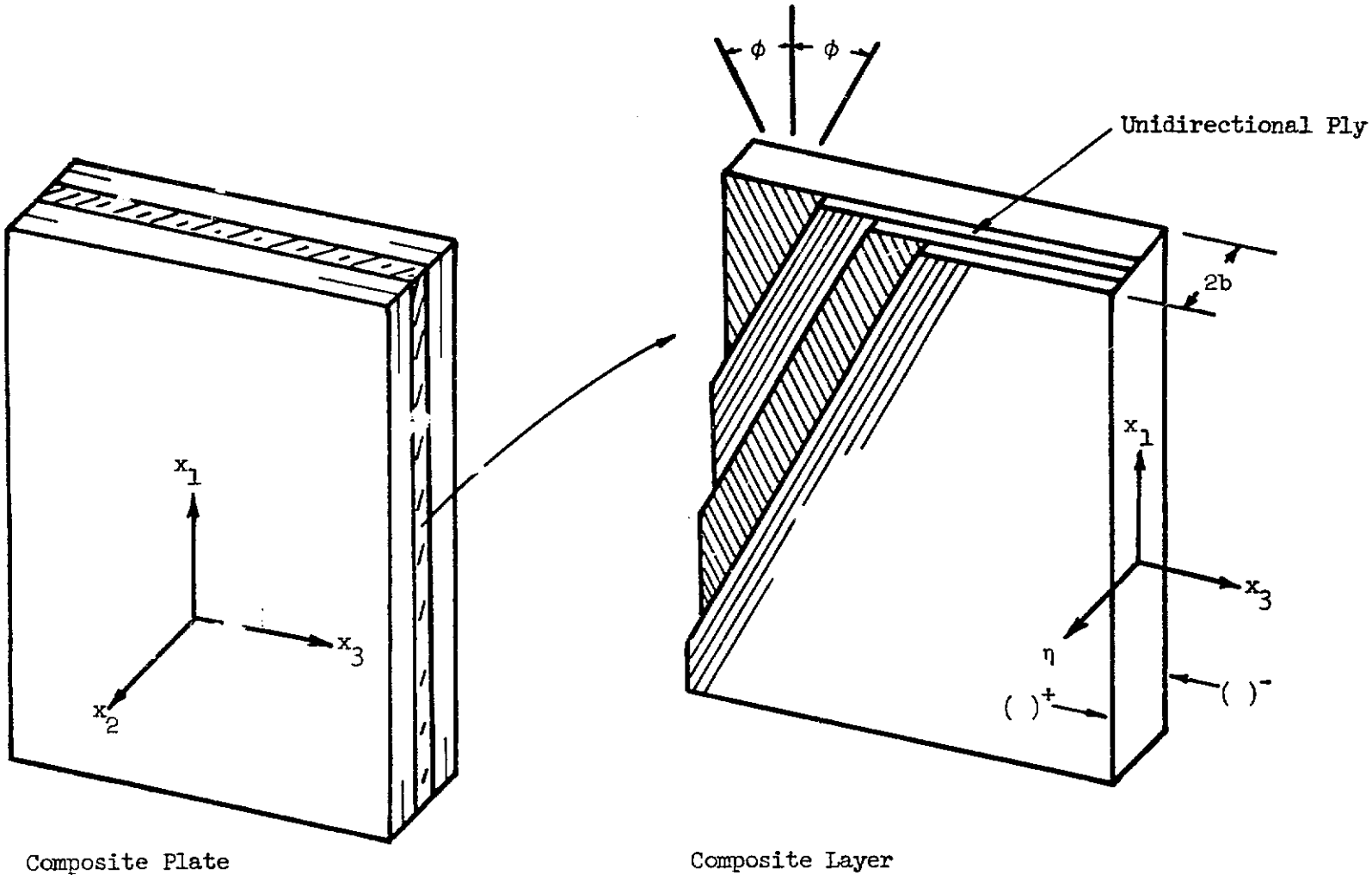

Figure 7. Multilayered Composite Plate

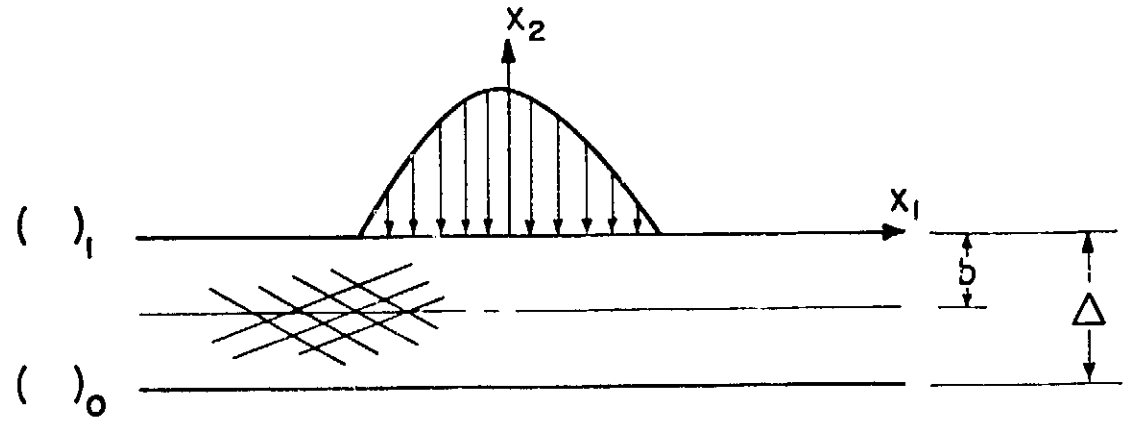

One-layer Model

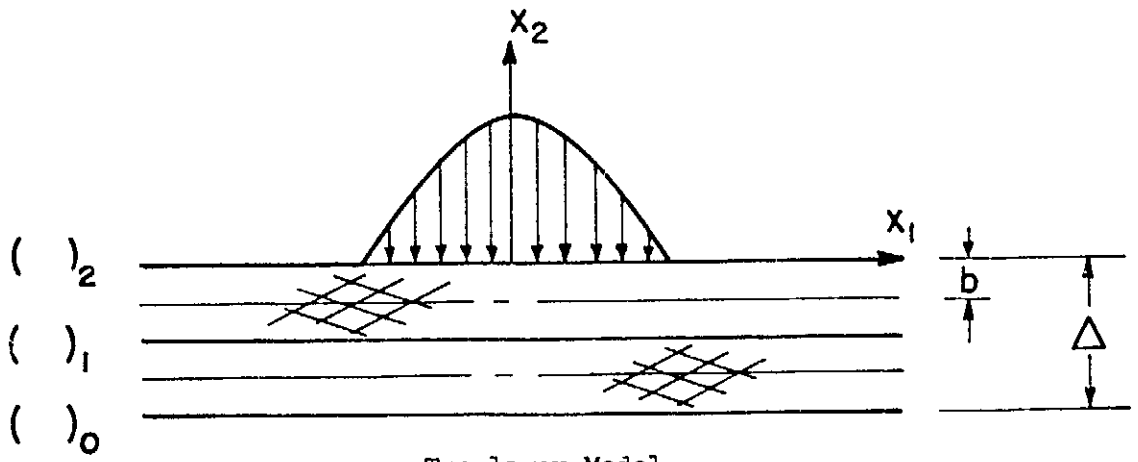

Two-layer Model

Figure 8. Composite Plate

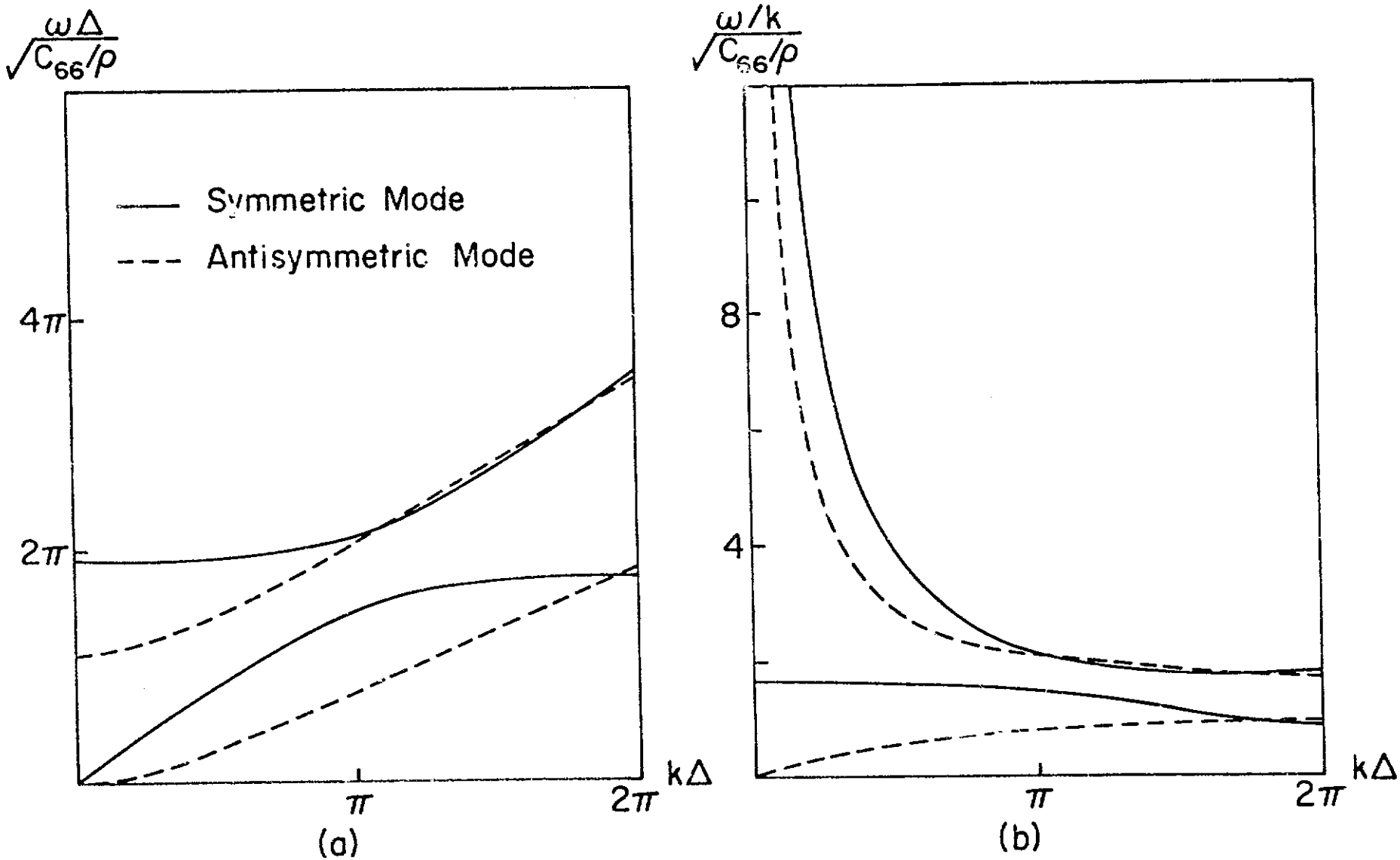

Figure 9. Dispersion Relationship and Phase Velocity of Isotropic One-Layer Plate ($\lambda = \mu$, Poisson's Ratio = 1/4)

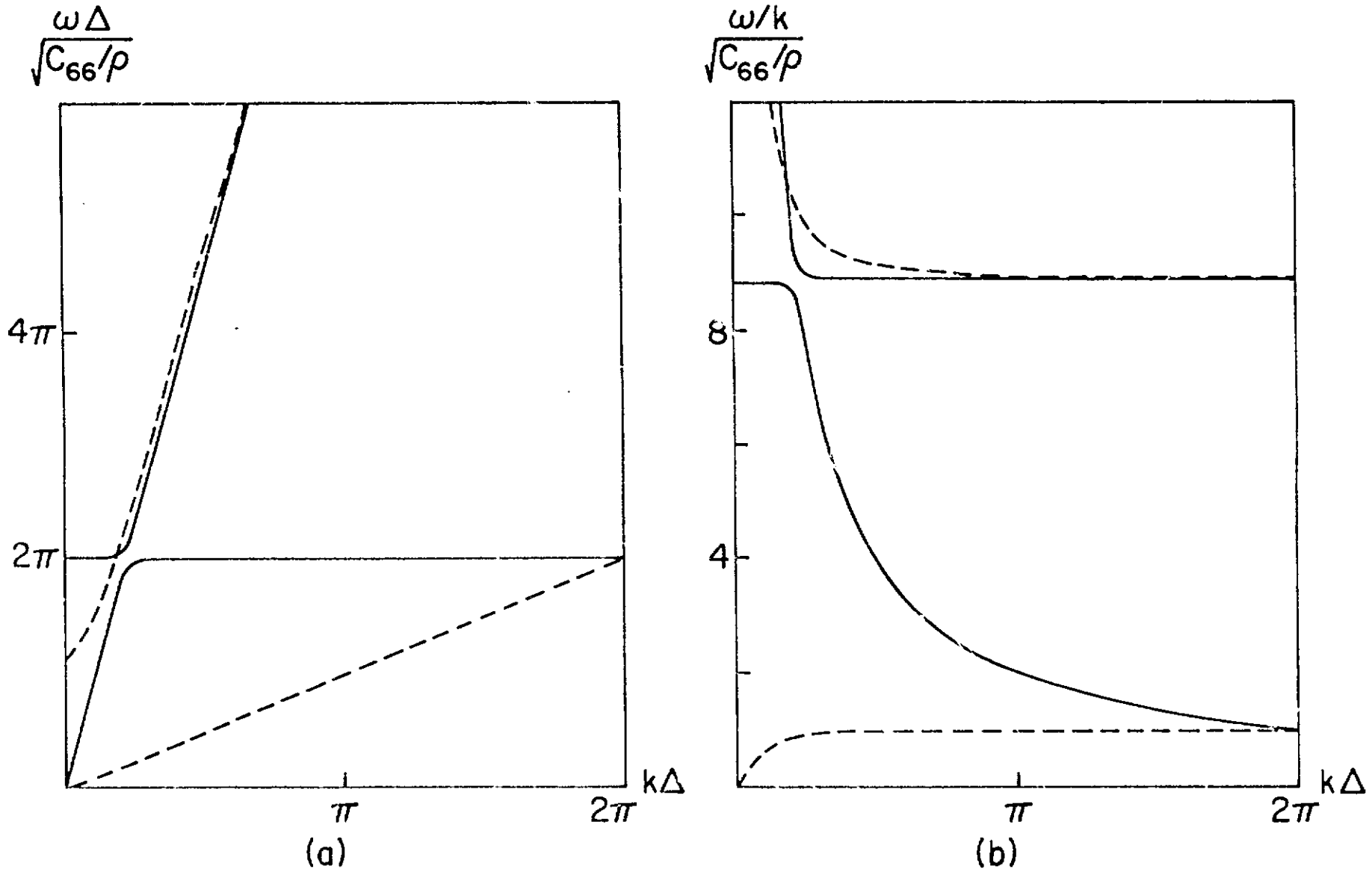

Figure 10. Dispersion Relationship and Phase Velocity of One-Layer Composite Plate (55% Graphite Fiber - Epoxy Matrix; Layup Angle = 0°)

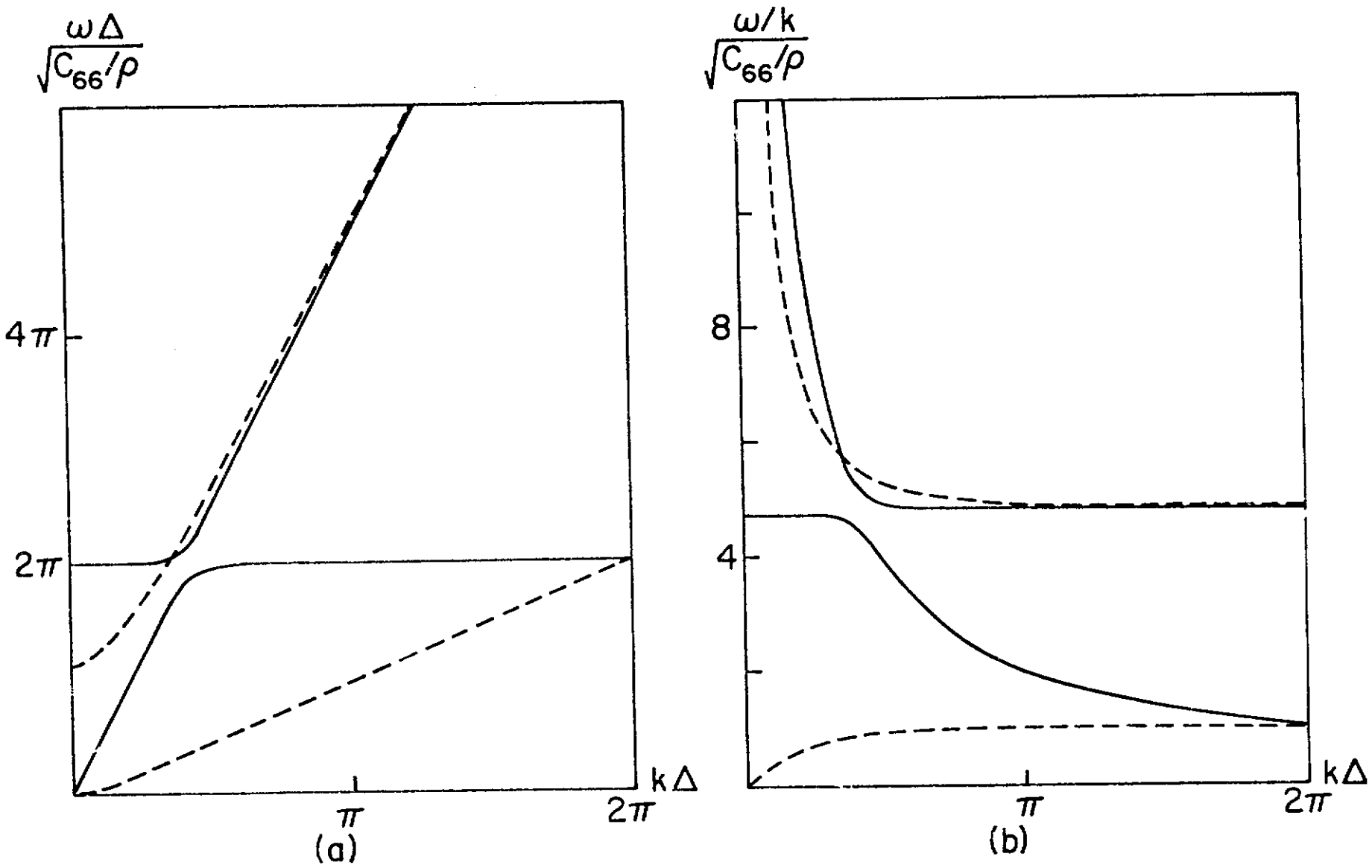

Figure 11. Dispersion Relationship and Phase Velocity of One-Layer Composite Plate (55% Graphite Fiber - Epoxy Matrix; Layup Angle = 45°)

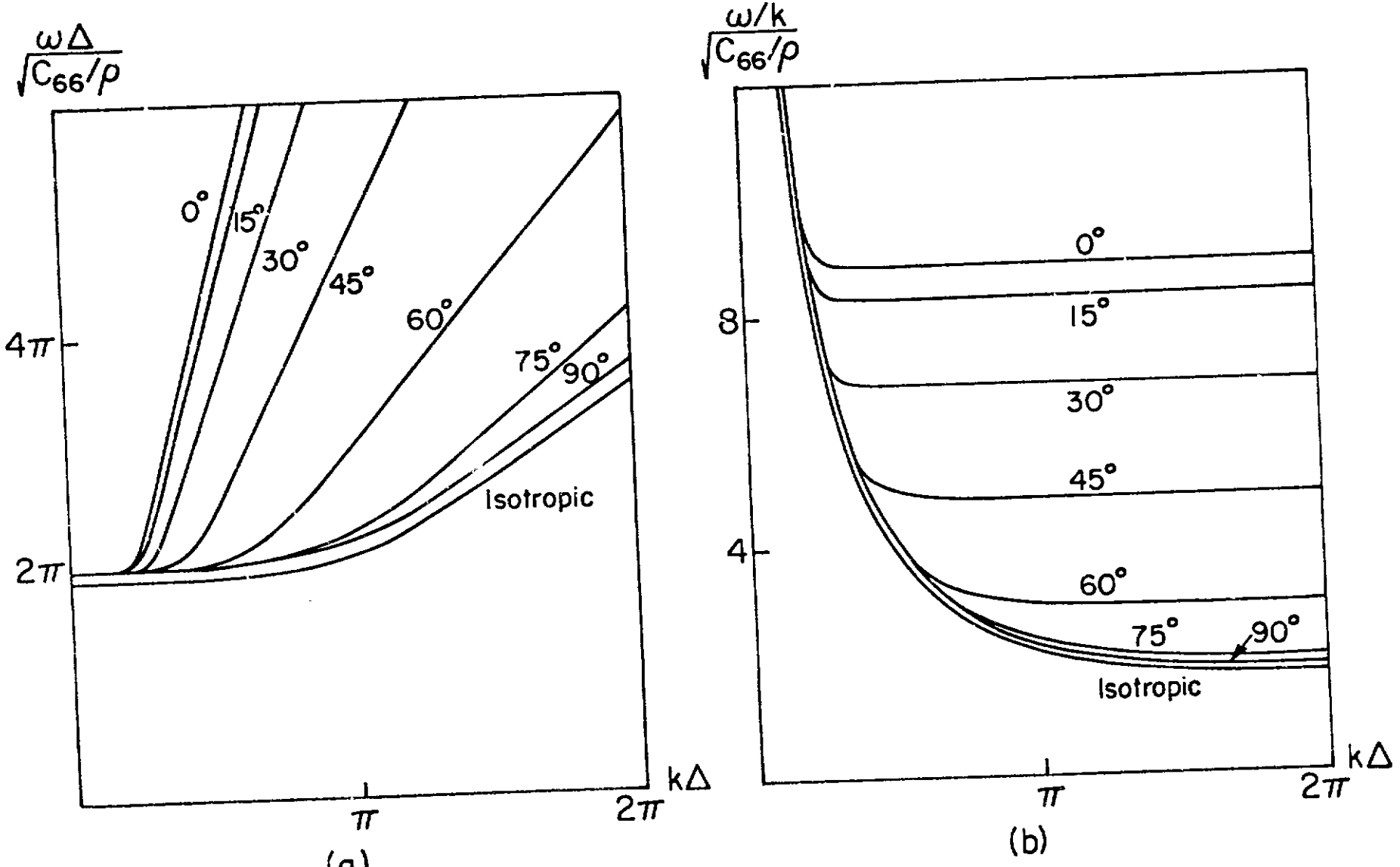

Figure 12. Effect of Layup Angle in Dispersion Relationship and Phase Velocity of Quasi-Longitudinal Wave (One Layer Model of Graphite - Epoxy Composite)

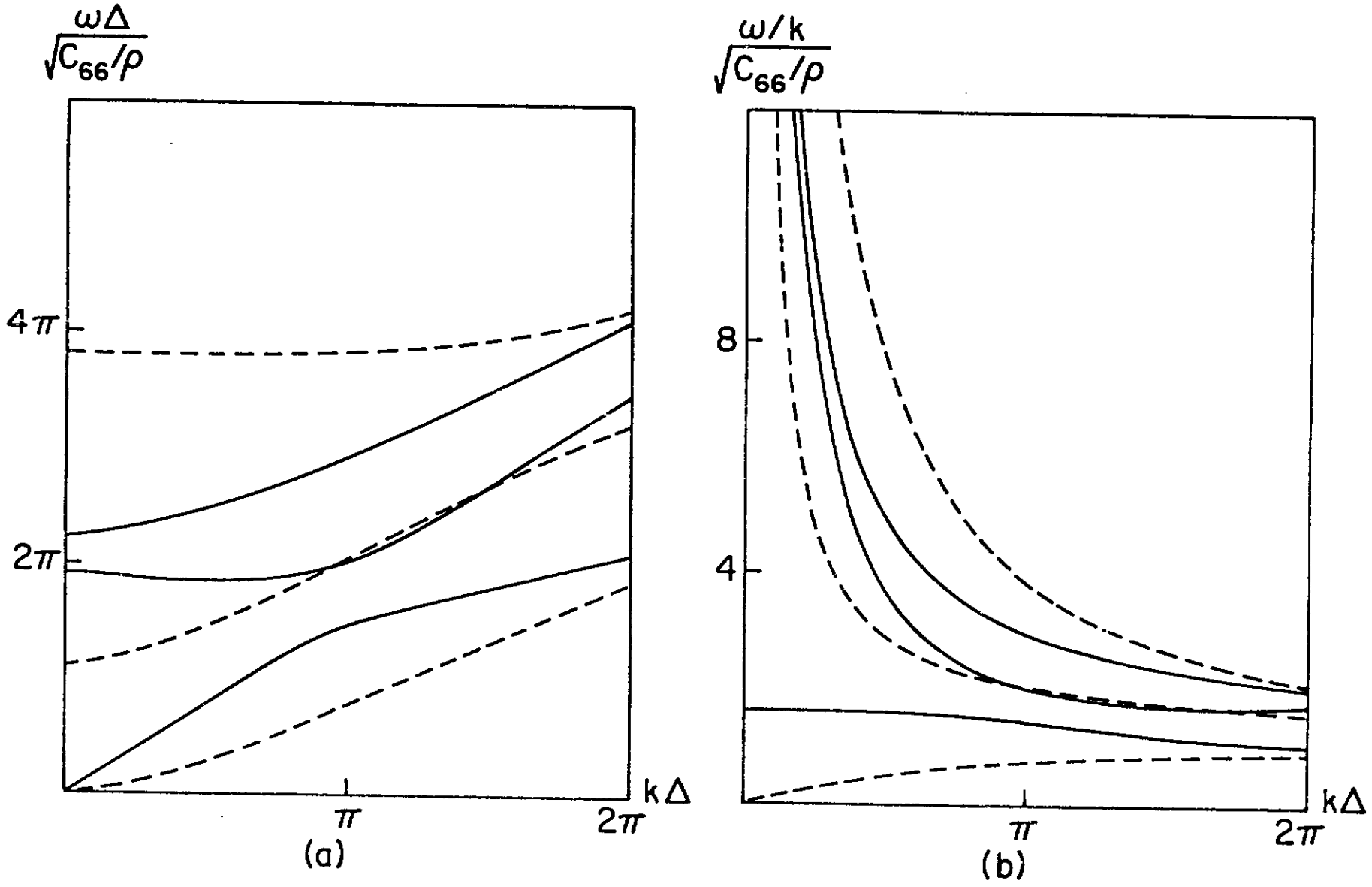

Figure 13. Dispersion Relationship and Phase Velocity of Isotropic Two-Layer Plate ($\lambda = \mu$, Poisson's Ratio = 1/4)

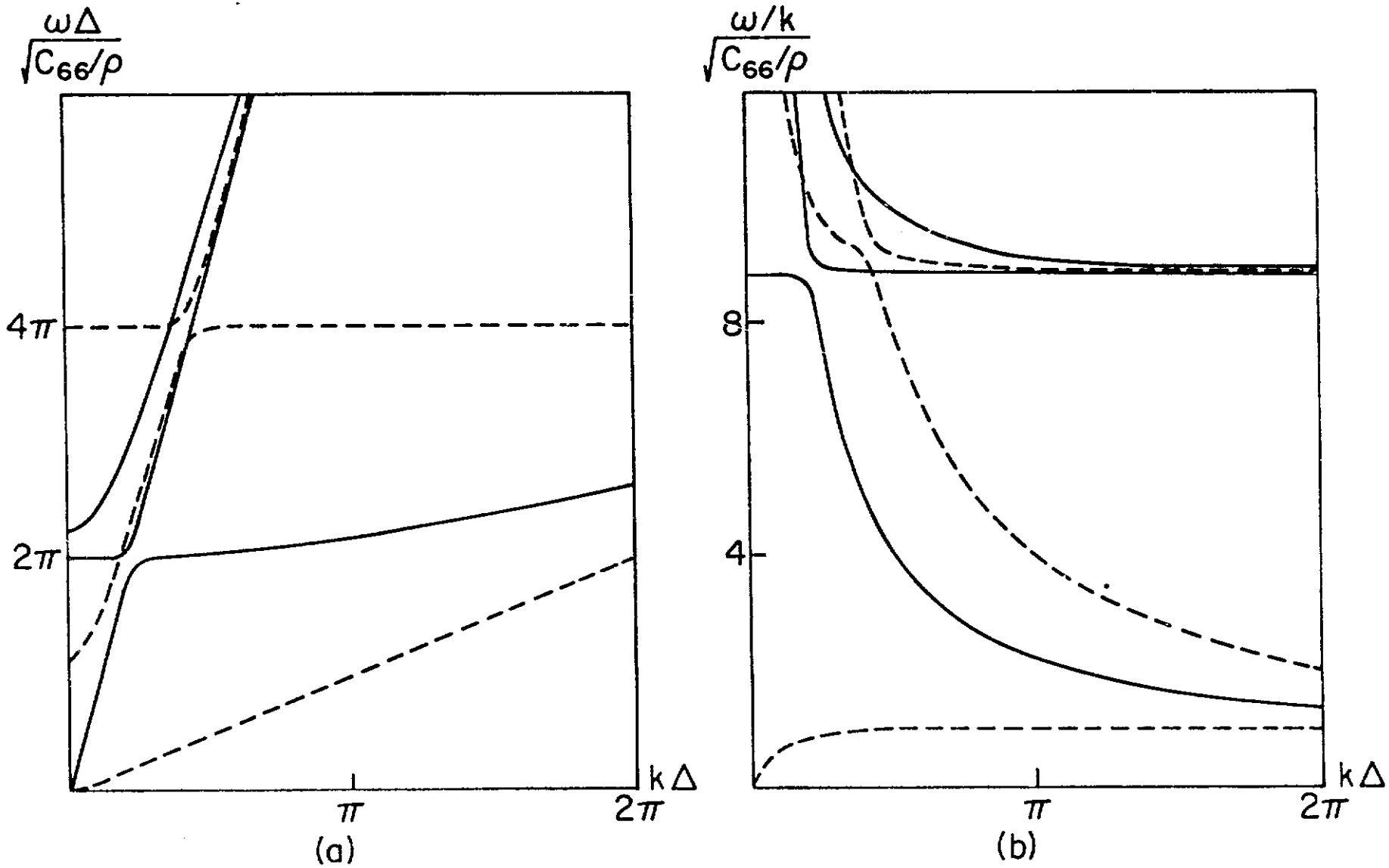

Figure 14. Dispersion Relationship and Phase Velocity of Two-Layer Composite Plate (55% Graphite Fiber - Epoxy Matrix, Layup Angle = 0°)

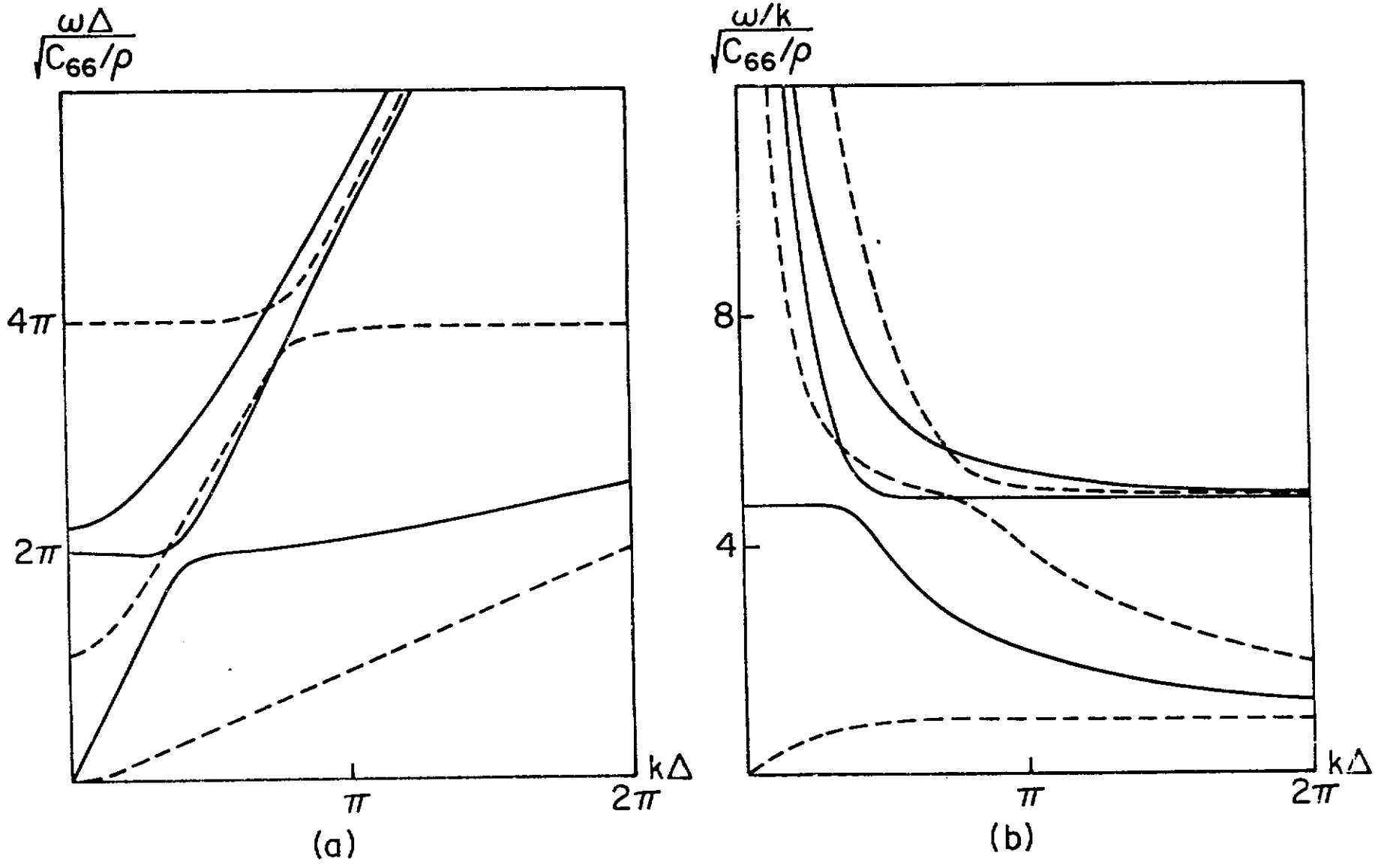

Figure 15. Dispersion Relationship and Phase Velocity of Two-Layer Composite Plate (55% Graphite Fiber - Epoxy Matrix, Layup Angle = 45°)

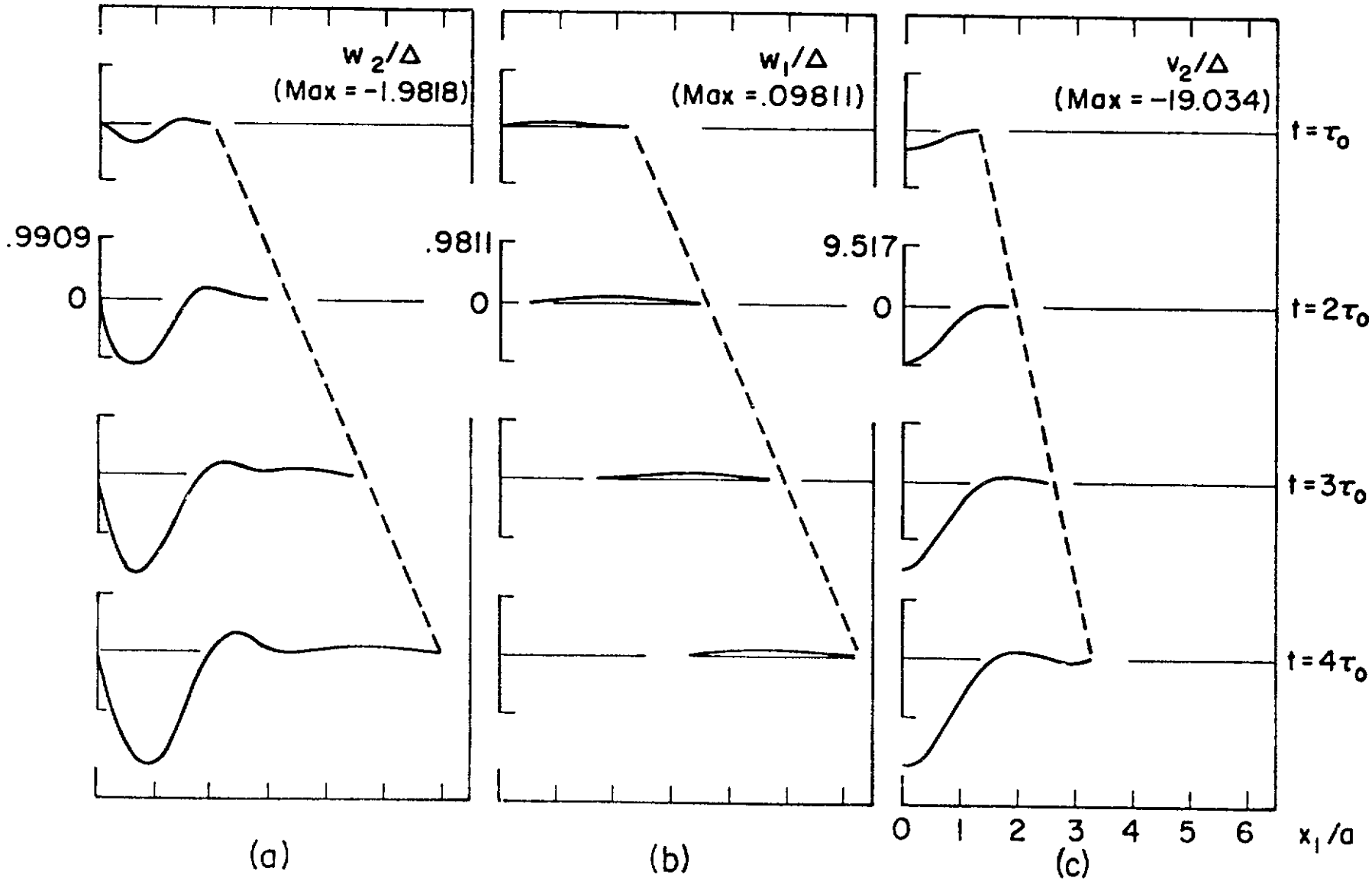

Figure 16. Wave Propagation in Isotropic Two-Layer Plate

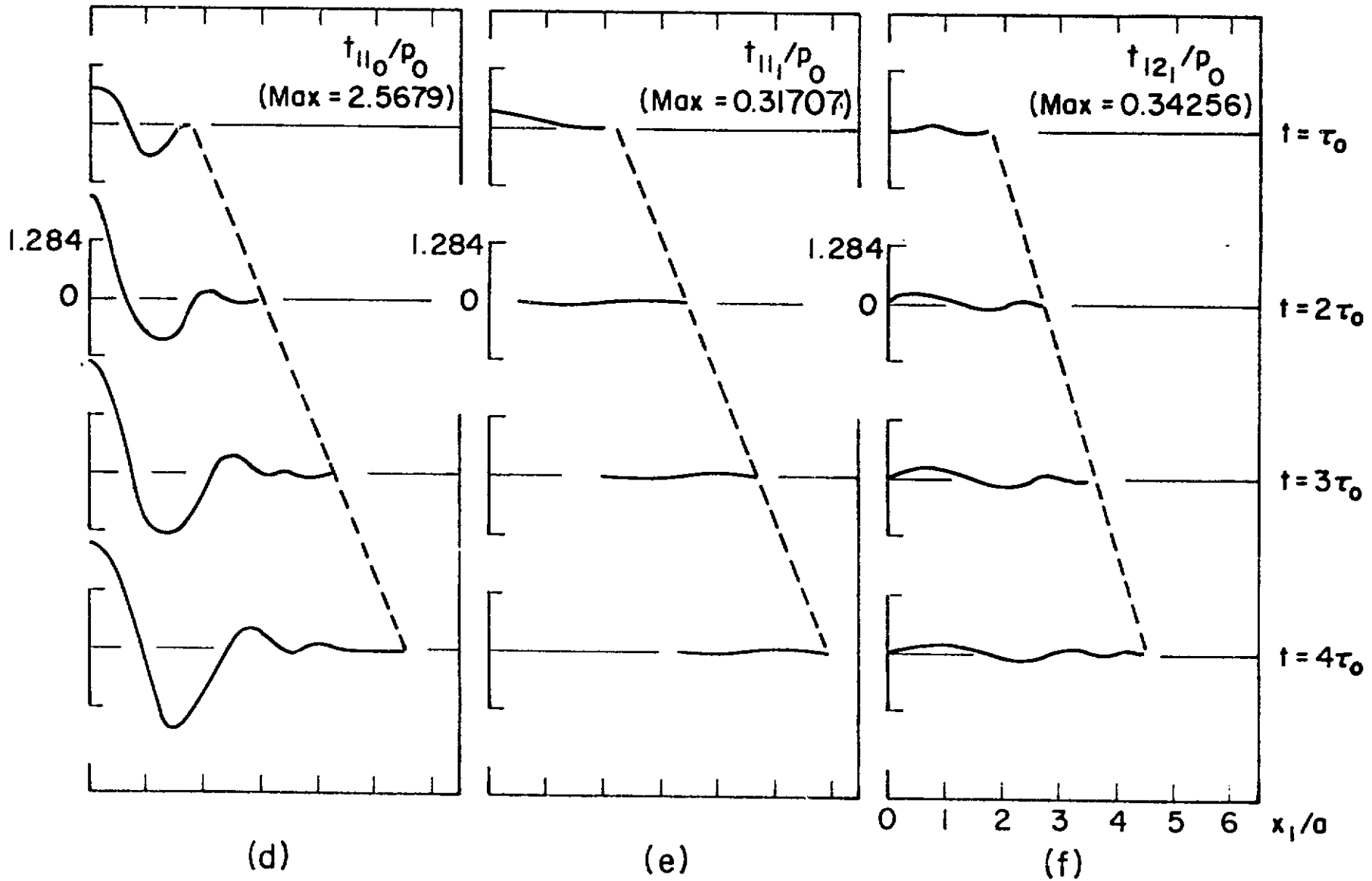

Figure 16 d,e,f

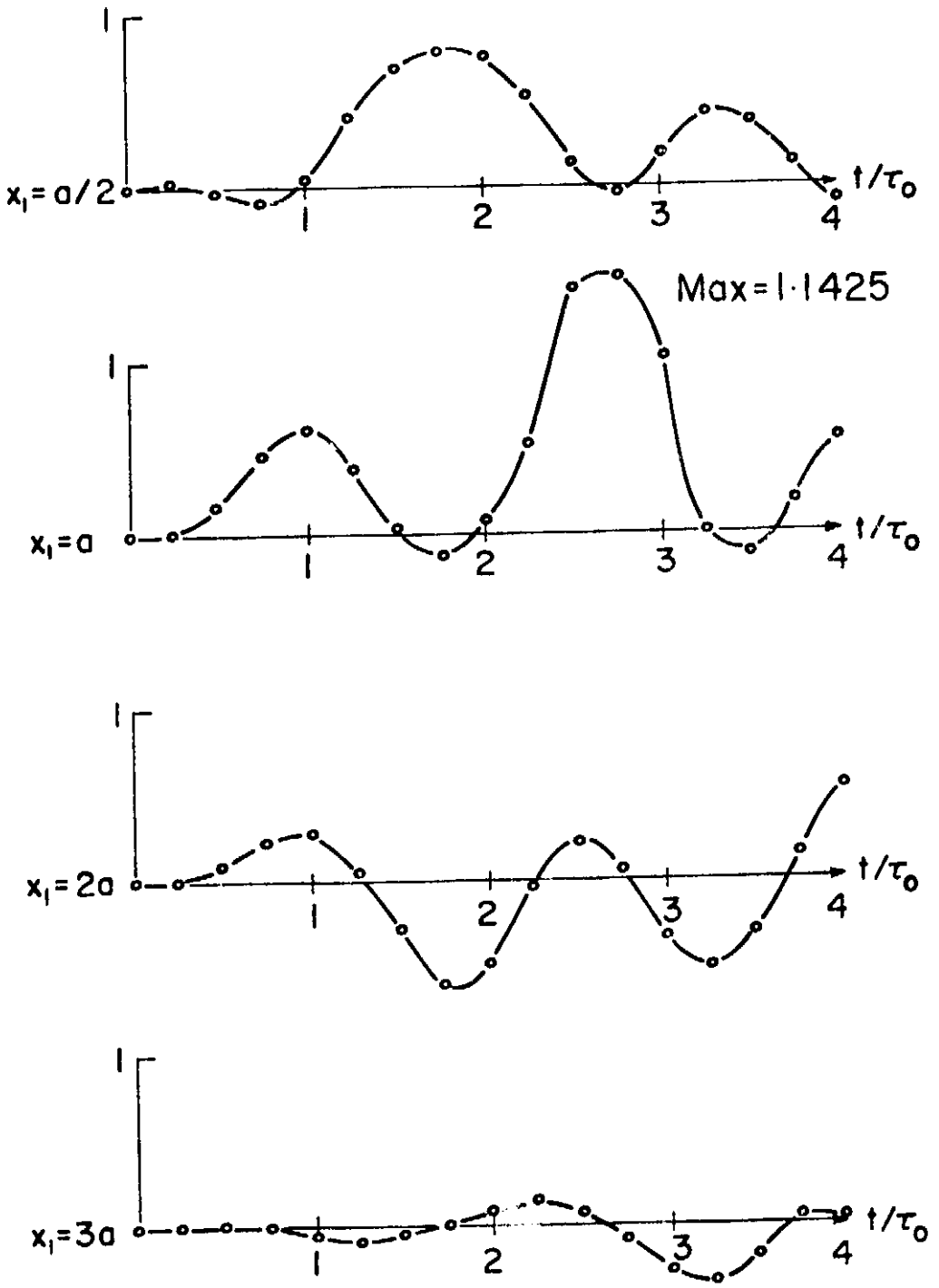

17 - (a)

Figure 17. Interlaminar Shear Stress t_{12_1}/P_o in Two Layer Composite Plate

Plate Thickness; Δ = 1 cm
Contact Time; τ_o = 20 μsec
Contact Radius; a = 4 cm
55% Graphite Fiber - Epoxy Matrix, Layup Angle = 45°

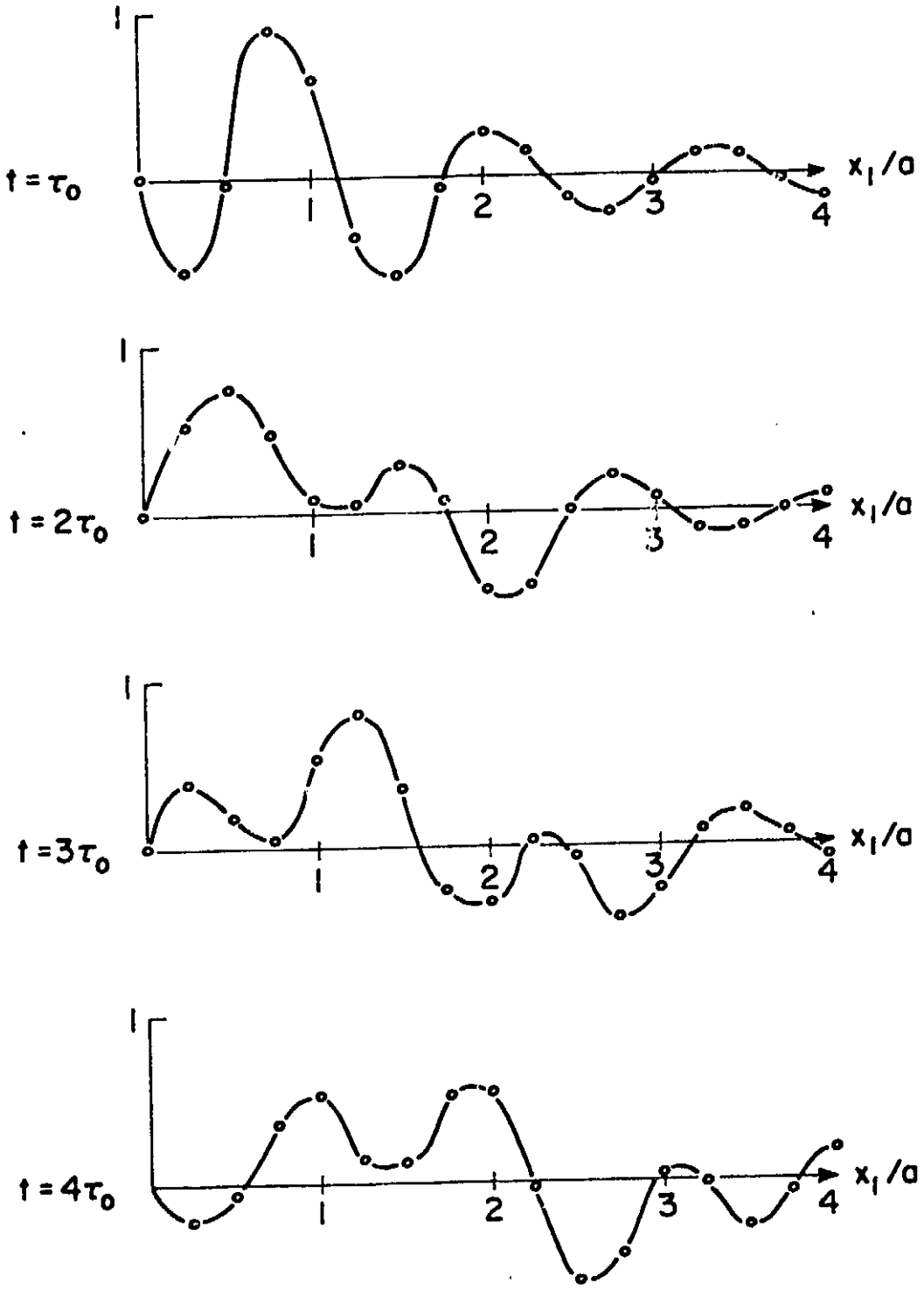
I
$t = \tau_0$
1
2
3
4
x_1/a
I
$t = 2\tau_0$
1
2
3
4
x_1/a
I
$t = 3\tau_0$
1
2
3
4
x_1/a
I
$t = 4\tau_0$
1
2
3
4
x_1/a

17 - (b)

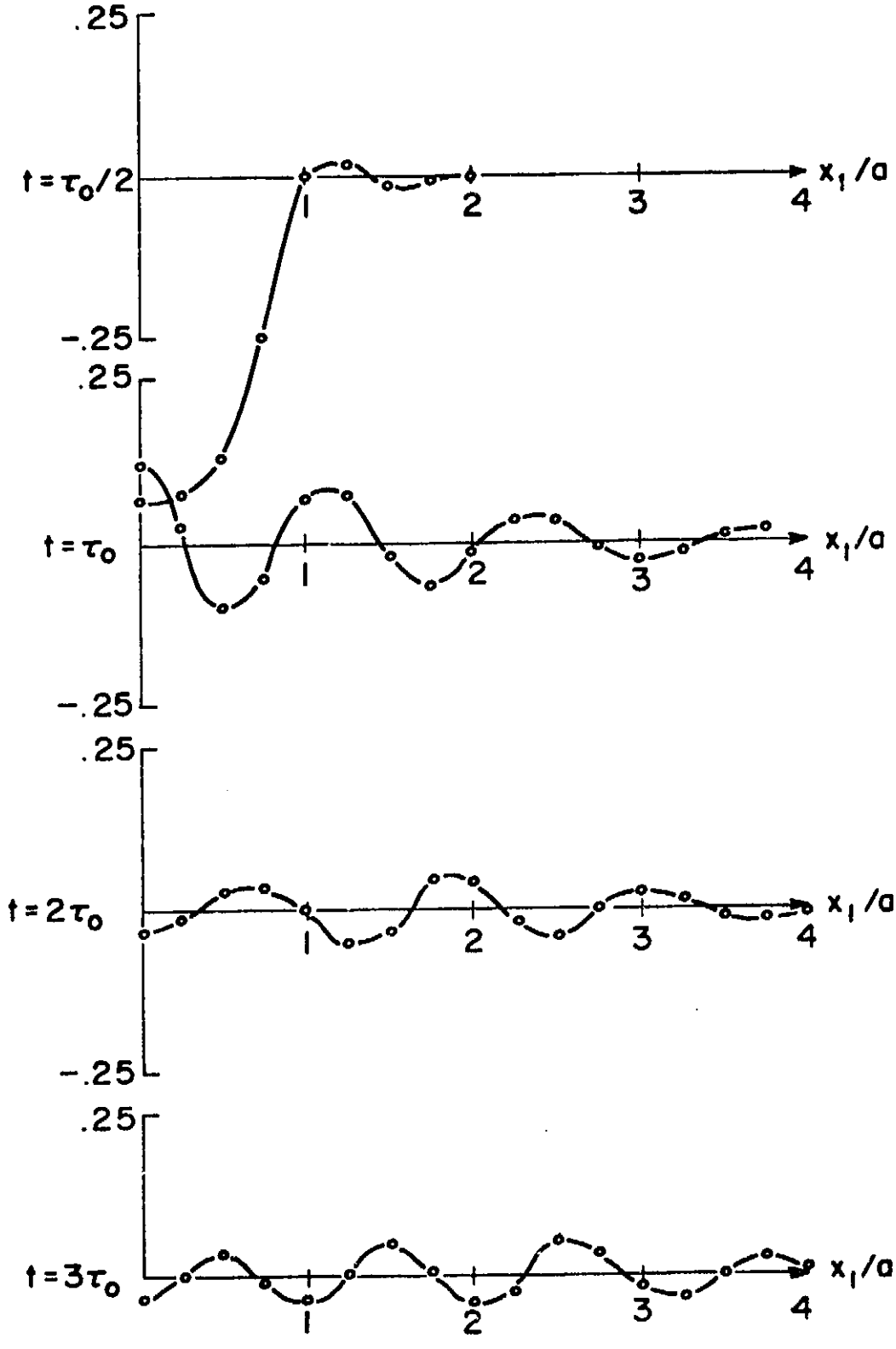

18 - (a)

Figure 18. Interlaminar Normal Stress t_{2_1}/P_o in Two Layer Composite Plate

Plate Thickness; Δ = 1 cm
Contact Time; τ_o = 20 usec
Contact Radius; a = 4 cm
55% Graphite Fiber - Epoxy Matrix, Layup Angle = 45°

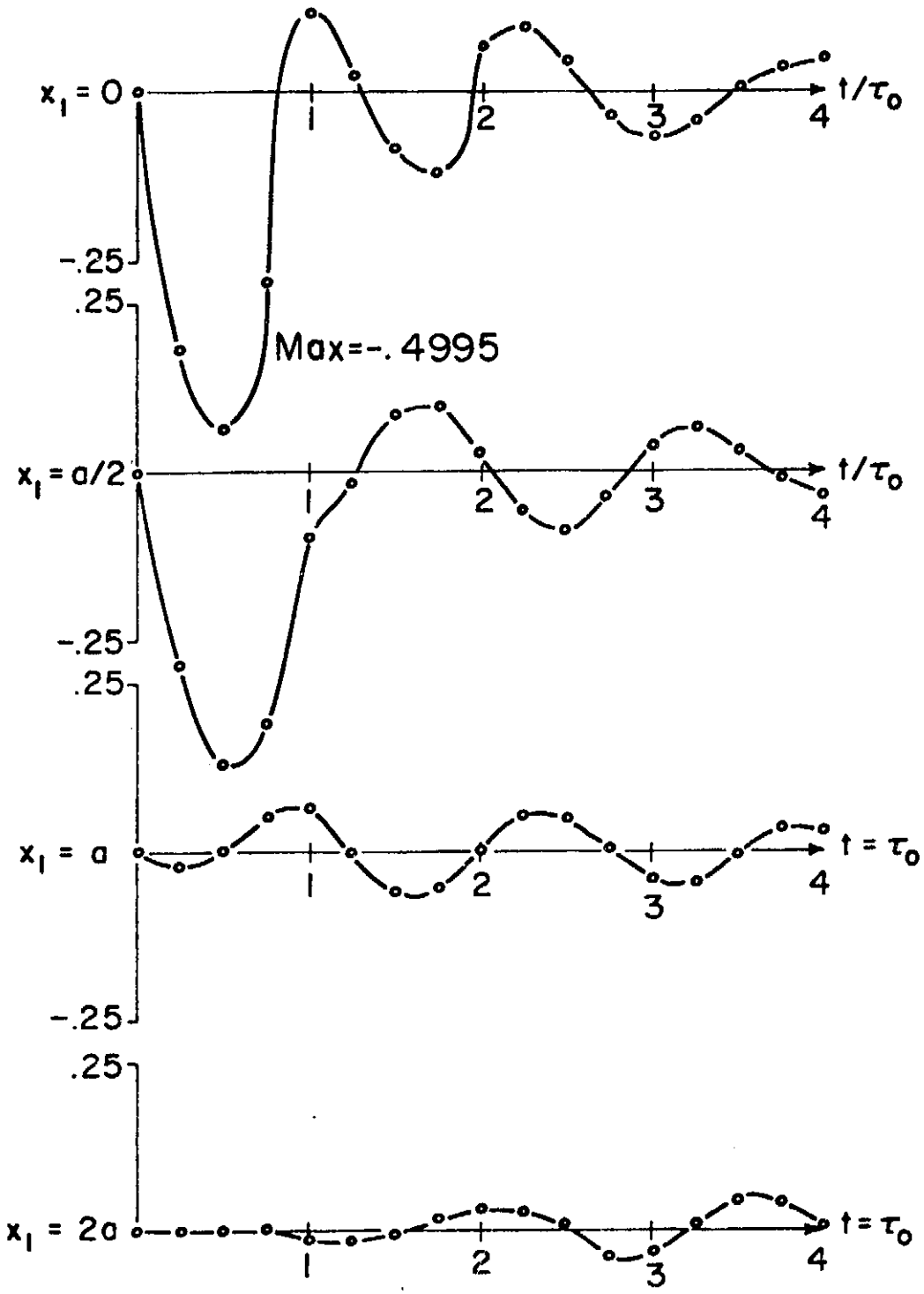

18 - (b)

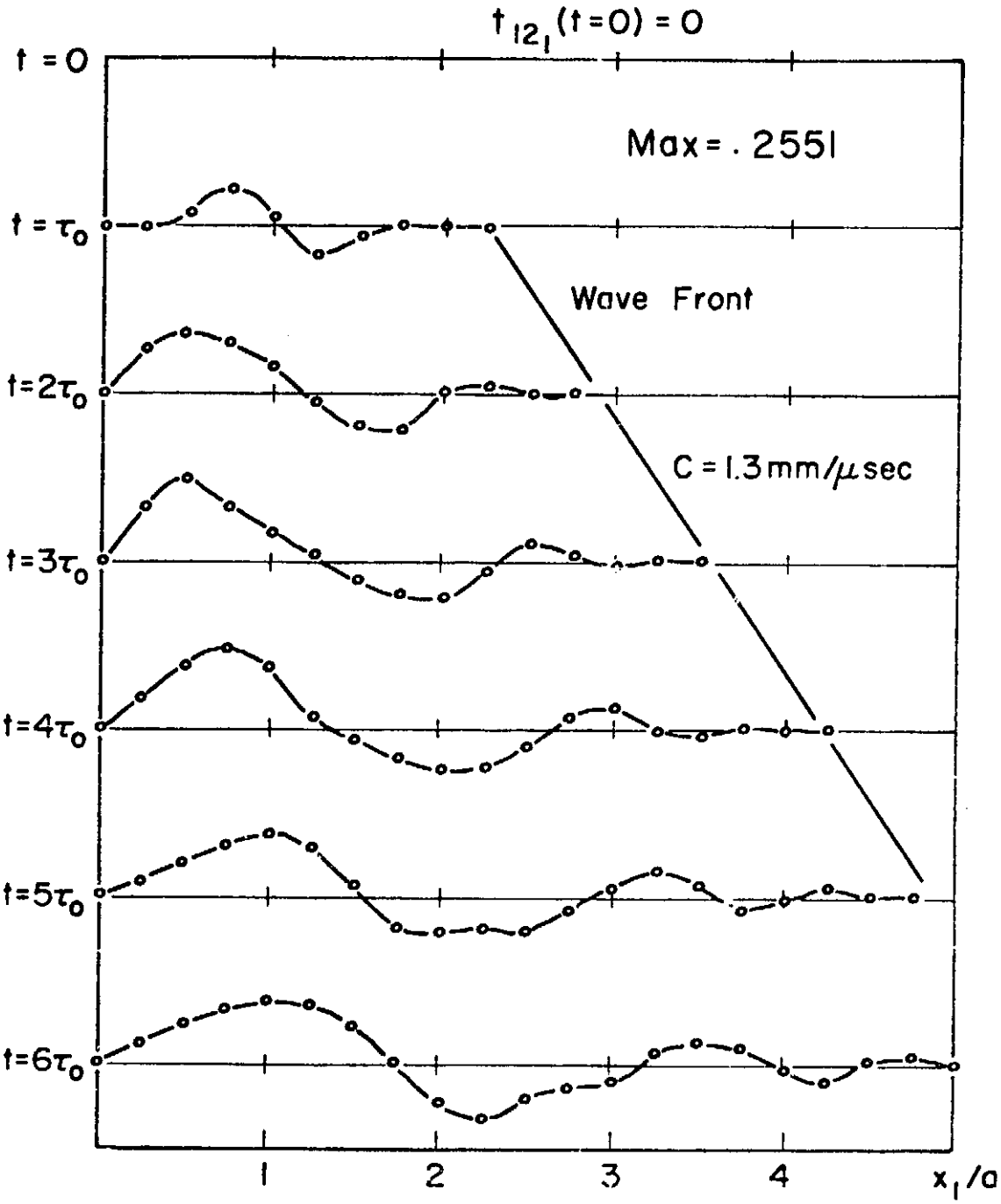

Figure 19. Interlaminar Shear Stress (t_{12_1}/P_o)
Two-Layer Composite Plate
55% Graphite Fiber - Epoxy Matrix
Layup Angle = 90°
Δ = 1 cm, a = 4 cm, τ_o = 20 μsec

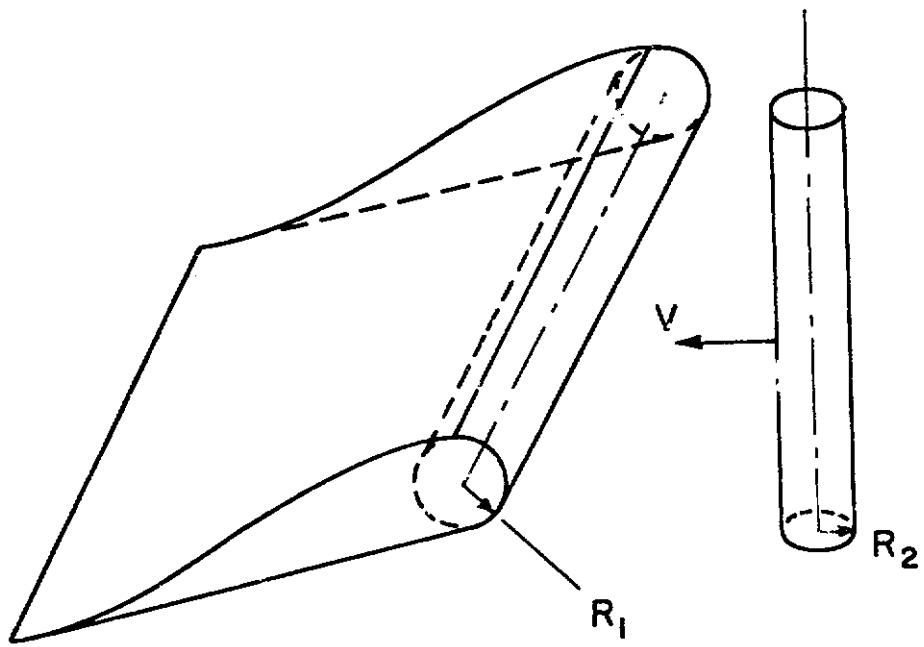

Figure 20. Model for the Impact of a Bone Cylinder with an Aircraft Wing or a Turbine Blade

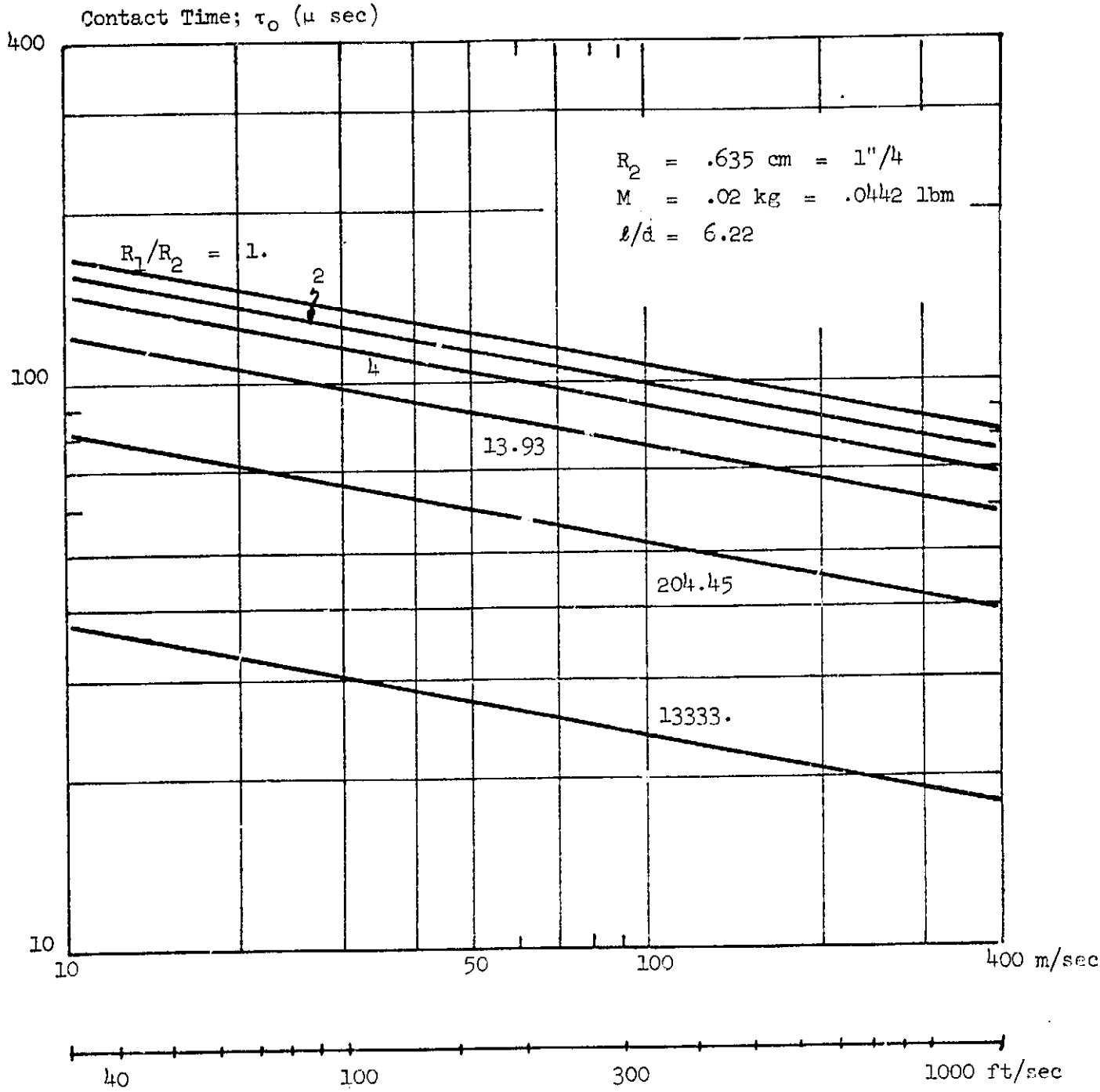

Figure 21a. Impact of Bird Bone and Graphite-Epoxy Composite; Contact Time Vs Impact Velocity

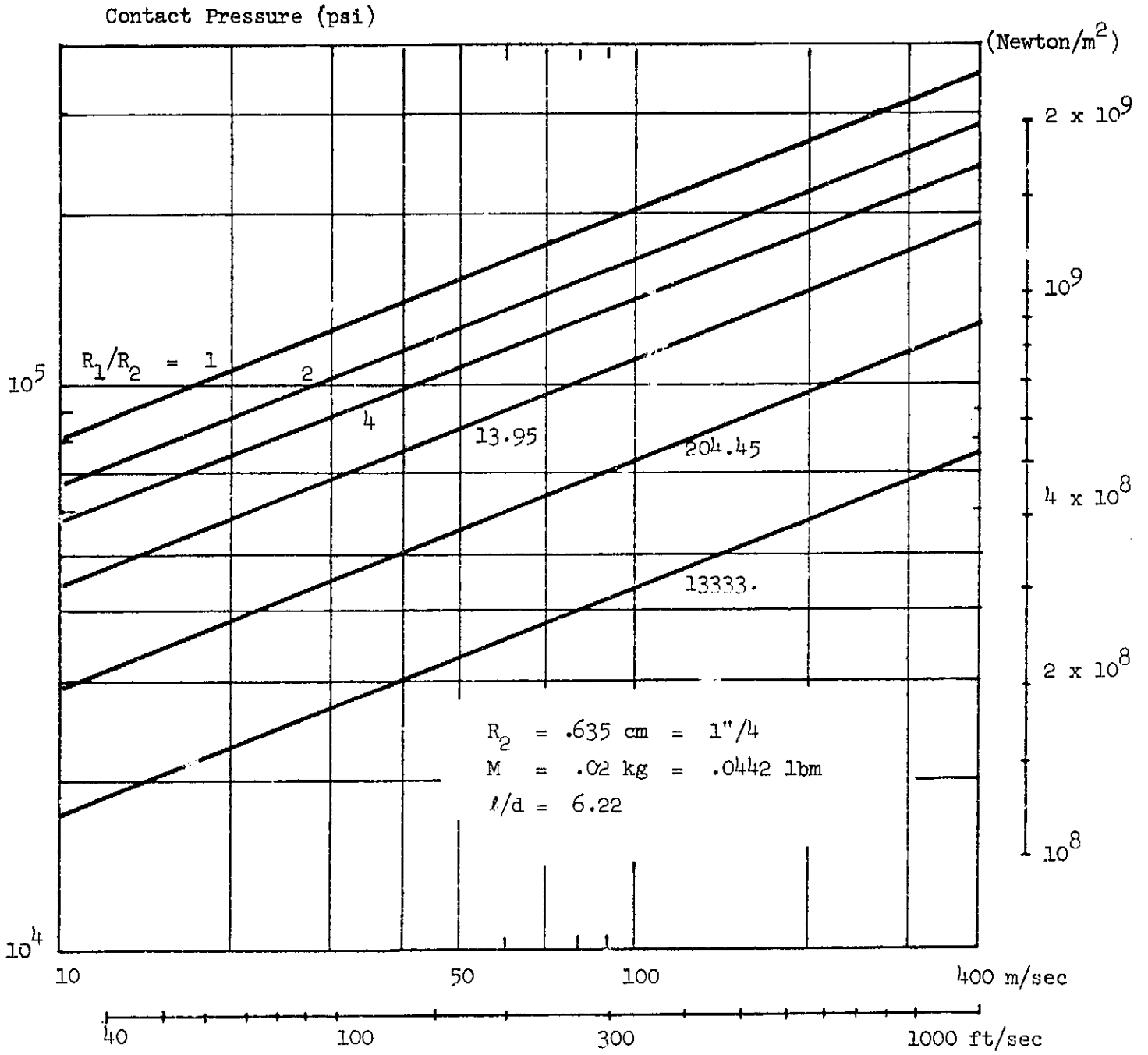

Figure 21b. Impact of Bird Bone and Graphite/Epoxy Composite: Contact Stress Vs Impact Velocity

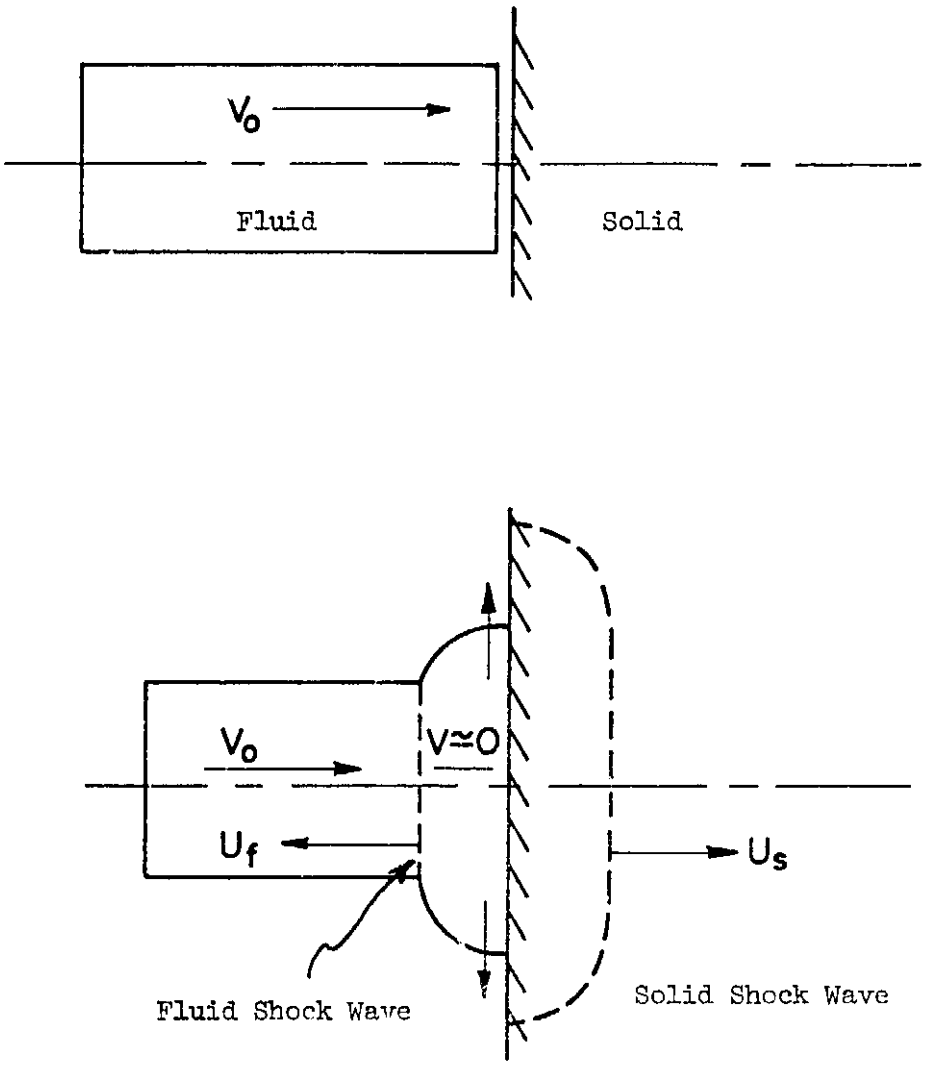

Figure 22. Water Hammer Model for Fluid - Solid Impact

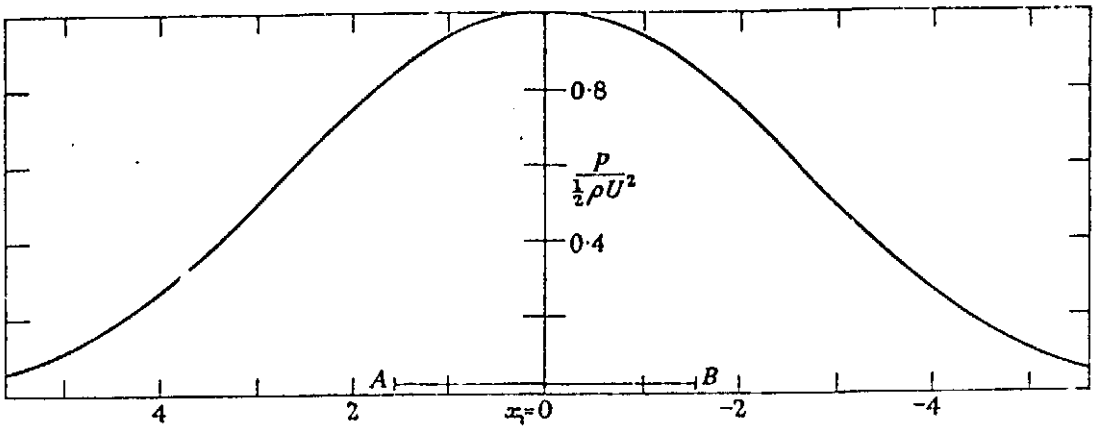

a. Pressure on plate, $\theta = 90°$. AB is jet width.

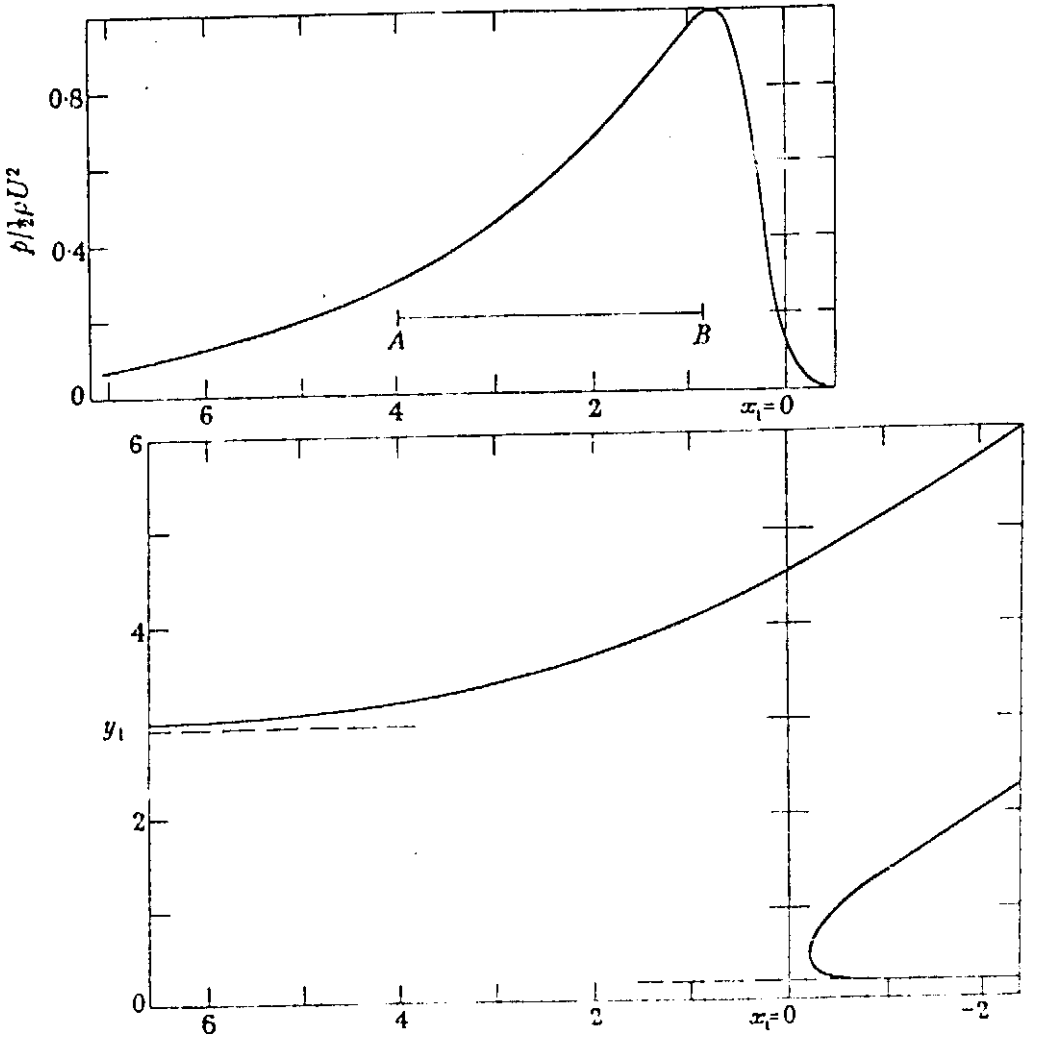

b. The upper half: pressure on plate $\theta = 30°$, AB is jet width.
The lower half: shape of jet when $\theta = 30°$.

Figure 23. Distribution of Pressure in Steady Flow of Two Dimensional Jet Against Flat Plate [36]

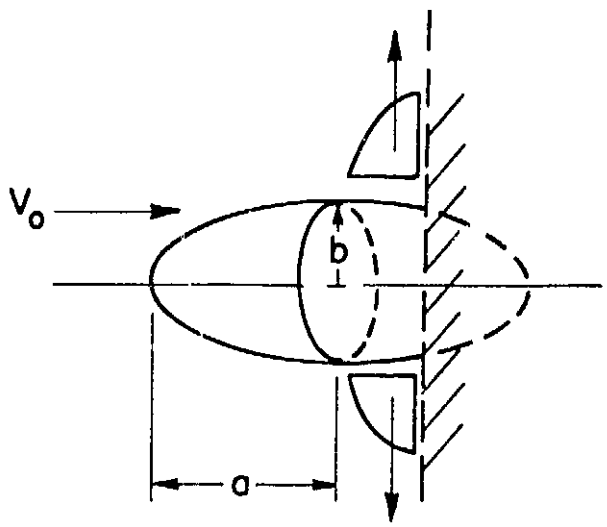

Figure 24. Momentum Model for Impact Force due to Fluid Impact with a Flat Plate

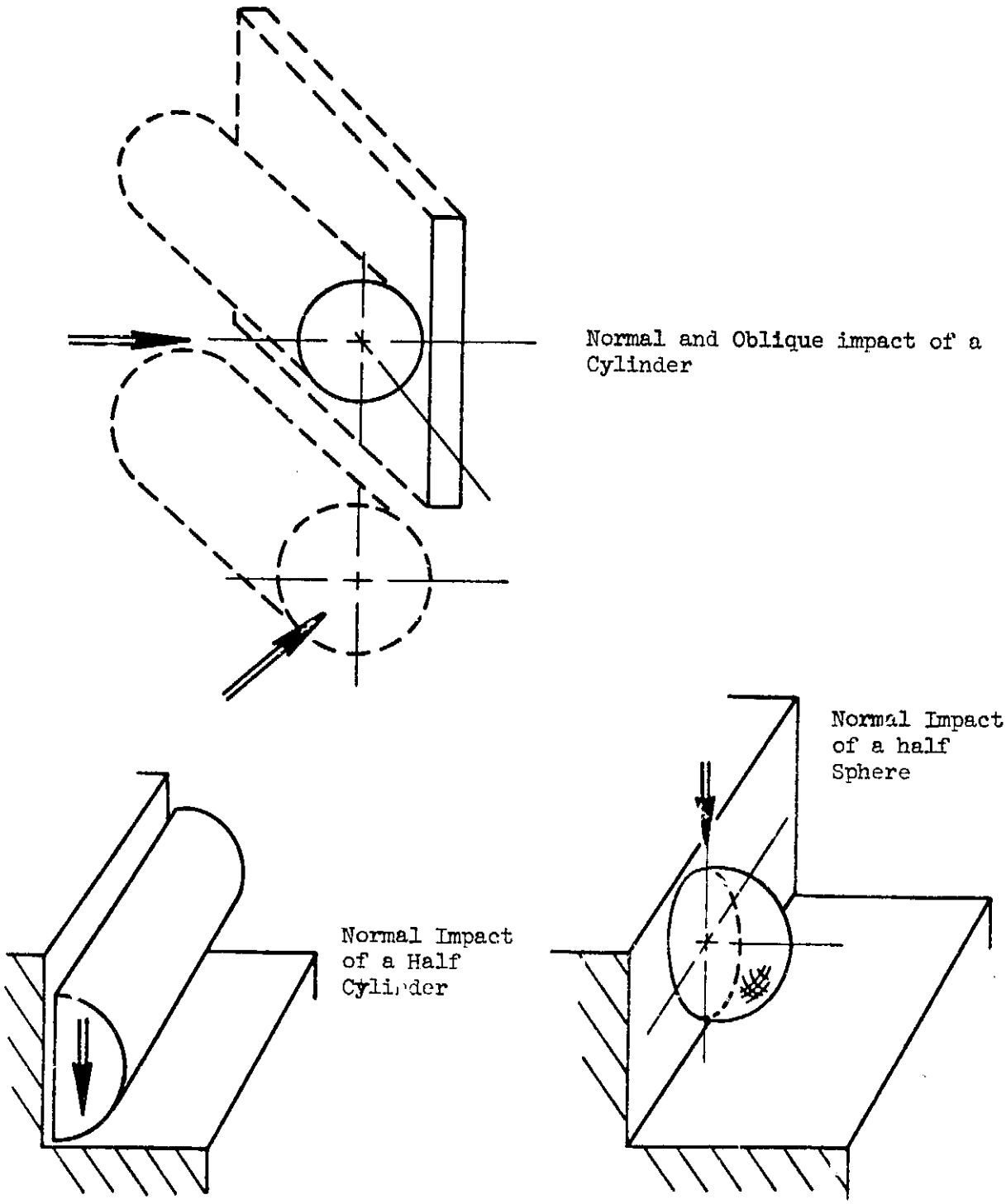

Figure 25. Finite Difference Models for Hydrodynamic Fluid Impact Code

0.0 SEC

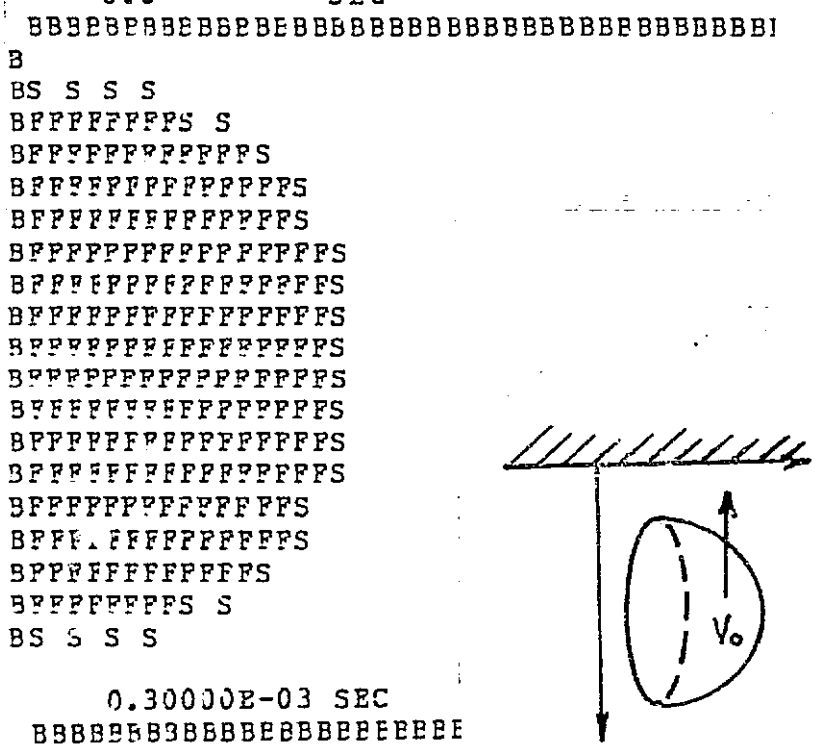

0.30000E-03 SEC

0.15000E-03 SEC

0.44999E-03 SEC

Figure 26a

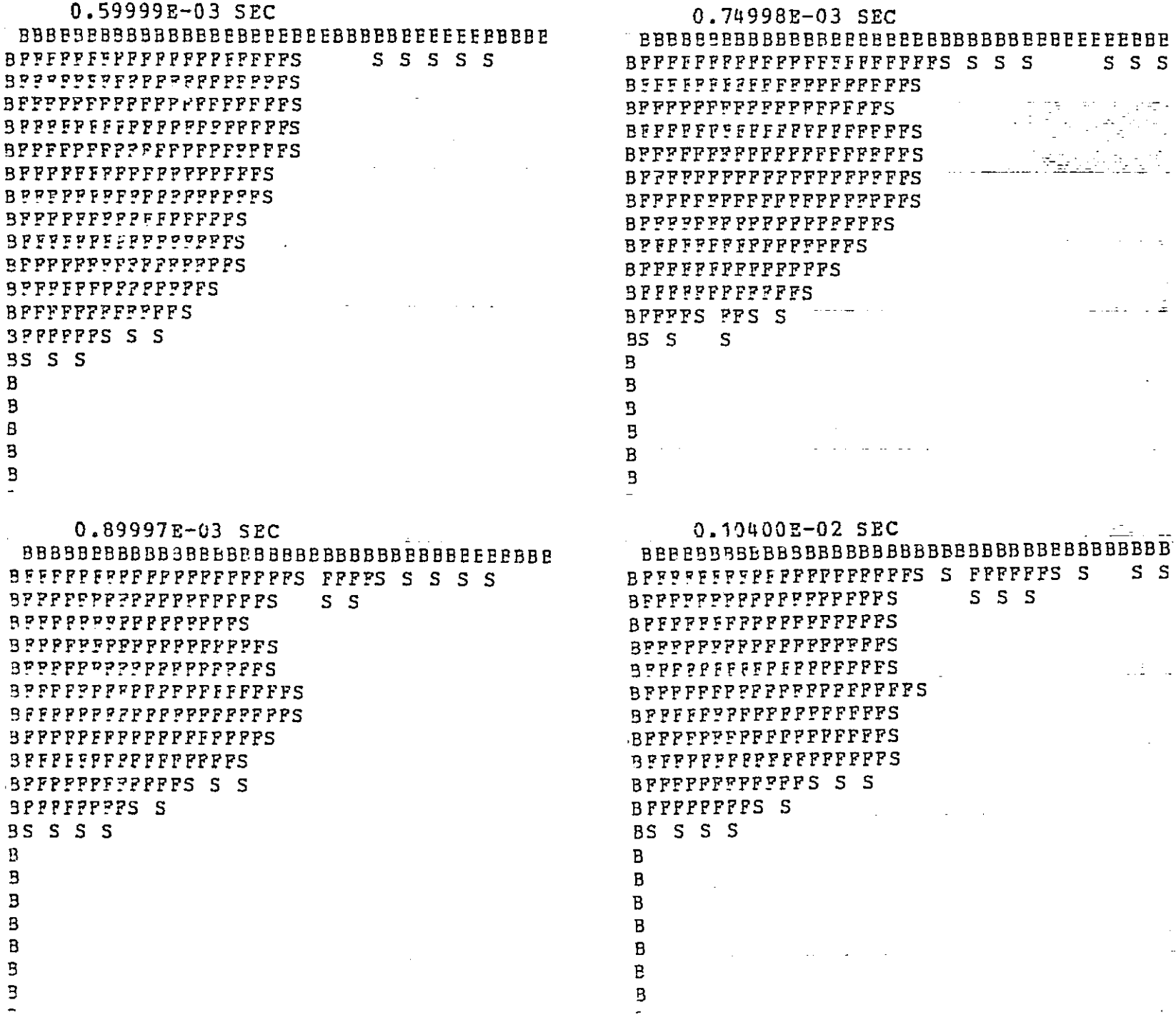

Figure 26b

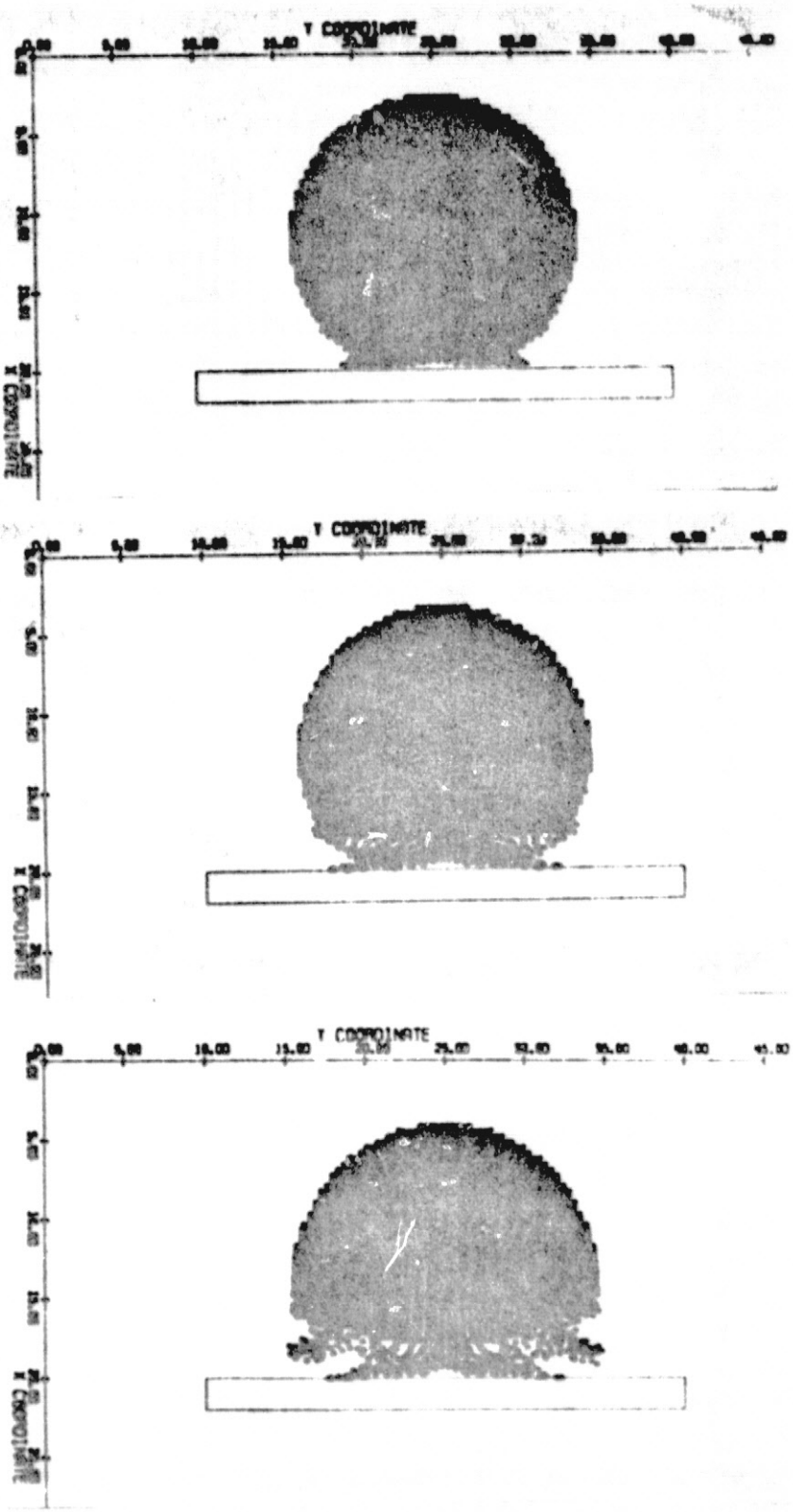

$t = 1.6 \times 10^{-4}$ sec

$t = 2.4 \times 10^{-4}$ sec

$t = 3.2 \times 10^{-4}$ sec

Figure 27. Normal Impact of a Fluid Cylinder

Diameter=1.8 cm, Kinematic Viscosity=.1 poise
Impact Veolcity=1000 cm/sec.

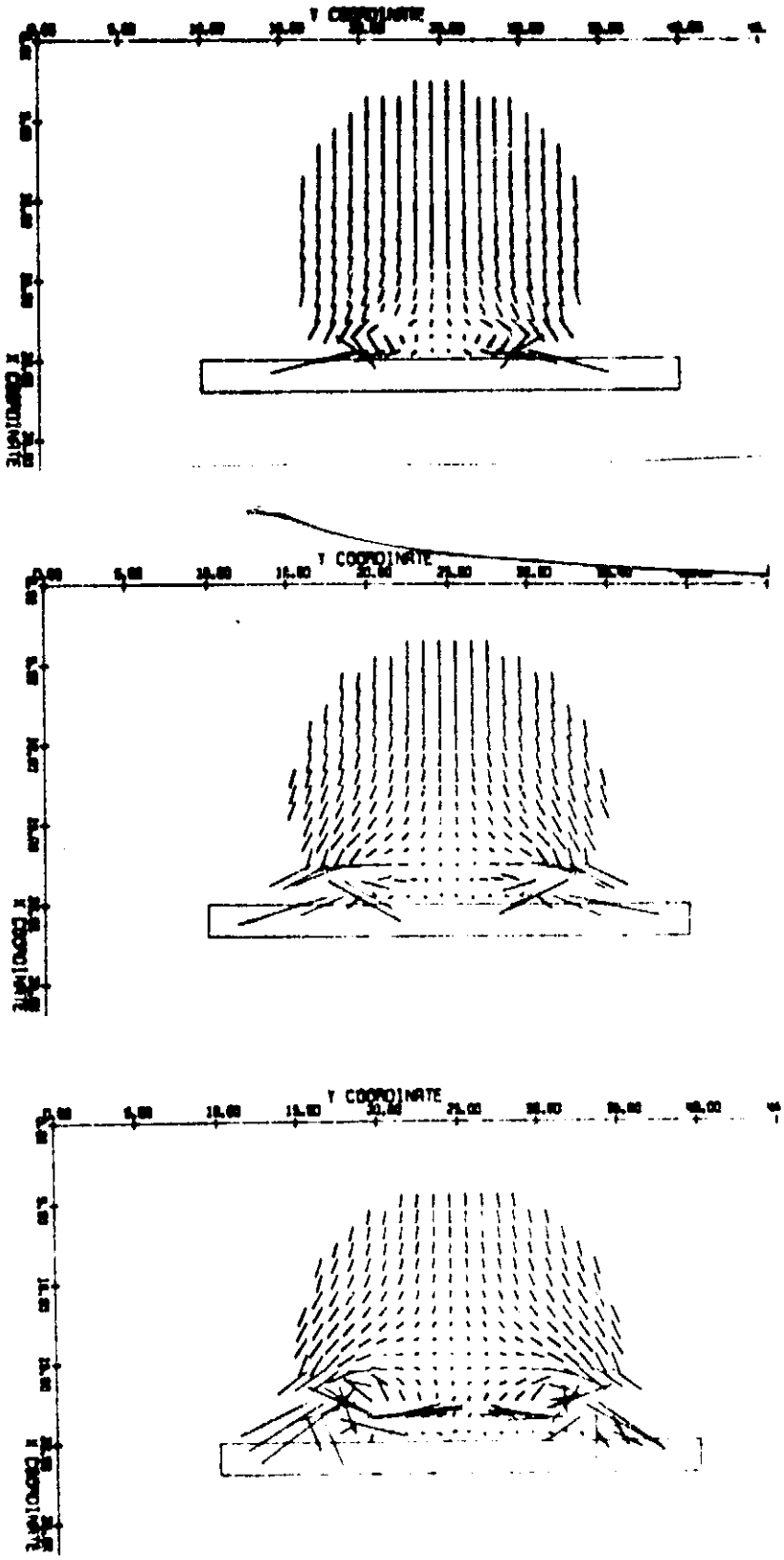

Figure 28. Velocity Vectors for Normal Impact of a Fluid Cylinder(conditions same as Fig. 27)

MAT OF FULL AND EMPTY CELLS

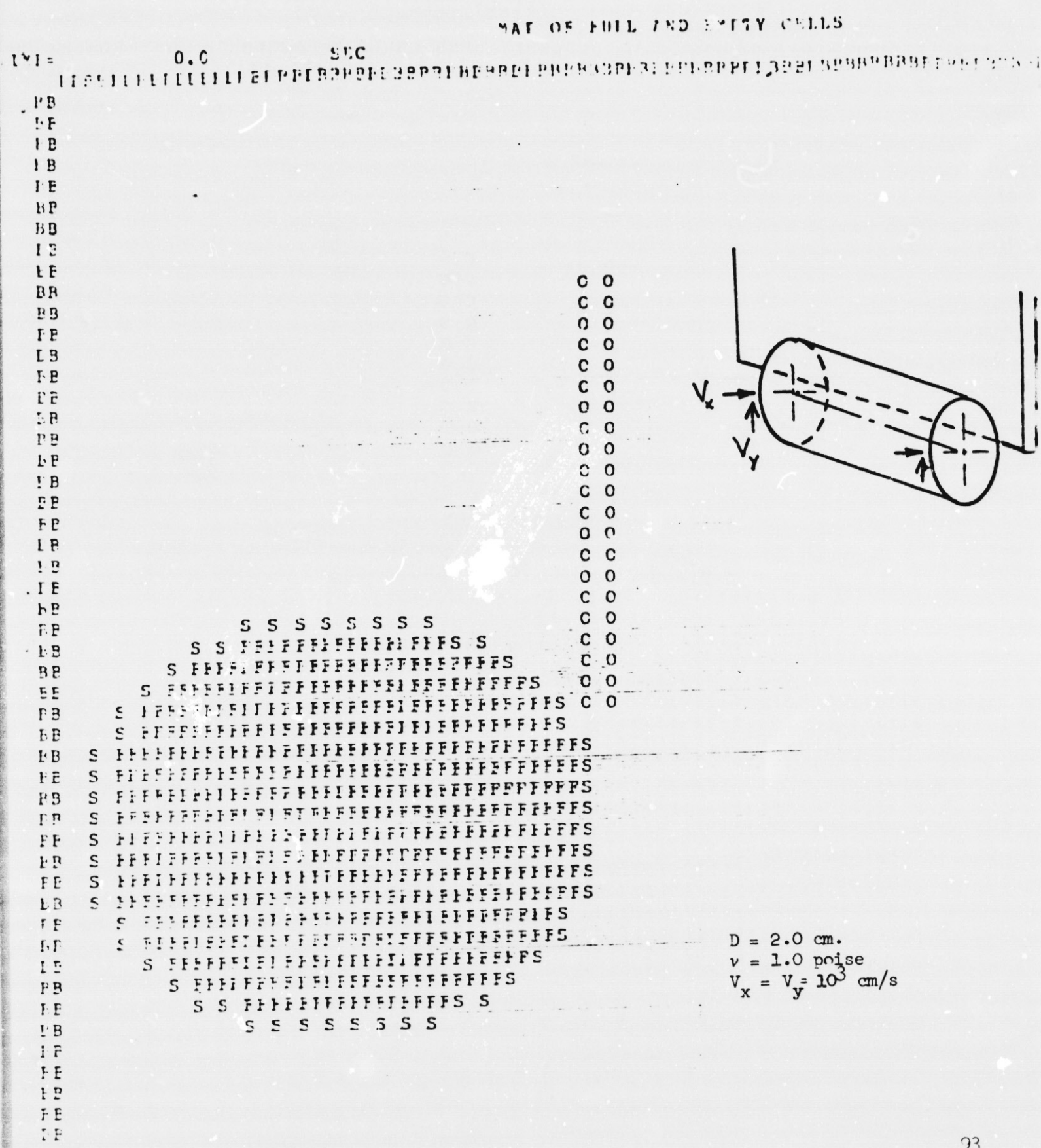

Fig. 29b

MAP OF FULL AND EMPTY CELLS

T= 0.100000E-03 SEC

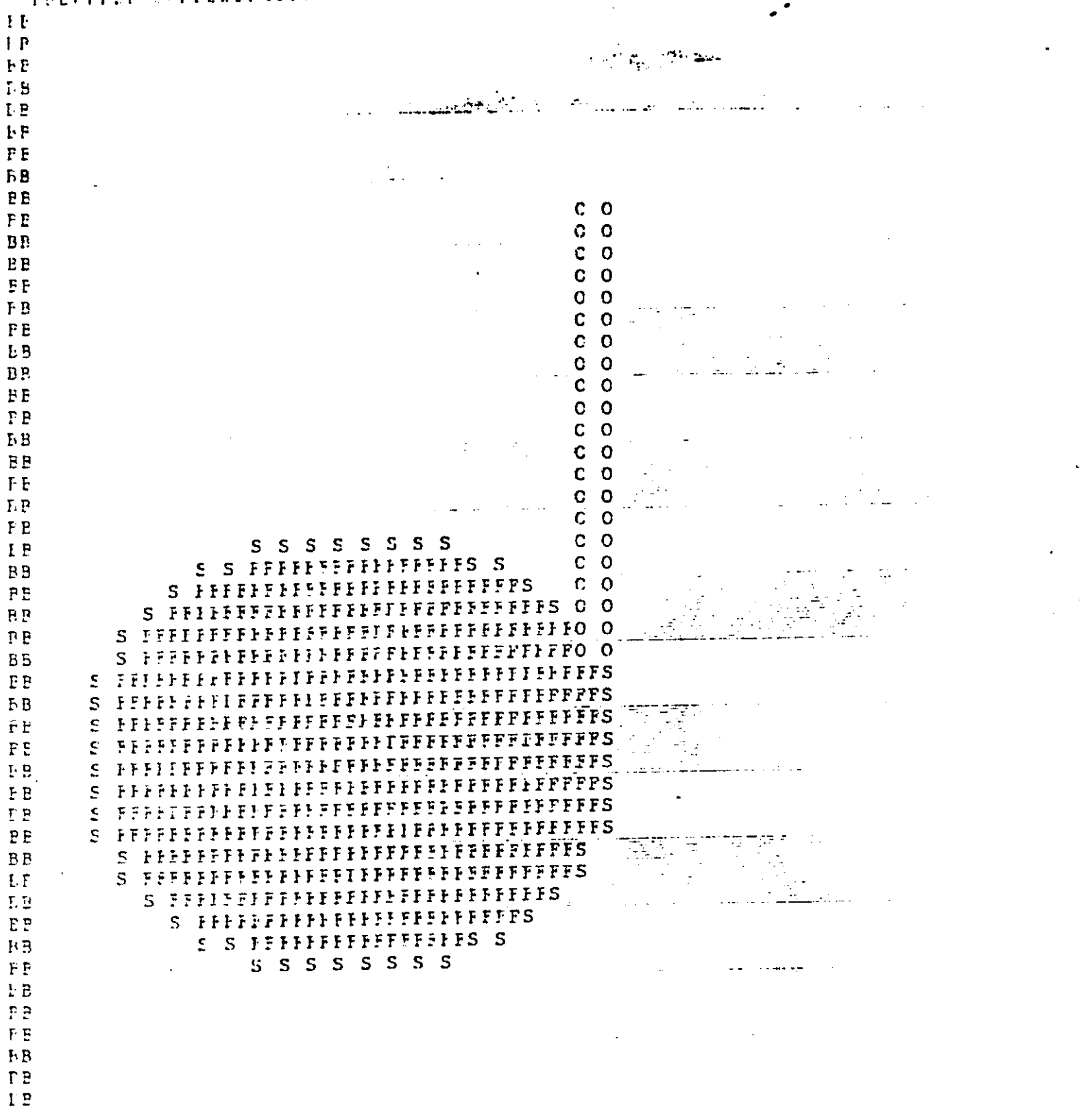

MAP OF FULL AND EMPTY CELLS

TIME= 0.2(((00F-03 SEC

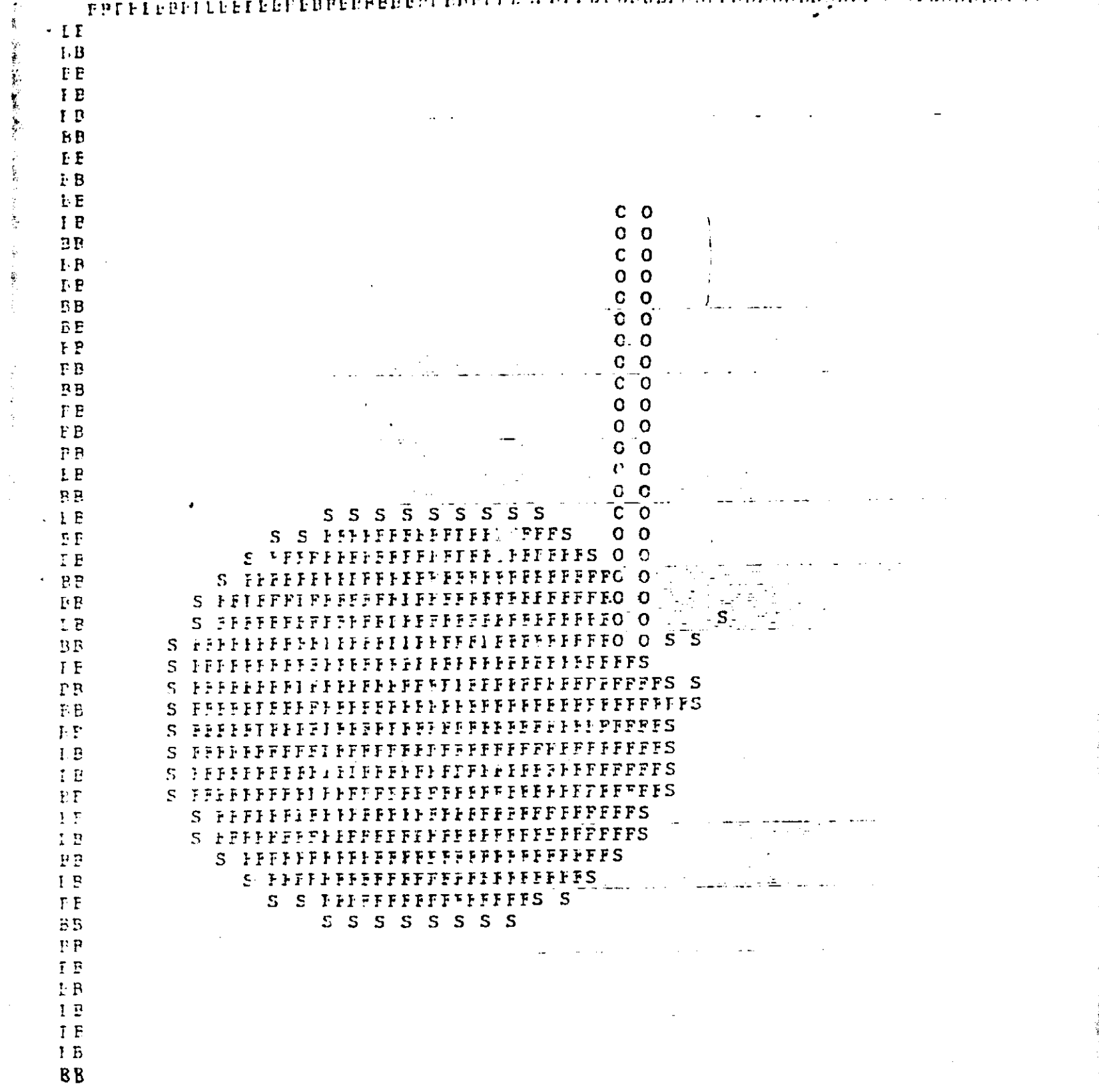

MAP OF FULL AND EMITY CELLS

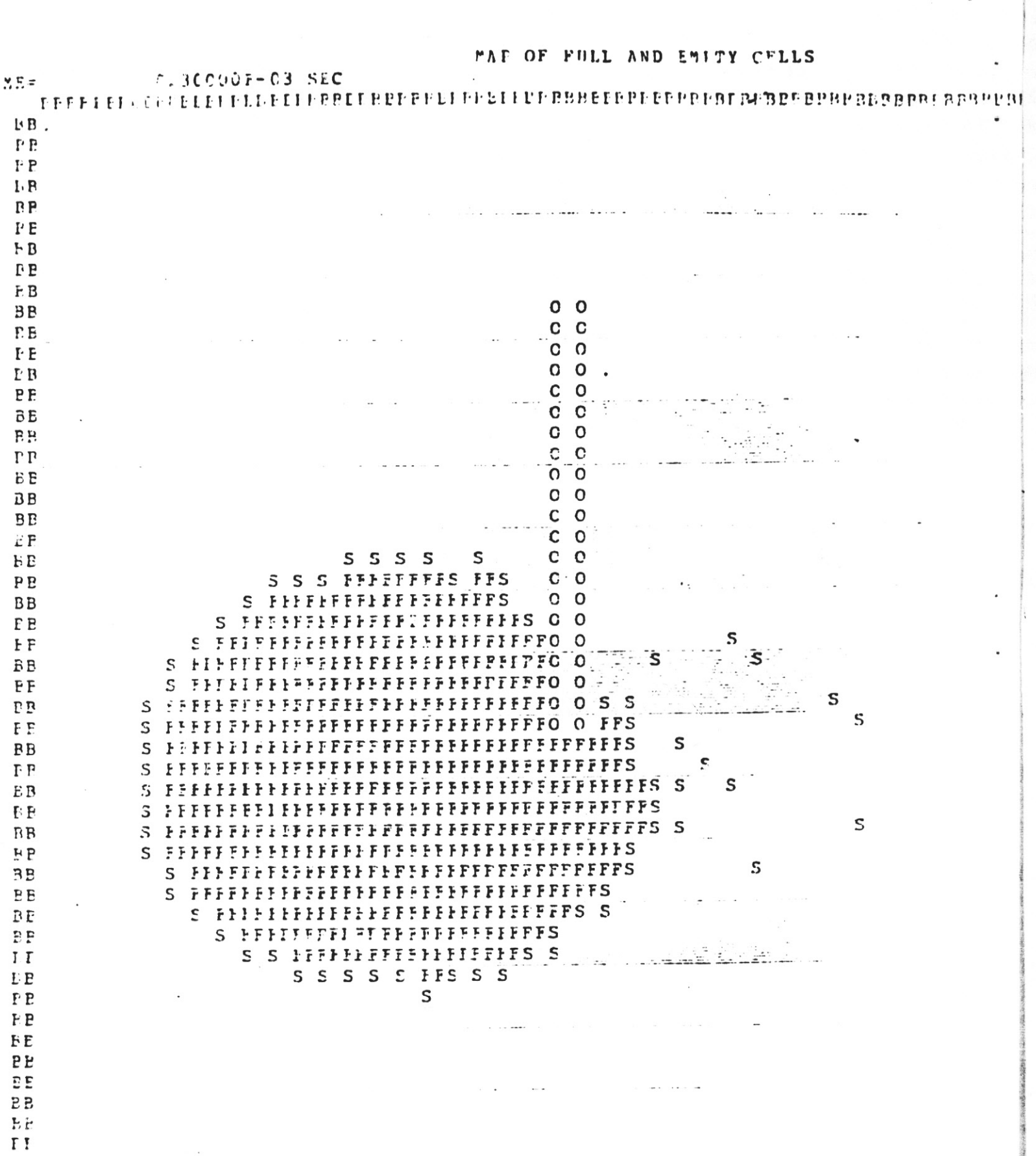

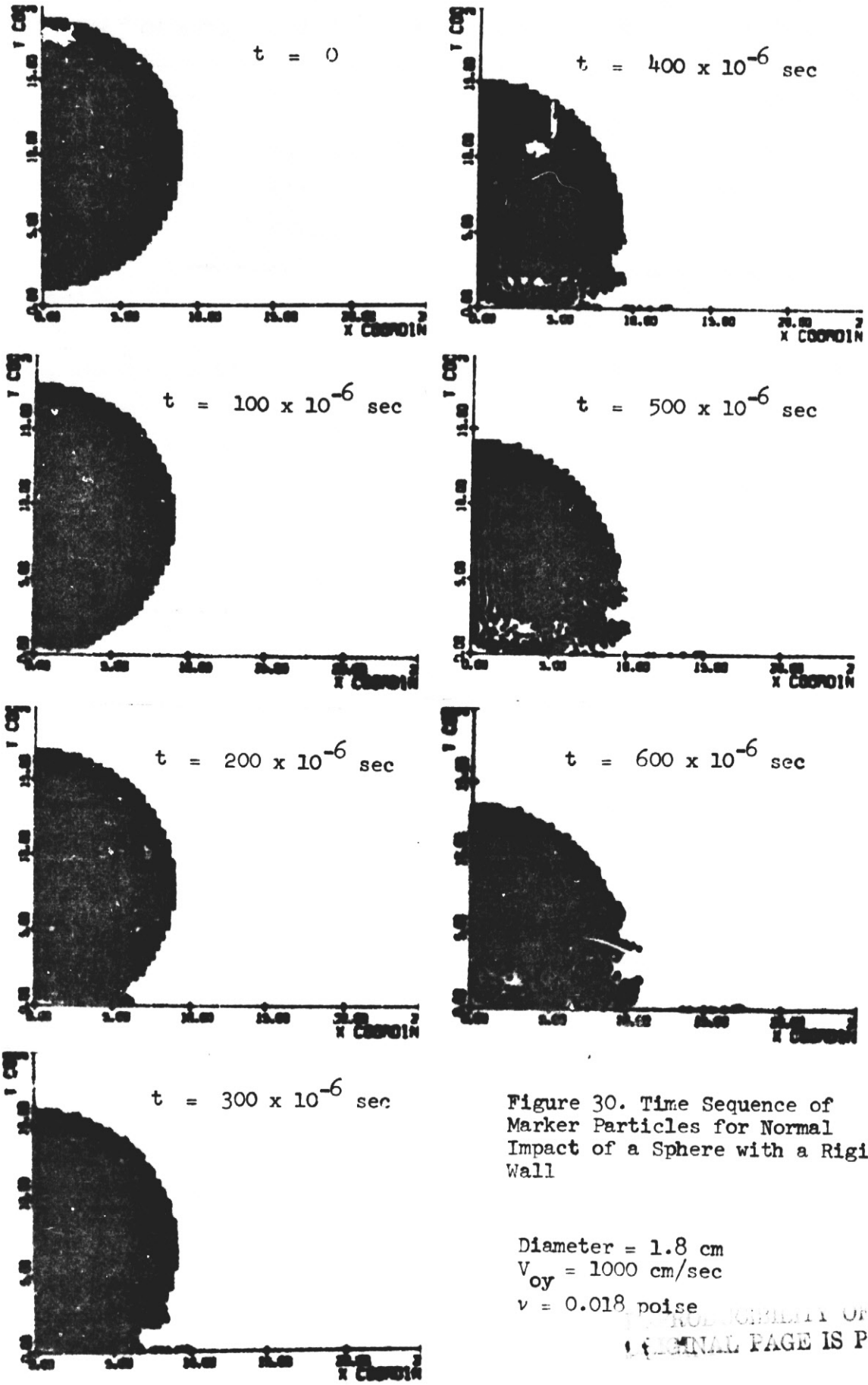

Figure 30. Time Sequence of Marker Particles for Normal Impact of a Sphere with a Rigid Wall

Diameter = 1.8 cm
V_{oy} = 1000 cm/sec
ν = 0.018 poise

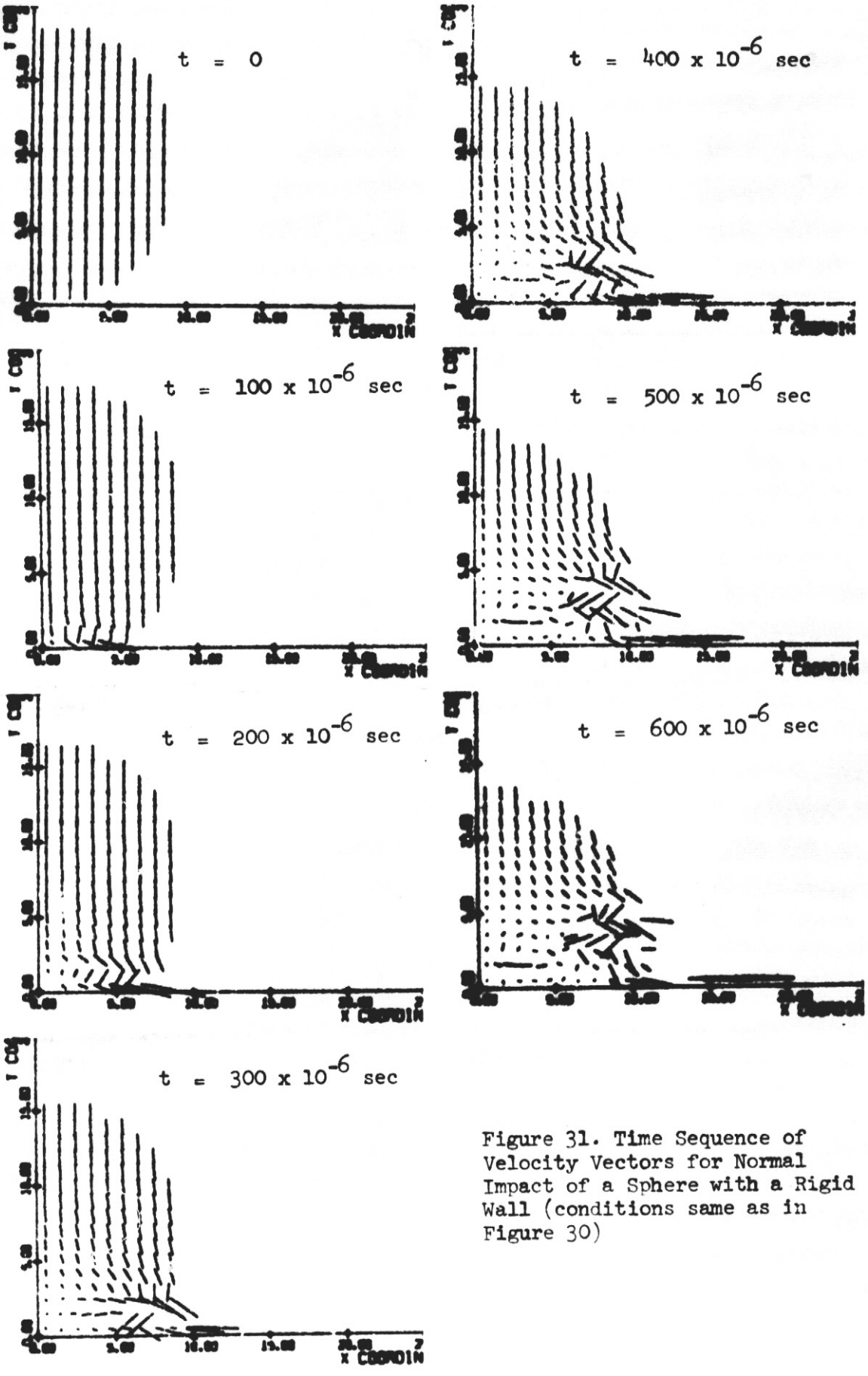

Figure 31. Time Sequence of Velocity Vectors for Normal Impact of a Sphere with a Rigid Wall (conditions same as in Figure 30)

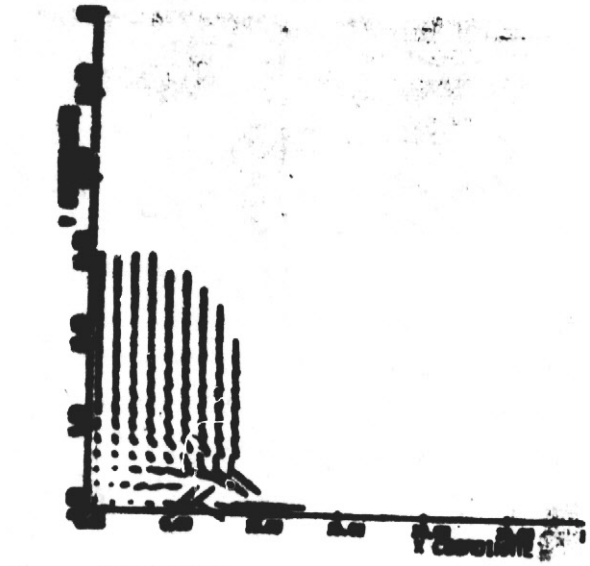

$t = 3\ 10^{-4}s$

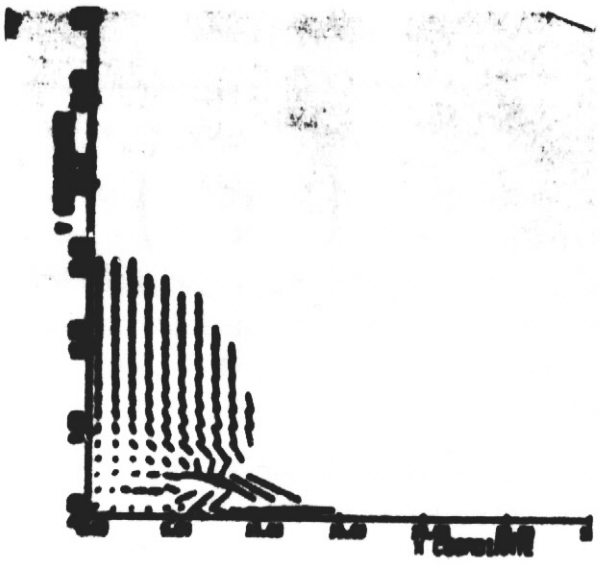

$t = 3.6\ 10^{-4}s$

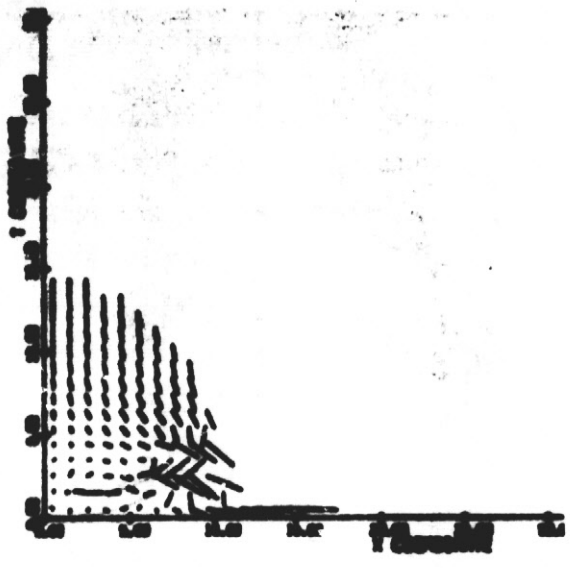

$t = 4.8\ 10^{-4}s$

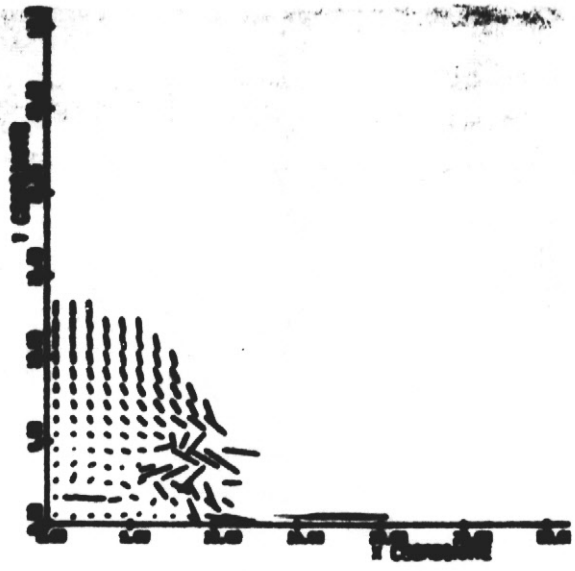

$t = 6.0\ 10^{-4}s$

Figure 32. Velocity Vectors for Normal Impact of a Sphere, (Diameter 1.8 cm. Velocity 1000 cm/s., Kinematic Viscosity 0.018 poise) Showing Development of Eddy Flow

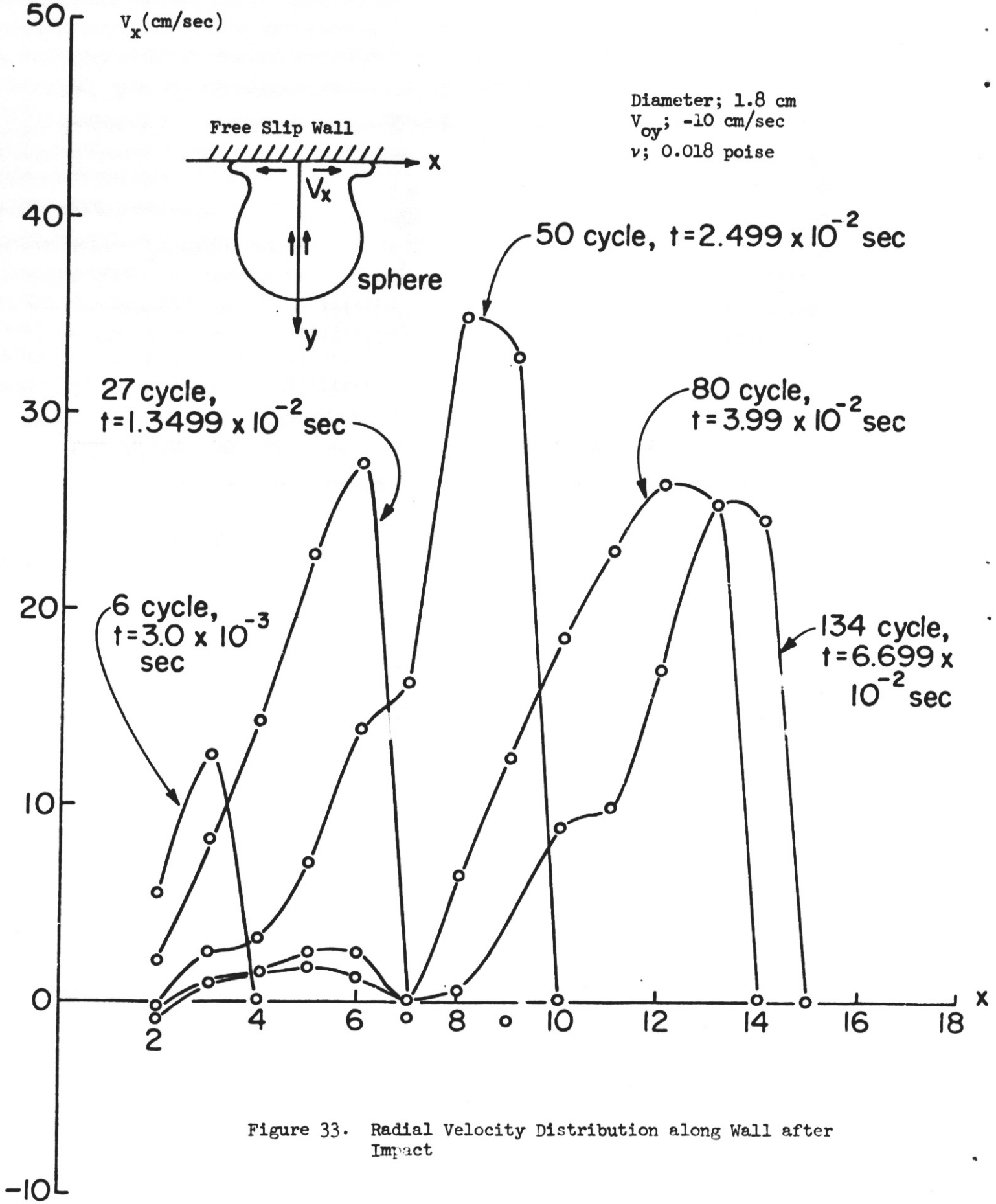

Figure 33. Radial Velocity Distribution along Wall after Impact

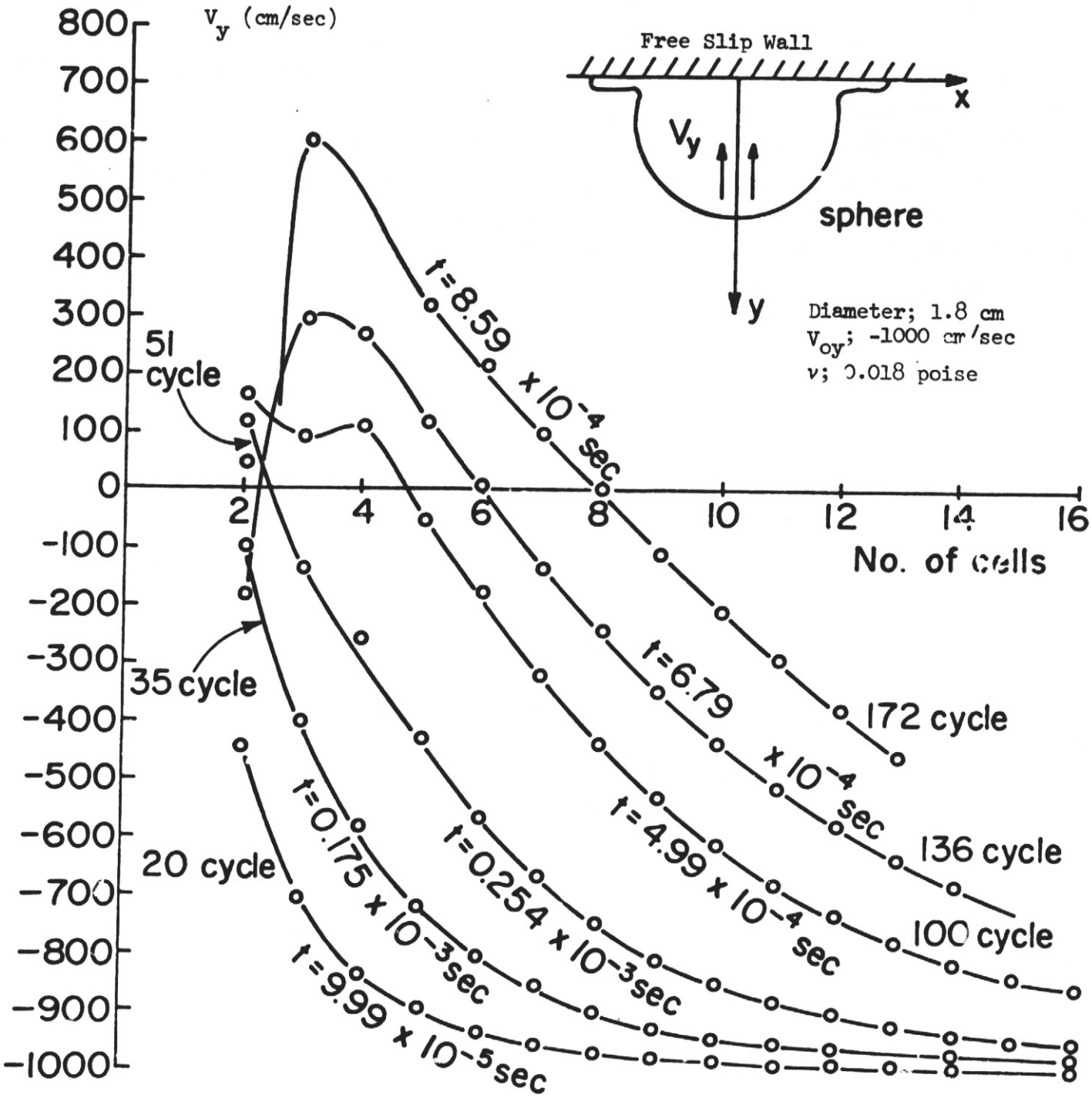

Figure 34. Normal Velocity Distribution along the Impact Axis

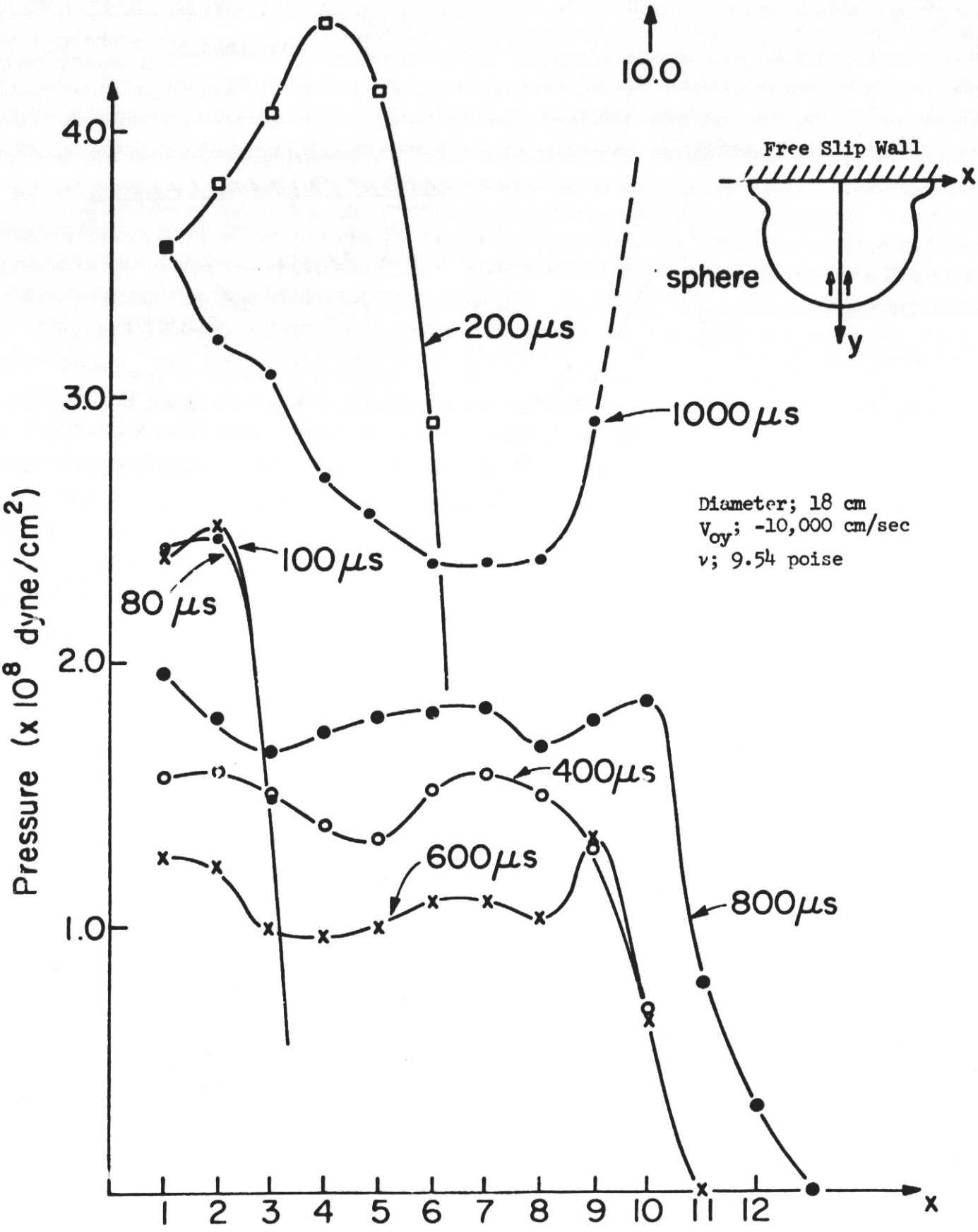

Figure 35. Pressure Distribution along the Wall after Impact

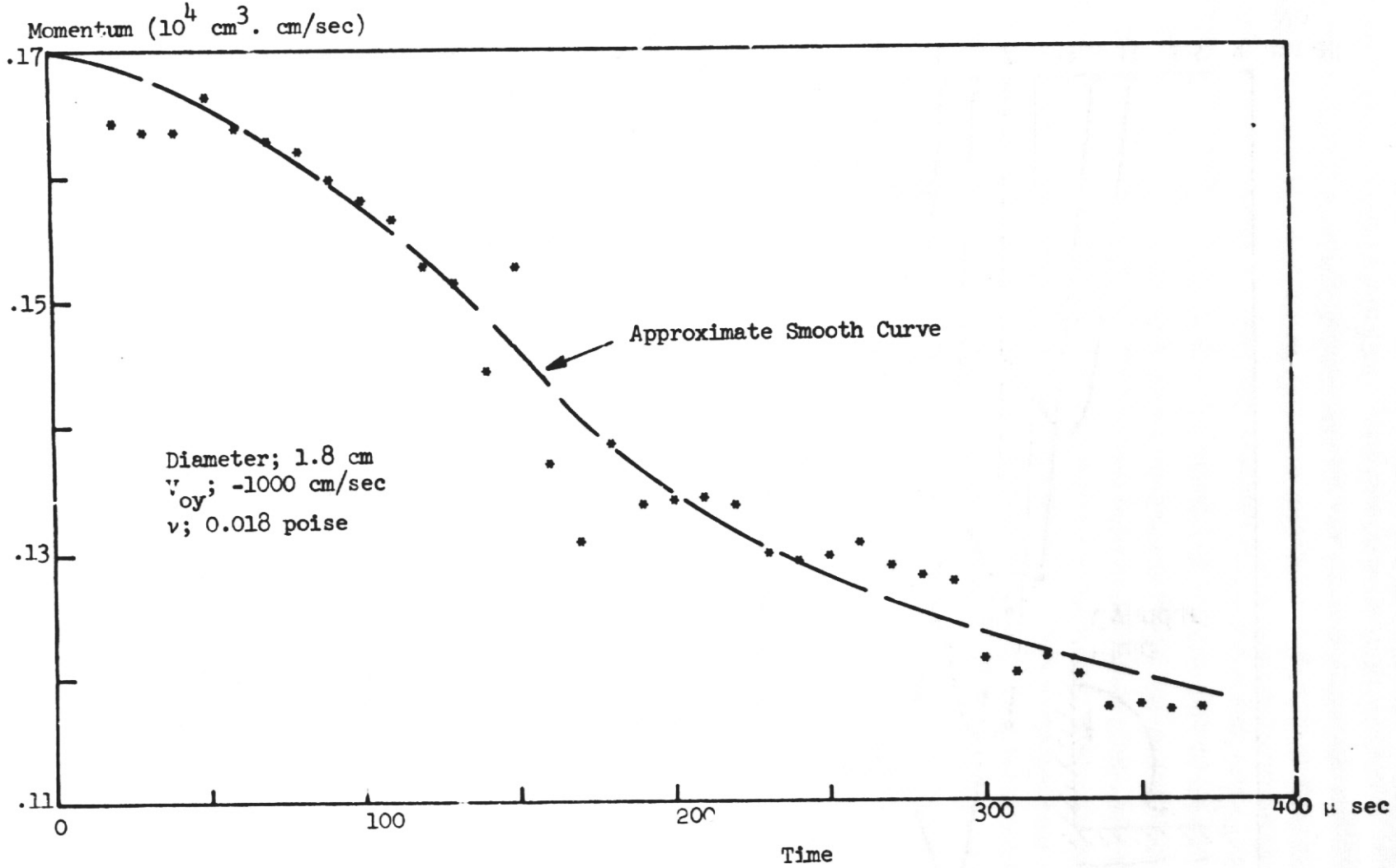

Figure 36. Normal Momentum Vs Time after Impact of a Fluid Cylinder with a Free Slip Wall

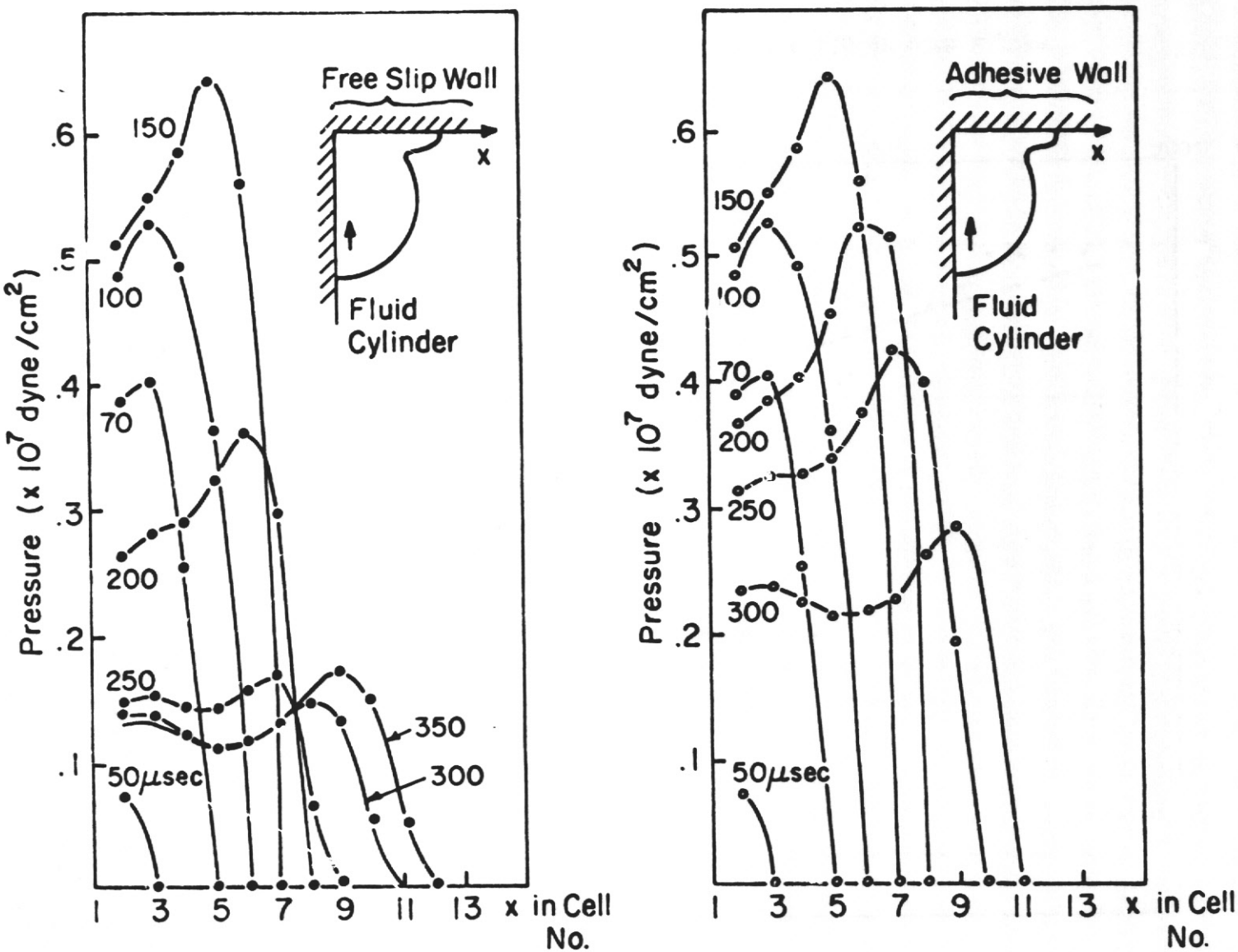

Figure 37. Pressure Distribution along Wall after Impact (Diameter; 1.8 cm. V_{oy}; -1000 cm. ν; 0.018 poise)

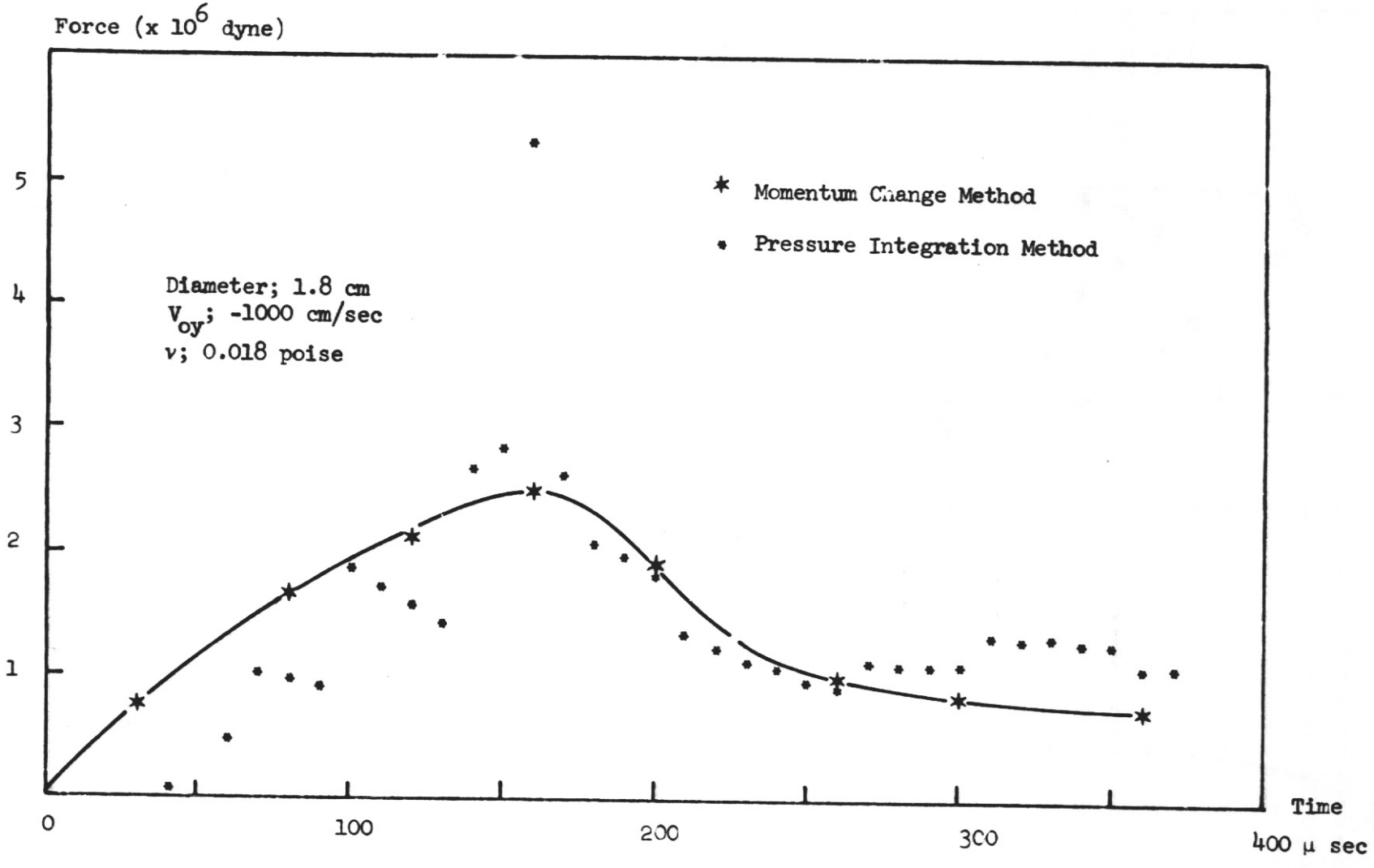

Figure 38. Normal Impact Force Vs Time for a Normal Impact of a Fluid Cylinder with a Rigid Wall

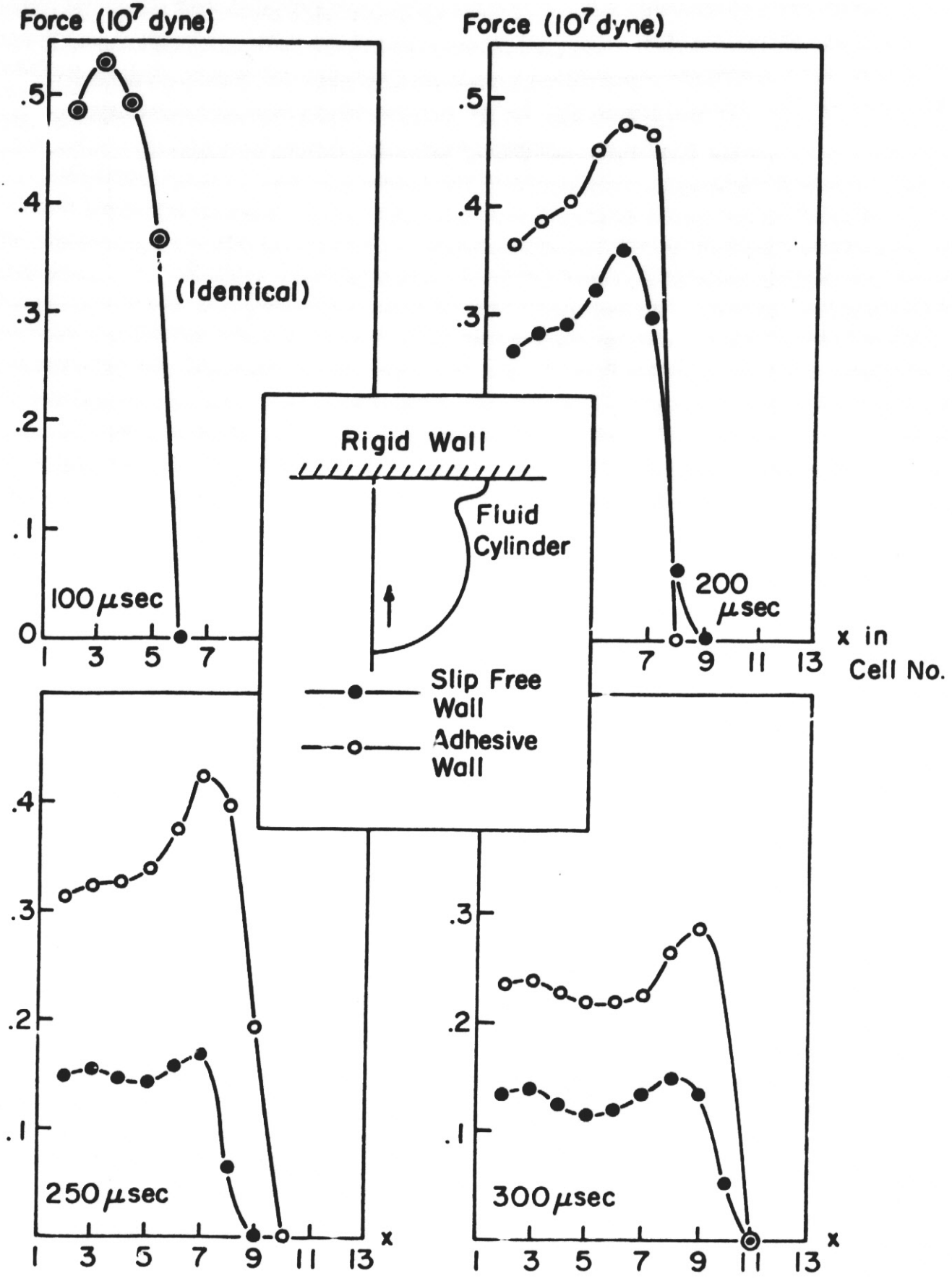

Figure 39. Comparison of Fluid Impact Pressure Distribution along the Wall after Impact (same data as in Fig. 38)

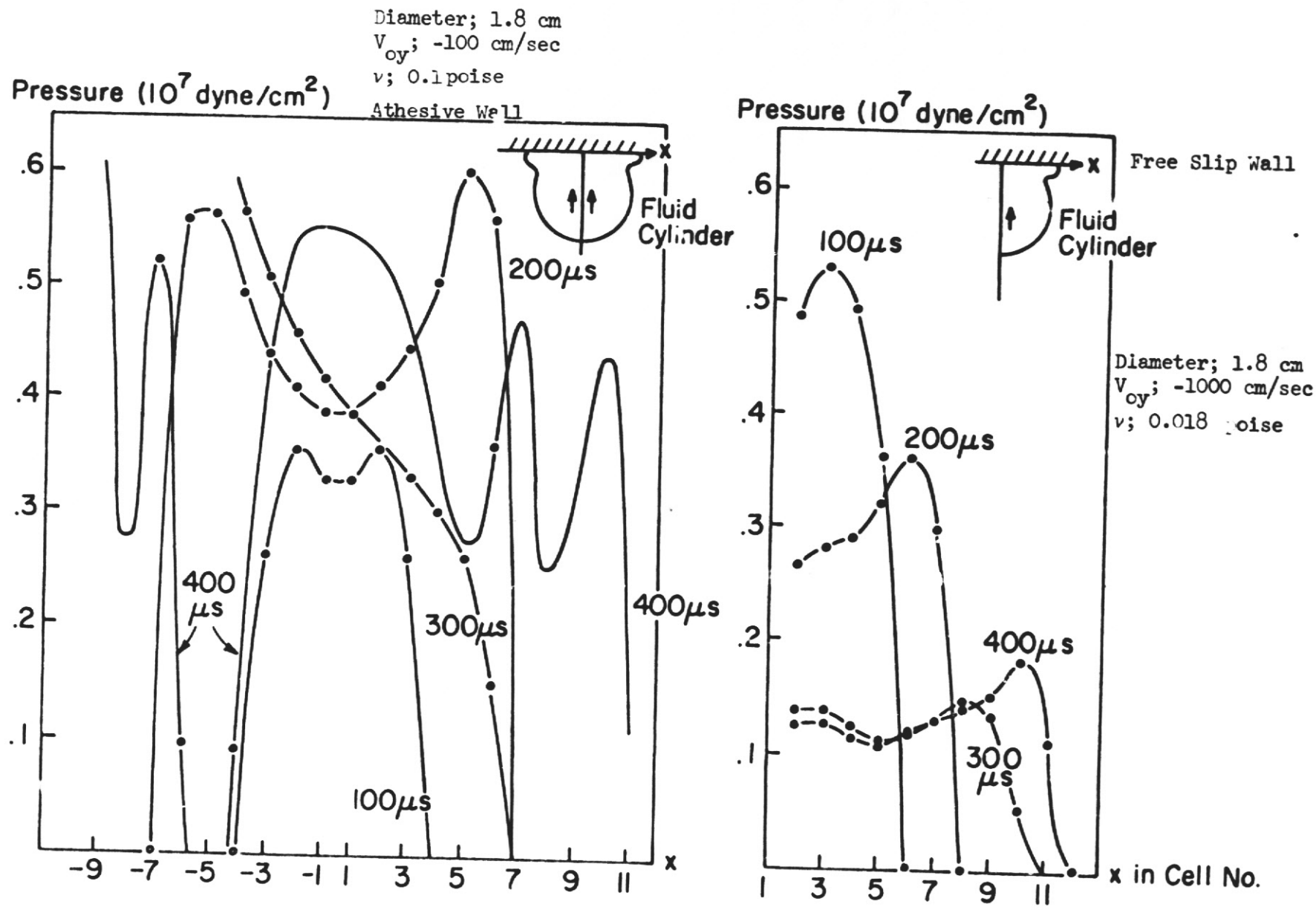

Figure 40. Distribution of Impact Pressure along the Rigid Wall after Impact